論文 / 著書情報
Article / Book Information

題目(和文)	
Title(English)	Study on High-resolution and Compact VCSEL Beam Scanner for 3D Sensing
著者(和文)	LiRuixiao
Author(English)	Ruixiao Li
出典(和文)	学位:博士（工学）, 学位授与機関:東京工業大学, 報告番号:甲第11755号, 授与年月日:2022年3月26日, 学位の種別:課程博士, 審査員:小山 二三夫,植之原 裕行,中村 健太郎,西山 伸彦,宮本 智之,馬場 俊彦
Citation(English)	Degree:Doctor (Engineering), Conferring organization: Tokyo Institute of Technology, Report number:甲第11755号, Conferred date:2022/3/26, Degree Type:Course doctor, Examiner:,,,,,
学位種別(和文)	博士論文
Type(English)	Doctoral Thesis

博士論文

Study on High-resolution and Compact VCSEL Beam Scanner for 3D Sensing
(3D センシング用高解像度小型面発光ビームスキャナーに関する研究)

令和 4 年（2022 年）2 月版

提出者

東京工業大学 工学院 電気電子系 電気電子コース

学籍番号　19D18320

Ruixiao Li

指導教員　　小山二三夫教授

内容

Important abbreviations used in the thesis

Abbreviations	Full words
VCSEL	Vertical cavity surface emitting laser
LED	Light emitting diode
EEL	Edge emitting laser
DFB	Distributed feedback
DBR	Distributed Bragg Reflector
ASE	Amplified spontaneous emission
DOE	Diffractive optical element
UV	Ultraviolet
LiDAR	Light detection and ranging
FMCW	Frequency modulated continuous wave
PL	Photoluminescence
QW	Quantum well
FoV	Field of view
EFL	Effective focal lens
NA	Numerical aperture
NFP	Near field pattern
FFP	Far field pattern
1/2/3 D	One/two/three dimensional

Important symbols used in the thesis

Symbols	Physical meaning
λ_{in}	Wavelength of coupled light from external light source
λ_r	Resonance wavelength of scanner/amplifier/waveguide
n_{wg}	Refractive index of top DBRs
θ_d	Specialized deflection angle
θ_{div}	Diffraction-limited beam divergence of beam scanner
l	Length of beam scanner
d_0	Aperture width of beam scanner
d_1	Mesa width of beam scanner
M^2	Beam quality factor
$I_{scanner}$	Current injected into scanner
I_{VCSEL}	Current injected into VCSEL
$\Delta\theta$	FoV of scanner in θ direction
$\Delta\phi$	FoV of scanner in ϕ direction
$\delta\theta$	Beam divergence of scanner in θ direction
$\delta\phi$	Beam divergence of scanner in ϕ direction
N_θ	Resolution points number in θ direction
N_ϕ	Resolution points number in ϕ direction
N	Number of scanners in the array
n	Number of spot of DOE
Λ	Grating pitch (Both for slow-light VCSEL and DOE)
λ_{VCSEL}	The lasing wavelength of integrated VCSEL
N_{eff}	Effective index of wafer for slow-light mode
m	The order of DOE
θ_m	The diffraction angle of mth order of DOE under normal incident
θ'_m	The diffraction angle of mth order of DOE with incident angle
θ_i	The incident angle to DOE
θ_s	Separation angle between 0th and 1st order of DOE
s	Space between scanners in the array
h_p	Height of prism mirror
w_p	Width of prism mirror
θ_p	Slope angle of prism mirror
l_p	Length of prism mirror

$\boldsymbol{\theta_{ds}}$	Smallest deflection angle of beam scanner
$\boldsymbol{\theta_{dm}}$	Largest deflection angle of beam scanner
$\boldsymbol{L}$	The length of beam steering module
$\boldsymbol{H}$	The height of beam steering module
$\boldsymbol{W}$	The width of beam steering module
$\boldsymbol{f}$	Effective focal lens of cylindrical lens
$\boldsymbol{\phi_{res}}$	The space between two resolution points in $\boldsymbol{\phi}$ direction
$\boldsymbol{b}$	length of baseline (distance between scanner and camera)
$\boldsymbol{\delta d}$	depth between target plane and reference plane
$\boldsymbol{D}$	depth of reference plane
$\Delta\boldsymbol{x}$	Displacement (disparity) in $\boldsymbol{x}$ direction
$\Delta\boldsymbol{y}$	Displacement (disparity) in $\boldsymbol{y}$ direction
$\boldsymbol{N_y}$	Resolution of 3D sensing image in y direction
$\boldsymbol{N_x}$	Resolution of 3D sensing image in x direction
$\boldsymbol{N_{ytotal}}$	Resolution of real-time 3D sensing in y direction per second

Chapter 1

Introduction

In this thesis, the VCSEL beam scanner with ultra-large field of view and high-resolution is proposed and demonstrated. It also provides high power, good manufacturability, and compact module size. It may provide new opportunities for next-generation 3D sensing. In this chapter, the development of 3D sensing applications will be firstly discussed, and then the previous work of current beam scanner including the VCSEL beam scanner.

1.1 Background

1.1.1 Development of 3D sensing applications

In recent years, the 3D sensing has been attracting much attention thanks to its application in mobile phones, robots, manufactory, automotive and intelligent society. It could be said that the 3D sensing will be a key element in the future society and appears in any home all over the world. Since 2017, Apple has firstly applied 3D sensing in our frequent daily life. They sale a cross-generation mobile phone iPhone X. Once it was released, it attracted extremely-high attention and almost all of other phone companies has started to apply 3D sensing to their product. However, the 3D sensing elements could only be found in high-level products of phone companies until now. It has been recognized that the application of 3D sensing could bring revolution to imaging, entertainment, and daily life. From the study from Yole, the 3D sensing may contribute the market of more than 15 billion dollars in 2025 by current technology in Fig. 1-1. Of course, we could further expect the more rapid increasing thanks to the development of 3D-sensing-related applications and the maturity of 3D-sensing-related technology.

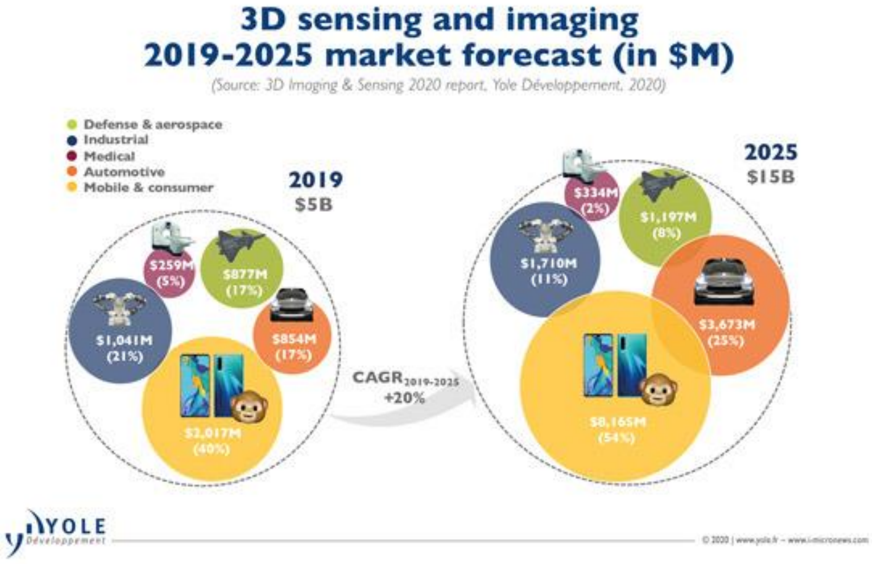

Fig. 1-1. The forecast of 3D sensing in these years [1]

Then, the application details of 3D sensing will be discussed. Firstly, the nearest application is in mobile phones. The 3D sensing was firstly used in iPhone X as Face ID, which enables you to unlock your phone by the 3D information of your face and also to open some special applications that requires your identification. In recent years, as a new and potentially main application in the future, the depth camera used for automatic focusing or automatic exposure has been gradually developed and equipped with more mobile phones. In current condition, it is difficult to know the real depth of target when taking a photo, so the target focusing is critical issue especially when expecting to realize background emptiness in a very near field. The depth camera could provide valuable depth information for autofocus control.

Fig. 1-2. Example of Face ID in IPhone [2]

The second nearest application is automotive. With development of electrical cars, the automotive gradually becomes an important factor when people make the purchase decision. For example, Tesla has become the first largest (Market value) company thanks to its excellent achievement in developing intelligent cars. However, the passive stereo vision that has been used in Tesla also arises many concerns about accuracy in long distance, the tolerance for variable complex environment and high computational consumption. The automotive level was classified by 6 steps. By using tesla's solution, only level 2 could be realized. It was recognized that the active Light Detection and Ranging (LiDAR) is the best choice for leve-5 absolutely automotive.

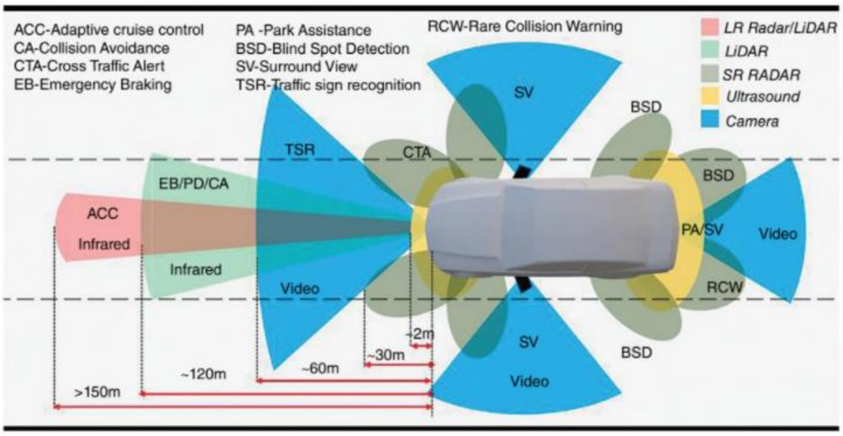

Fig. 1-3 3D sensors for automotive [3]

The third application introduced here is for industrial manufacturing. It seems to be far away from our lift, but it will bring the revolution to current manufacturing. Most of big companies has been using machines to fasten the manufacturing speed and efficiency, but many workers are still needed to make the machines work together and there might be many dangerous environments that is not suitable for people to work, for example the mine and iron production. The automatic manufacturing will provide safety to the workers and the release the works to highly-technical industry, which will thoroughly improve the development of the society. As the eye of industrial robots or machines, 3D sensing is essential for its information capturing and intelligent decision.

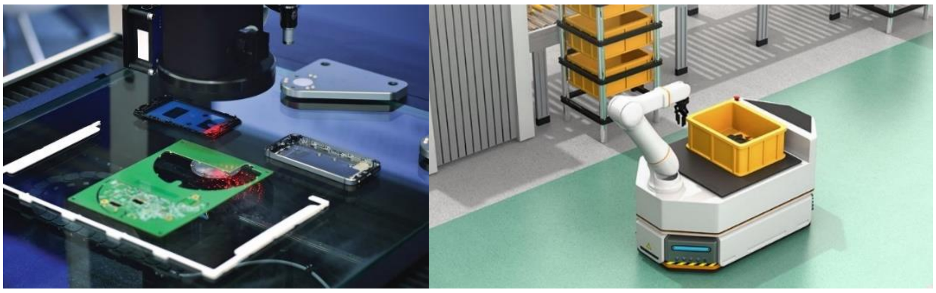

Fig. 1-4. Optical inspection for quality control and Automated Guided Vehicle for intelligent manufactory [4]

1.1.2 *Introduction of 3D sensing technology*

a. Two-camera stereo vision

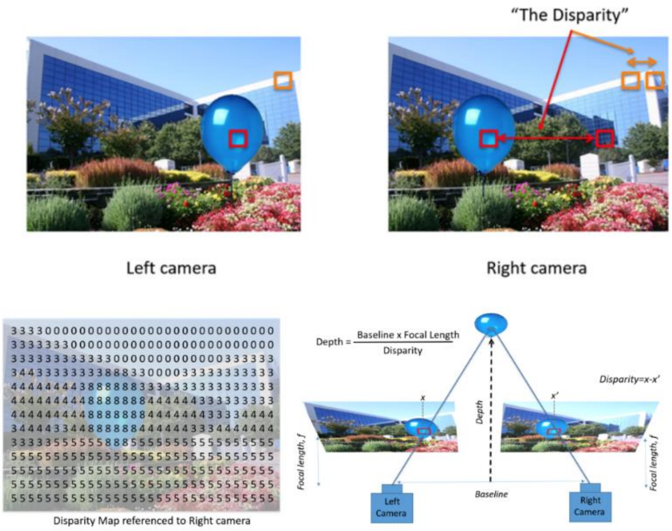

Fig. 1-5. Principe of passive stereo vision [5]

3D sensing is a technique that captures the spatial position information in the three-dimension space. The most important information is depth because horizontal position could be easily obtained by conventional 2D camera. It usually uses the following three could of technologies: 1. Two-eye stereo vision; 2. Structured-light sensing; 3. Time of flight sensing. In details, stereo vision could be classified into active and passive method. It applies the same method of our eye to capture the 3D information of targets as shown in Fig. 1-6. Two cameras that was placed separately will capture the photo of the same target. In the two photos, the position of each point captured by the left camera will be a little different from that captured by the right camera. We call this difference disparity, from which the depth information of each point could be calculated. Also the horizontal information could be estimated by the depth and internal parameters of camera, for example, focal length and pixel size. To get the depth information accurately, the photo should be taken when sunlight is strong enough but not over exposed. It highly depends on the environment condition for example weather. It is also important to find the correspondence of two photos, which may lead to larger memory and computational cost. For easier correspondence between two photos and better environmental tolerance, active

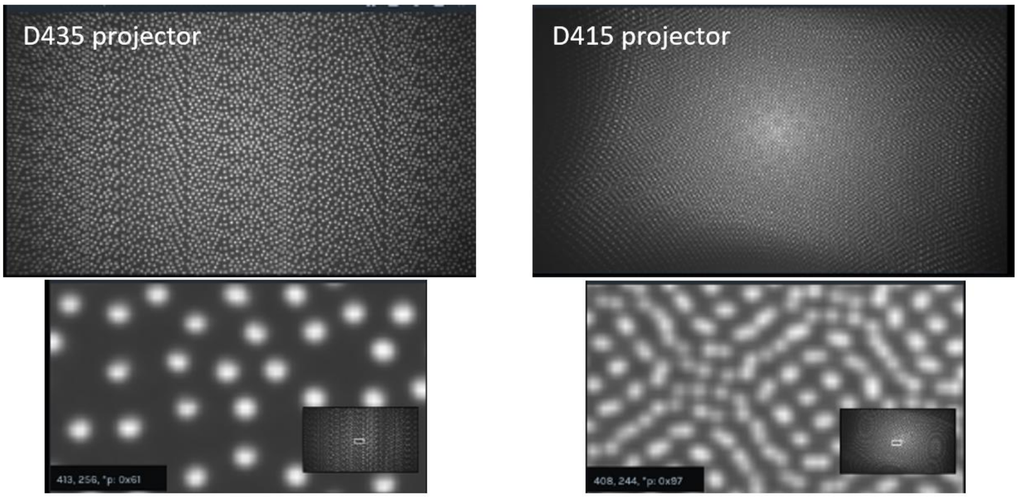

Fig. 1-6. Pattern generated for active stereo vision [5]

two-eye stereo vision was proposed. A designated pattern generated by light source and optics will be projected to the object as shown in Fig 1-6, which has been used in Microsoft RealSense D400 series. The correspondence between two photos will not rely on the target but depends on the correspondence of designate pattern. It largely simplifies the corresponding process and is very beneficial for the use in dark environment. In the other side, only one camera could only realize the same function.

b. Structured-light sensing

As mentioned before, the correspondence and disparity between two photos provides the path to calculate depth information. One of photos could be the original pattern recorded in advance. To compare the disparity between the captured photo of target and recorded pattern. The depth could be also obtained. We call this kind of technology structured-light sensing as shown in Fig 1-6. Actually, structured-light are using the triangulation of camera, target, and projector for active vision.

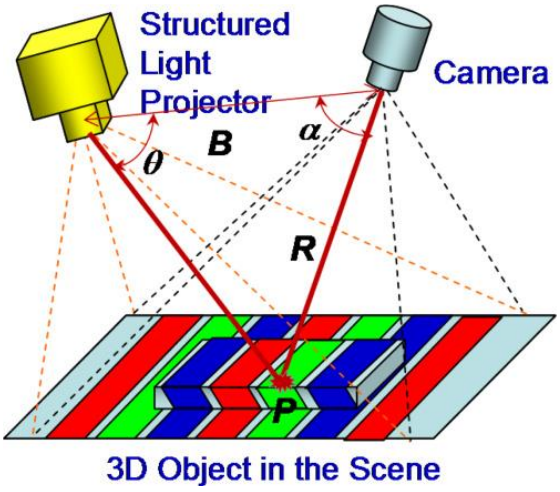

Fig. 1-7. Principle for structured-light sensing [6]

The system of structured-light sensing includes a light projector that illuminates light with designed pattern. The pattern could be coded to find the correspondence of original pattern and reflected pattern. The pattern could be coded as sinusoidal fringe pattern [7], binary pattern[8] and statistical pattern [9] as shown in Fig. 1-8.

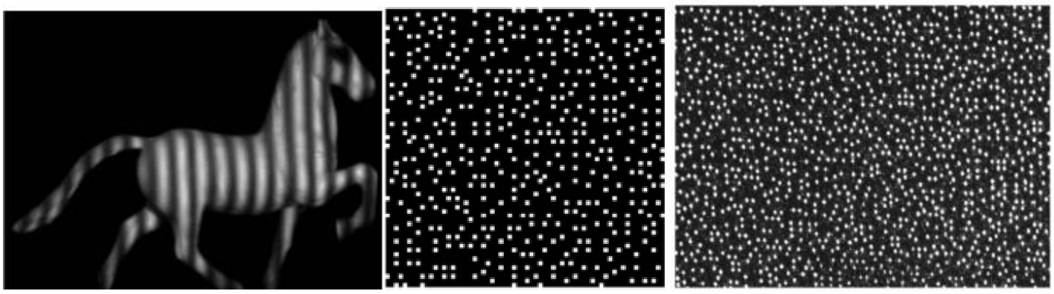

Fig 1-8 The projected pattern for structured-light [6-8]

The pattern reflected by a target will lead to disparity modulated by the depth. The pattern will be received by the camera and be used to estimate the depth of target by calibrated parameters as the workflow shown in Fig. 1-9. In this flow, a grid coded pattern was projected by a DOE-based laser system.

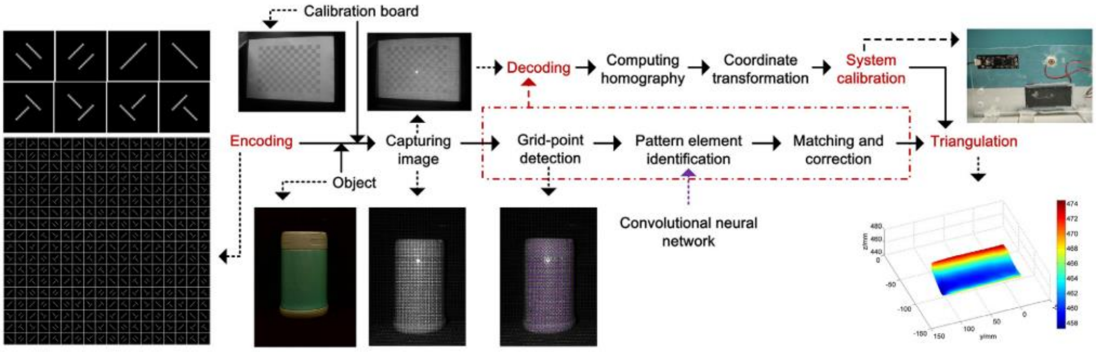

Fig 1-9 The projected pattern for structured-light [10]

Currently, the most frequently applied patterning method for consuming devices is the random statistical pattern that was generated by a VCSEL array and DOE. It could generate the pattern of more than 10,000 dots with designed coding method. However, the statistical pattern size is usually larger than 1 pixel, so the pixel-wise structured-light sensing currently is still difficult for mobile devices. The phase coding structured-light such as sinusoidal fringe pattern could realize pixel-wise sensing, but the light projection method is too complex to be equipped with the mobile phones. The MEMS mirror may be used to realize scanning stripe structured-light without precise coding, but the complexity of MEMS system is still complex for mobile devices.

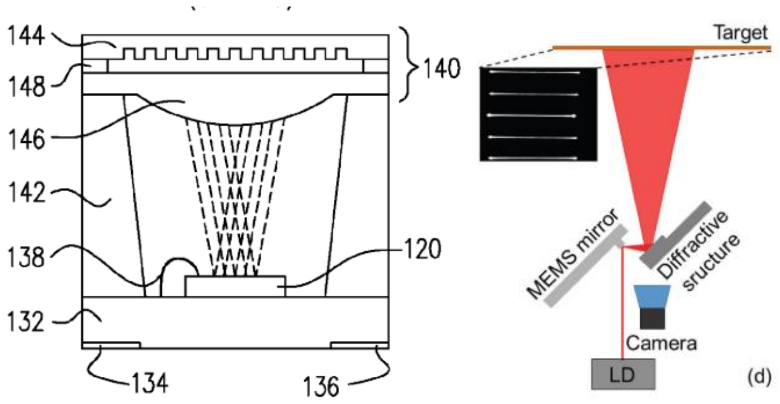

Fig 1-10 DOE-based dot pattern generator[11] and MEMS-based line-pattern projector[12]

c. Time of Flight LiDAR

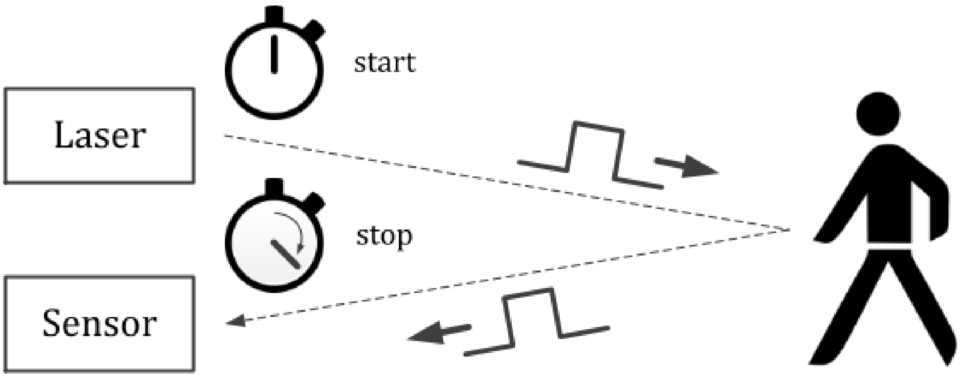

Fig. 1-11. Principle of time of flight sensing [13]

The time-of-flight (ToF) sensing system is composed of a light source and a camera. The light source will emit light to the target. And it estimate the depth between camera and target by the time of light flying between camera and target as shown in Fig. 1-11. Assuming the distance between target and camera is d, and the time when light goes to the target and reflected by the target is t, the distance could be estimated by $d = ct/2$, where c is the speed of light in the propagation material. However, we could emit a pulse to the object and directly estimate the depth through the time delay of emitting pulse and receiving pulse, but sometimes it is difficult to measure the delay accurately for example, when the distance of target is short, the time delay may be too small to be detected by the detector. When the background is strong, for long-distance measurement, the signal may be drawn in the background. Therefore, some indirect method to measure the time delay was developed, of which the most famous and efficient way are charge-based and FMCW-based indirect ToF LiDAR.

The charge-based indirect ToF LiDAR usually has special shutting time design as shown in Fig. 1-12 to integrate the charge excited by received photons in different shutter window. It is obvious that the charge integrated in different shutter window could be modulated by the time delay of reflected light, so the time delay and thus distance could be estimated from the charges in different shutter window. However, due to the limited shutter window length, the available measurement distance is very limited. It is usually used to detect the range within 20m.

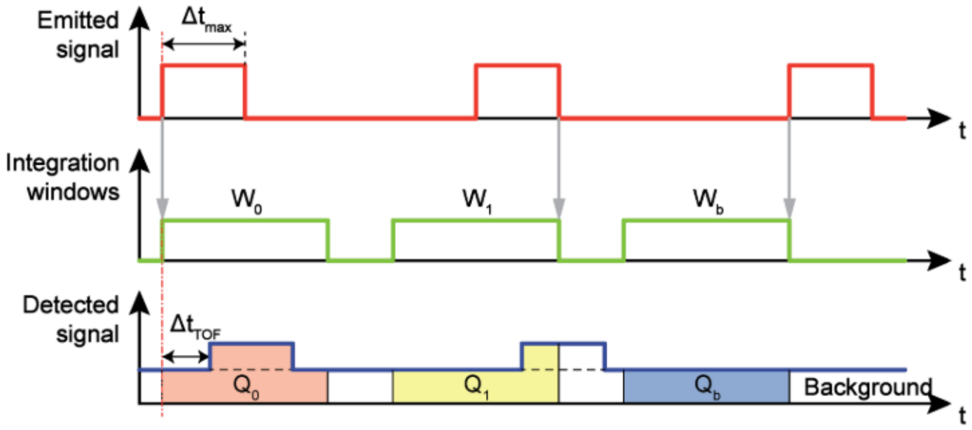

Fig. 1-12 The principle of charge-based indirect LiDAR [14]

For better resistance of background light and availability for reflectivity-varied object, frequency modulated continuous wave (FMCW) LiDAR was proposed. The light source does not emit a single-wavelength pulse anymore, but its wavelength was tuned in some range continuously. The signal with temporally varied wavelength/frequency will be reflected by the target. The frequency shift could be used to estimate the time delay of emitted and received signal as shown in Fig. 1-13. The FMCW always needs large and stable wavelength tuning range to obtain enough ranging resolution and ranging distance, and the tuning speed should be also high for high-speed detection, which may precludes its cost efficiency.

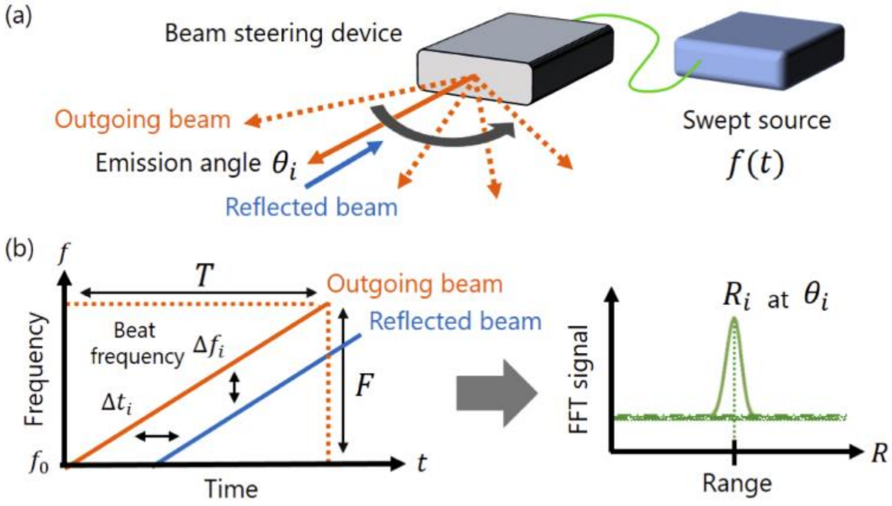

Fig. 1-13 Principle of FMCW LiDAR [15]

Specified by the kinds of light source and detector, the navigation of LiDAR could be implanted in detail. Firstly, the ToF LiDAR could be classified by the light emitting method as shown in Fig. 1-14. The flash LiDAR needs to cover the who detected range at the same time while the scanning LiDAR will only detect a single point and detect the whole field of view by scanning the light spot.

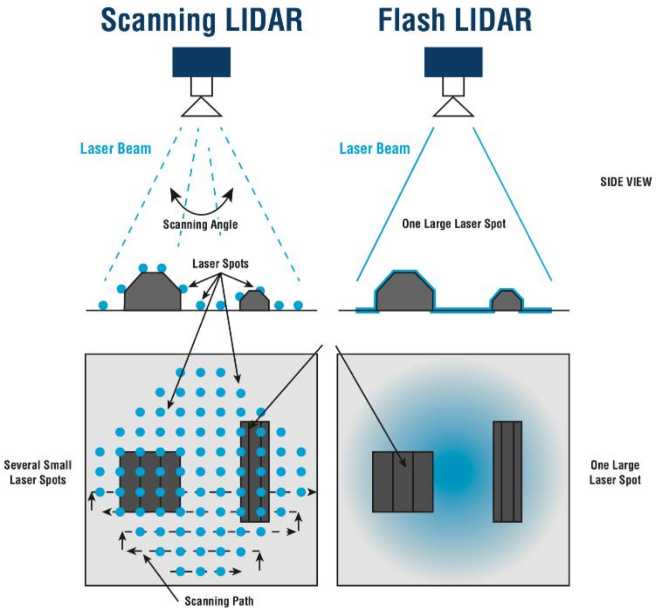

Fig. 1-14 The comparison of scanning and flash LiDAR [16]

The flash LiDAR was firstly proposed and used practically due to the simple light source. It was composed of a laser light source, a diffuser and a multi-pixel camera [17]. Although its setup is very simple, it is difficult to realize depth detection at long distance because the large power diffusing. Another problem is the ghost image will be generated by the multi reflection of diffused light [18]. To emerge the requirement for long-distance ranging for automotive, the scanning LiDAR based on mechanical rotation [19] and MEMS mirror [20] were proposed and manufactured by some companies. They were equipped with the cars to test the automotive beyond level 3. However, the mechanical LiDAR are facing to serious problems of stability, long-term availability and scanning speed. Its cost and size are also problems for further application.

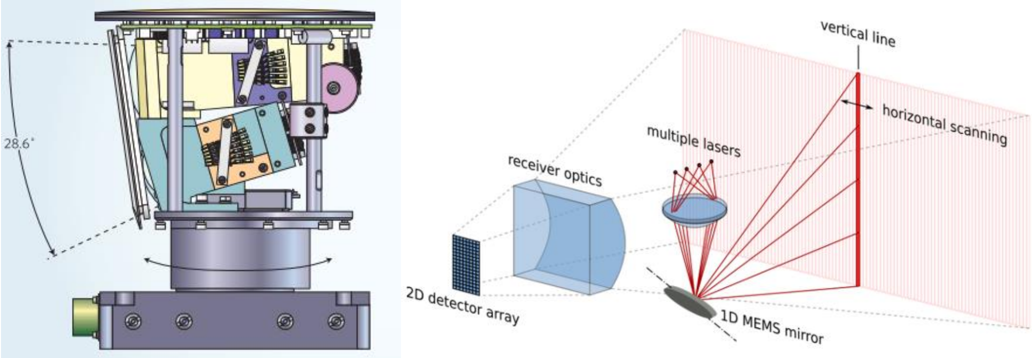

Fig. 1-15 The principle of mechanical LiDAR [19] and MEMS mirror LiDAR [20]

To avoid the mechanical elements and simplify the manufactory complexity, LiDAR based on semiconductors were proposed and demonstrated. For instance, the LiDAR based on optical phased array (OPA) [21] and photonic crystal slow-light waveguide [22] succeeded in detecting the object placed at several meters. However, the on-chip solid-state LiDAR are still at primary stage due to the limitation of scanning light source, for example limited resolution, scanning range and output power and detector, for example, the sensitivity and internal noise.

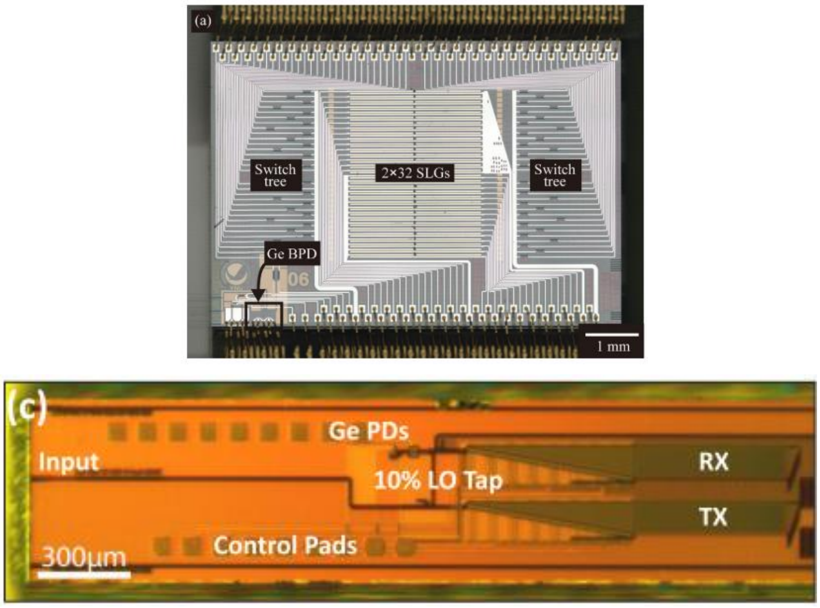

Fig. 1-16 Solid-state LiDAR based on optical phased array (OPA) [21] and photonic crystal slow-light waveguide [22]

As mentioned, the sensitivity of detector is also important for LiDAR. Currently, the avalanche photodiodes (APDs) or photomultiplier tubes (PMTs) are usually used for long-range detection. However, its array integration is difficult. Single-pixel measurement could greatly reduce the requirement for large-scale detector integration. Beam scanning technology is also helpful for single-pixel LiDAR [23] while the flash sensing is difficult to realize single-pixel LiDAR. Recently, some temporally varied laser projector were used to realize single-pixel LiDAR. A LiDAR system based on structured illumination was previously proposed and demonstrated to realize 128 × 128 points depth detection at around 5m distance [24]. A spectral-temporal modulated light source with spatial dispersion was also demonstrated to realize the depth detection at <1m distance [19]. These new schemes expand the path to realize the cost-effective LiDAR, but the resolution and available range is still far away from real application. In current stage, the solid-state scanning LiDAR are still thought to be the most promising solution for real applications.

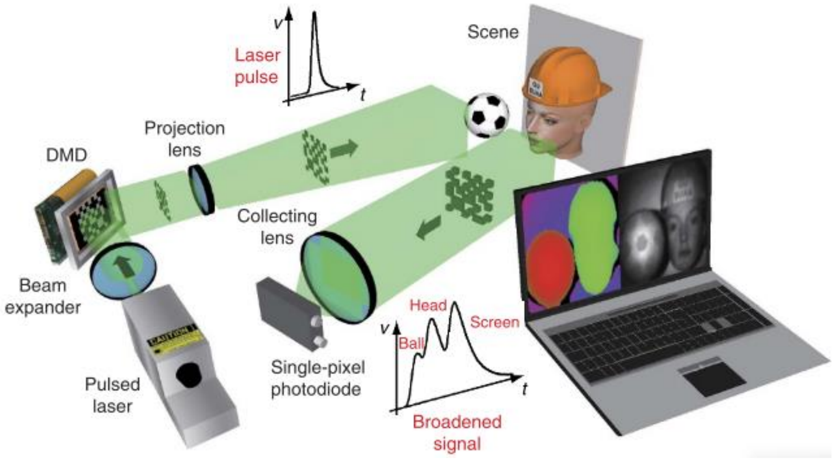

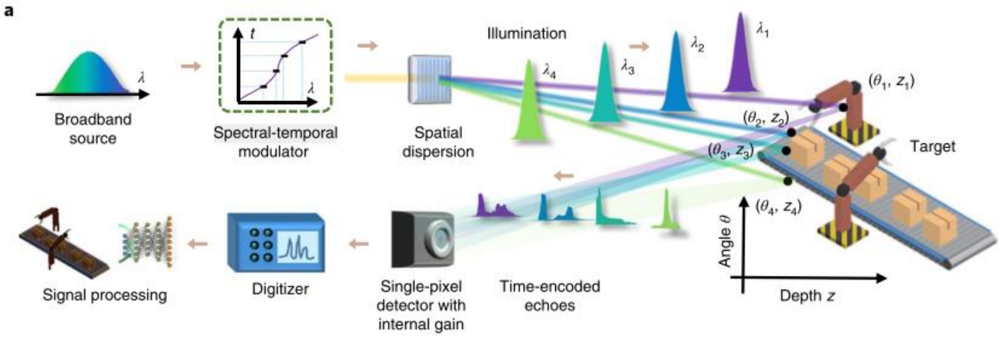

Fig. 1-17 Single-pixel LiDAR based on structured illumination [24] and spectral-temporal modulated light source [25]

d. The comparison of different 3D sensing technologies

The comparison of these method was shown in the table 1-2.

Table 1-1 Comparison of different kinds of 3D sensing technology

	Passive stereo Vision	Time of flight	Structured-Light
Bright background	○	△	△
Dark background	×	○	○
Short Range (<1m)	○	○	○
Middle range (5-50m)	△	○	×
Long range (>100m)	×	△	×
cm-detect	○	○	○
μm-detect	×	×	○

As mentioned before, the passive stereo vision does not have good performance in weak background light, while the active stereo vision is similar to that of structured-light sensing. However, the active sensing such as time of flight sensing and structured-light sensing apply lasers or LEDs to generate the light pattern so the strong background light may disturb the light received by camera, which is why their performance in strong background light is common. Of course, by increasing the output power, the tolerance to the strong background light could be better. As for the detection range, as we know for the photo of target that is far away from the camera will be very small if focal length is not long enough, which will bring difficulties for stereo vision to detect the long range. Similarly, the structured-light also depends on the triangulation of system, so it is also difficult to detect long range. Besides, for structured-light sensing the light power density projected by the light source will be rapidly decreased by the square of distance, which make it more difficult to detect long-range target compared to passive stereo vision. However, the time of flight could be used to detect the long range when the power is enough because the accuracy is only related to the power received by the camera. Limited by the readout speed of camera used in time-of-flight sensing, it is difficult to detect ultra-short range due to extremely propagation time of light. However, in the near range, the structured-light could show extraordinary performance because the power and triangulation are not problem anymore. Theoretically, it could reach several μm and even be used in the microscopy and 3D imaging of physical tissues. Known their performance, we could easily find the advantages of active 3D sensing technology and consider about their suitable applications. Thanks to the availability in middle and long range, the time-of-flight sensing are most suitable for automotive and thanks to the extraordinary accuracy in short range of structured-light sensing, it could be used in 3D printing and face identification.

1.1.3 Comparison between flash sensing and scanning sensing

For scanning sensing, the light source will cover the part of total detected range and then cover the total detected range by light scanning. For flash sensing, the light will project the total detected field at the same time. Assuming the power emitted by scanning and flash sensing are same, it is obvious that scanning sensing has larger power density because the power concentrates on a small region rather than the whole field of flash sensing. Numerically, if the total resolution number of 3D sensing is N, the light density improvement of scanning sensing will be N times. As mentioned before, the accuracy of active 3D sensing is highly dependent on the power density of light. However, for scanning sensing, it may take more time than flash sensing to finish imaging one frame, so the flash sensing may has more time to do temporal averaging process and increase the depth accuracy. In conclusion, the signal to noise ratio (SNR) benefits from scanning sensing could be $\sqrt{N}$. The relation between resolution of 3D sensing and SNR benefit of scanning sensing is plotted in Fig. 1-18.

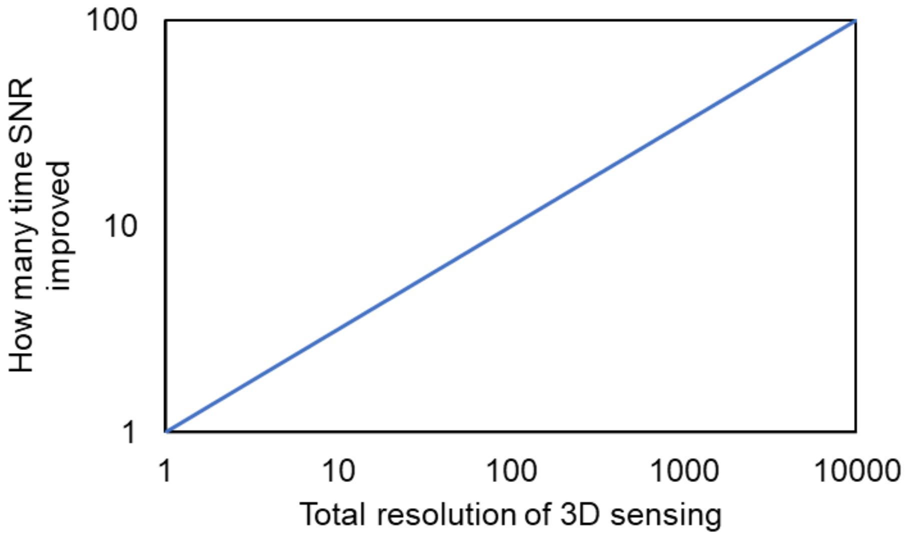

Fig. 1-18. Comparison flash and scanning 3D sensing

1.2 Previous research about beam scanner

Because the scanning 3D sensing could provide larger SNR compared to the flash sensing, the development of beam scanning light source is very important. In this section, several beam scanning techniques will be introduced. Firstly I would like to introduce the criteria of beam scanning techniques. 1) High power: it is easily understandable that higher-power may bring better accuracy and longer detection range, for short-range applications (<5m), the required power is usually <100mW; for middle-range (5-50m) application, the requirement is usually < 10W; while for long-range applications, the power requirement could reach 100W;. 2) Power consumption: Although the power of two scanners is same, the power consumption may have significant extra power consumption difference for beam controlling and beam shaping. Besides, the power efficiency may be another factor to assess the power consumption; 3) Field of view (FoV): Field of view assesses the area that could be covered by the beam scanner. It is obvious larger FoV is better. In most cases, in the short-range detection a very large FoV of >90° ×90° is required; in middle-range detection, the FoV could be a compromised to >60° ×60°; while in long-range detection, the FoV could be further compromised to >30° ×30°. It caused by two factors: In the long-range, for the same angular FoV the covered area (in meter square) will be larger that of short or middle range. Another factors is concerns about the SNR degradation of large FoV in long-range detection; 4) Resolution number: The resolution number determines the quality of final 3D image and resolving ability of two closed object, which is very important for automotive application. Current applied 3D sensing in automotive provides resolution of more than 10,000. 5) Size: The size of beam scanning system should include all parts of the system including the light source, beam scanner and optics. Solid-state beam scanner usually has smaller size. Only small devices could be applied in mobile devices such as mobile phones; 6) Cost and manufacturability: It may depend on the maturity of fabrication process of devices. 7) Scanning speed and stability: Scanning speed may be important to increase the framerate of 3D sensing, which is important for detecting the moving target. For mechanical scanners, the stability may be poor with high scanning speed. Besides, there are many other factors that are also important such as the beam scanning repeatability, long-term availability, light wavelength, environment tolerance, beam divergence, integrability with other parts including receiver and so on.

1.2.1 Mechanical beam scanners

The first beam scanner introduced here is mechanical beam scanner that has been proposed and applied in the real LiDAR applications. It is composed of a light source (Light emitting diodes (LED)[26,27] or Edge emitting lasers (EEL)[28]) and a dynamic scanning mirror. Recently, the micromechanical mirror-based (MEMS) [20,29–32] was proposed and fabricated to replace the convention dynamic mirror. The schematic of dynamic mirror based, and MEMS mirror based beam scanner are shown in Fig. 1-10.

The principle of mechanical scanner is simple: the light emitted from light source will be deflected by a mechanically movable mirror (Bulky or MEMs). It could provide

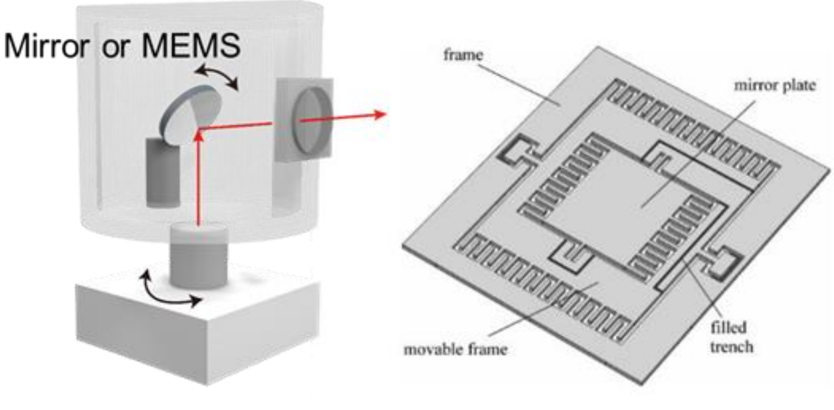

Fig. 1-19. Mechanical scanner [30]

enough resolution and could be fabricated based on current technology. The power is dependent on the used light source. Currently 100W is possible. It is only a temporary method to emerge the urgent requirement of beam scanner. For the large-scale application, it still needs face the difficulties in large size, long-term availability and very high assembling cost. MEMS mirror seems to be a solution for the scanner size and assembling cost. In details, a 1D MEMS mirror with ultra-large FoV of 150° was proposed[33]. However, it could only realize around scanning speed of 400Hz with a small acceptance aperture of <2mm. Besides, for 1D MEMS mirror based LiDAR, the rotation plate is usually needed to realize beam scanning in orthogonal direction, which increase the instability and reduce the scanning speed of LiDAR[34]. To solve this problem, 2D MEMS mirror was also developed. A 2D MEMS scanner with FoV of 65° × 53° was proposed previously [35]. It provides the scanning speed of 21.3kHz for one direction but only 400Hz for the orthogonal direction. In conclusion, MEMS mirror is still not a mature technology with following problems: 1) Conflict between scanning speed and power. Larger aperture means larger light acceptance area. For current high-power light source, the emission beam size is always as large as cm scale, so only the MEMS mirror with larger aperture could accept all the light and realize the long-range detection. However, the scanning speed is inversely proportional to the scale of MEMS mirrors. A cm-scale mirror is difficult to realize kHz-scale beam scanning. Besides cm-scale MEMS mirror currently is still critical for fabrication process, so the bad yield may also increase the expense of MEMS mirrors. 2) Instability and poor long-term reliability: The LiDARs are expected to be used in a car. The violent vibration may affect the stability of MEMS mirror and even destroy the MEMS mirror.

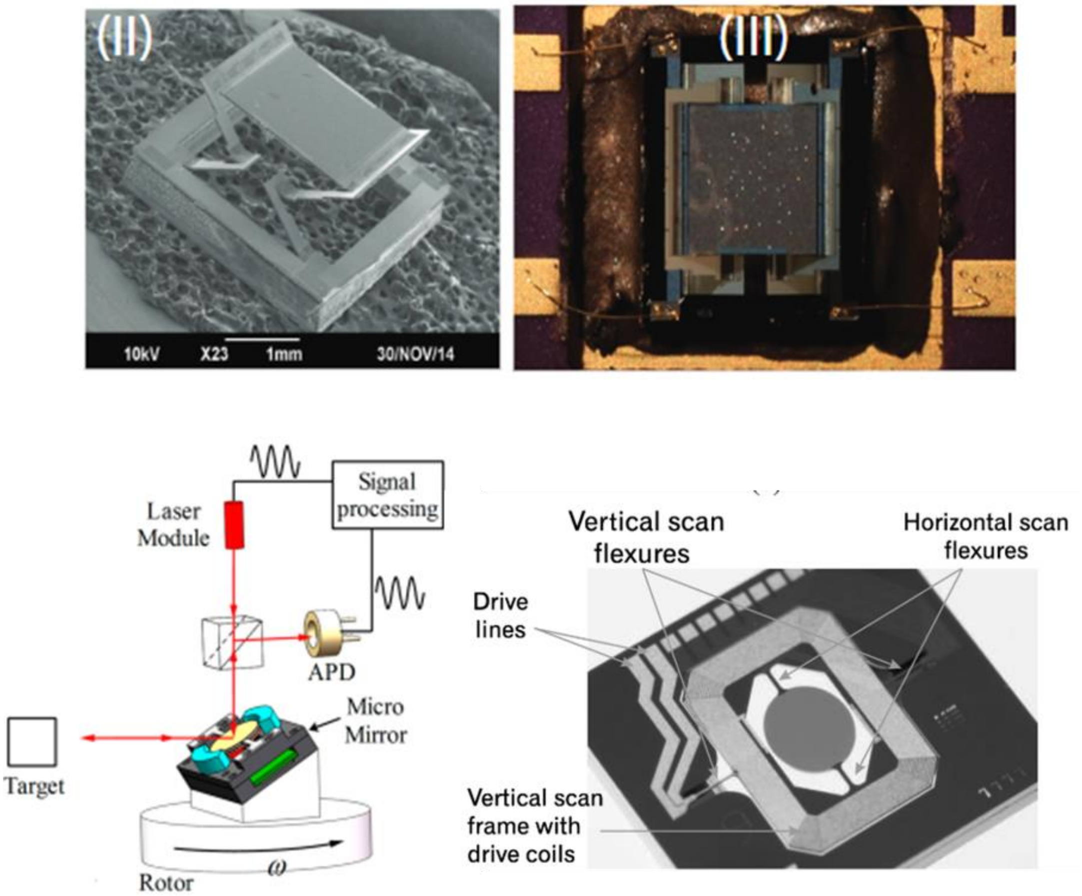

Fig. 1-20 The large-FoV 1D MEMS mirror [33]; Rotor-assisted MEMS scanner [34]; High-speed 2D MEMS mirror [35]

1.2.2 *Non-mechanical beam scanners*

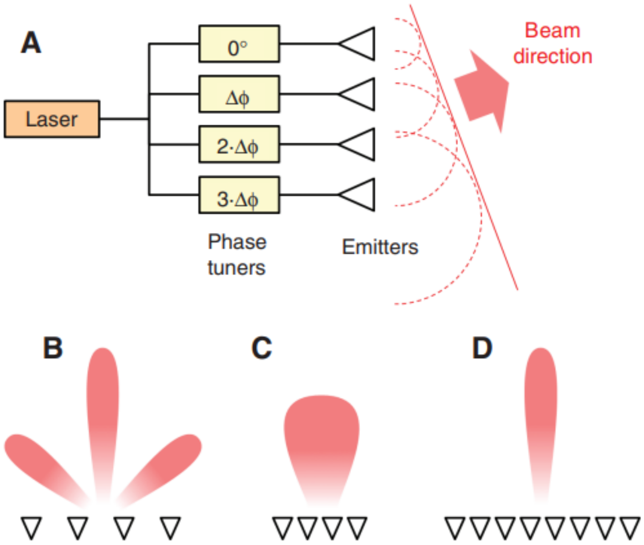

Fig. 1-21. OPA principle [36]

Therefore, non-mechanical beam scanner was thought a more promising solution. A very popular non-mechanical beam scanning technique is optical phase array (OPA) 33)–[44]. Optical phase array was composed a series of optical phase shifters (Phase tuners) as shown in Fig. 1-21 [36]. The light will be split and coupled to the phase shifters. The phase shift will form continuous and linear phase shifting to deflect the beam emission angle from antennas. Therefore, the total scanning range of OPA is determined by the phase tuning range. The phase tuning could be wavelength dependent and wavelength independent. A wavelength dependent OPA was proposed and demonstrated with scanning range of 65° [39]. However, it needs light with broadband wavelength tuning of >460nm, which is almost impractical for real application. Most of OPAs are based on active phase control. The OPA controlled by liquid clad was previously proposed. It realized triple-wavelength beam scanning of >29° [45]. It requires a laser source with triple-wavelength and cannot realize continuous beam scanning, which is also problems for practical applications. Another famous OPA used the thermal effect to control the phase shifters. [40]Due to heat effect, the power consumption will be larger than aforementioned OPAs and its scanning range is also limited by the phase tuning range as 20°. The passive OPA was also recently proposed by using the similar principe of AWG[37]. It could save the energy and increase the control stability, but it only realized scanning range of smaller than 15° limited by the waveguide layout.

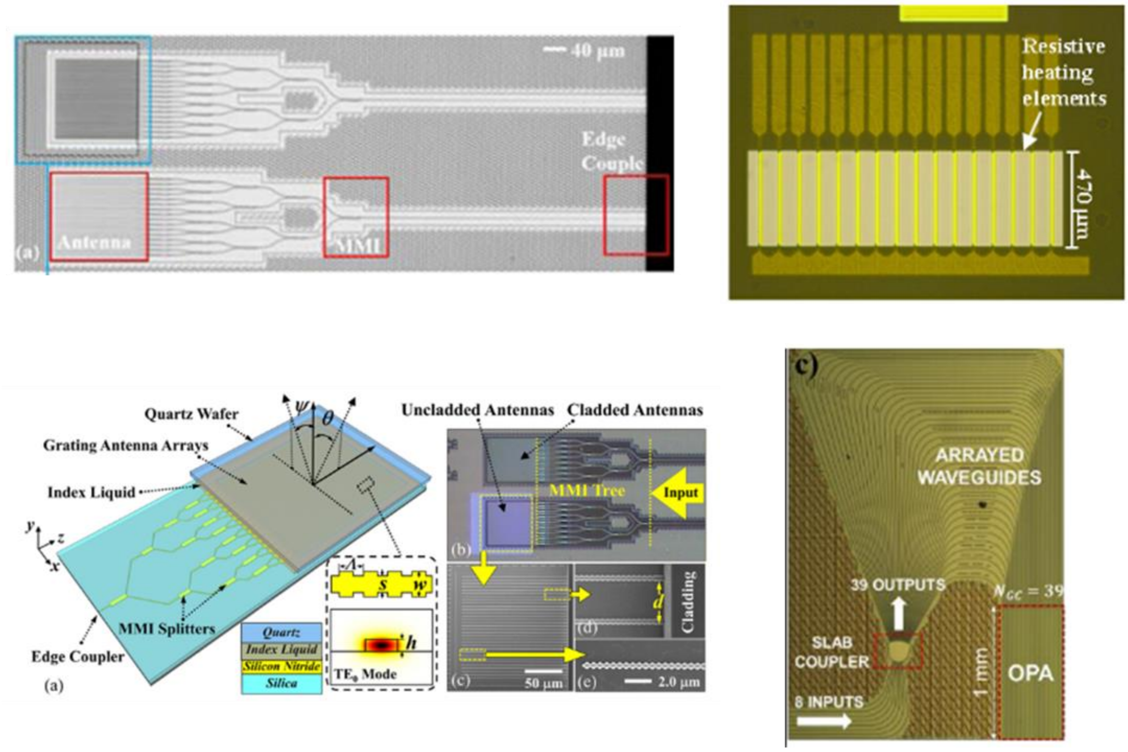

Fig. 1-22. Wavelength-dependent OPA [39]; Thermal-driven OPA [40]; Liquid-clad OPA [45]; Passive OPA [37]

For most 1D OPA, in the orthogonal direction, the Si grating is used to realize beam scanning. However, due to the low dispersion of Si grating. The beam scanning angle in the orthogonal direction is usually small. Therefore, the 2D OPA was proposed to realize the beam scanning in two direction. Nanophotonic phased array was firstly proposed and realized 64 shifters integration. By using this OPA, the multi-order spot will be emitted and steered by 6° ×6° by controlling the phase shifters [38]. It has great potential of larger-scale integration, but the steering angle and beam divergence are still away from real application. Another 2D integration method of OPA is MEMS phase shifters [43]. It was used to realize the beam steering of 6° ×6°, but the light intensity uniformity and scanning range are still not acceptable for real LiDAR application.

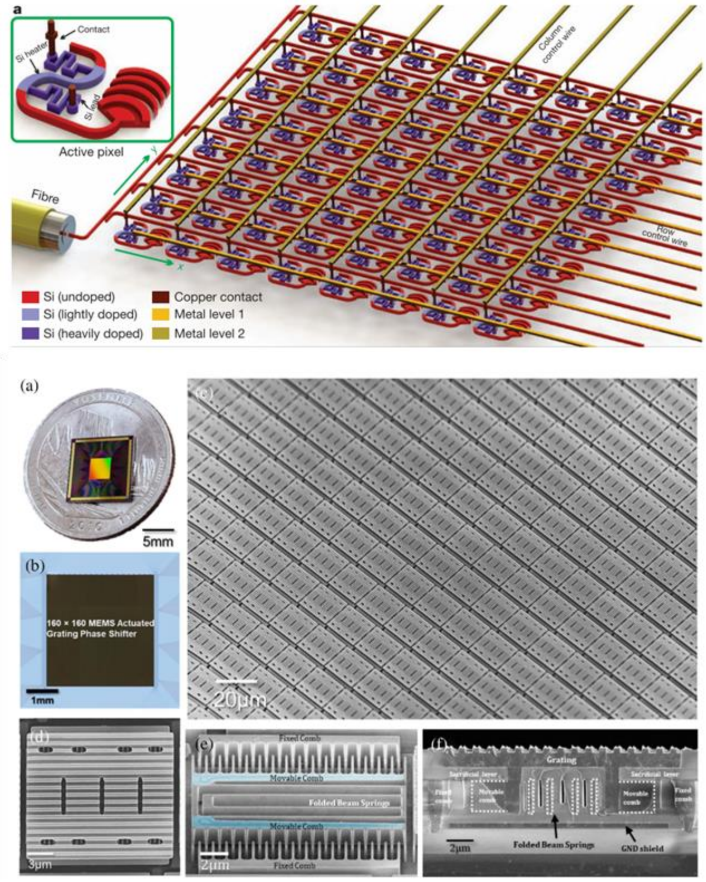

Fig. 1-23 Nanophotonic phased array [38] and MEMS OPA [43]

Previously, an OPA based on multi-pass silicon photonic platform was proposed and demonstrated to realize a large FoV of >70° and narrow beam divergence of 0.15°. However, its beam scanning range in the orthogonal direction is also limited by the dispersion of Si grating [41].

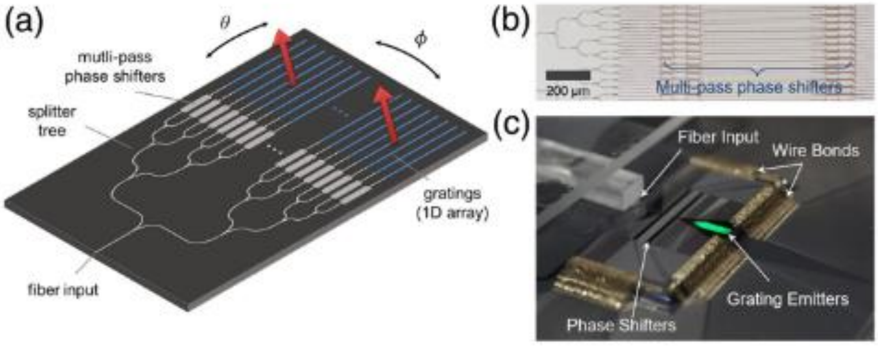

Fig. 1-24 FoV>70° OPA based on multi-pass silicon platform [41]

The fabrication platform for OPA will be conventional Si-based CMOS method for better fabrication availability [36], SiN platform for better beam divergence and better FoV [42] and InP platform for availability of integrating a laser [44].

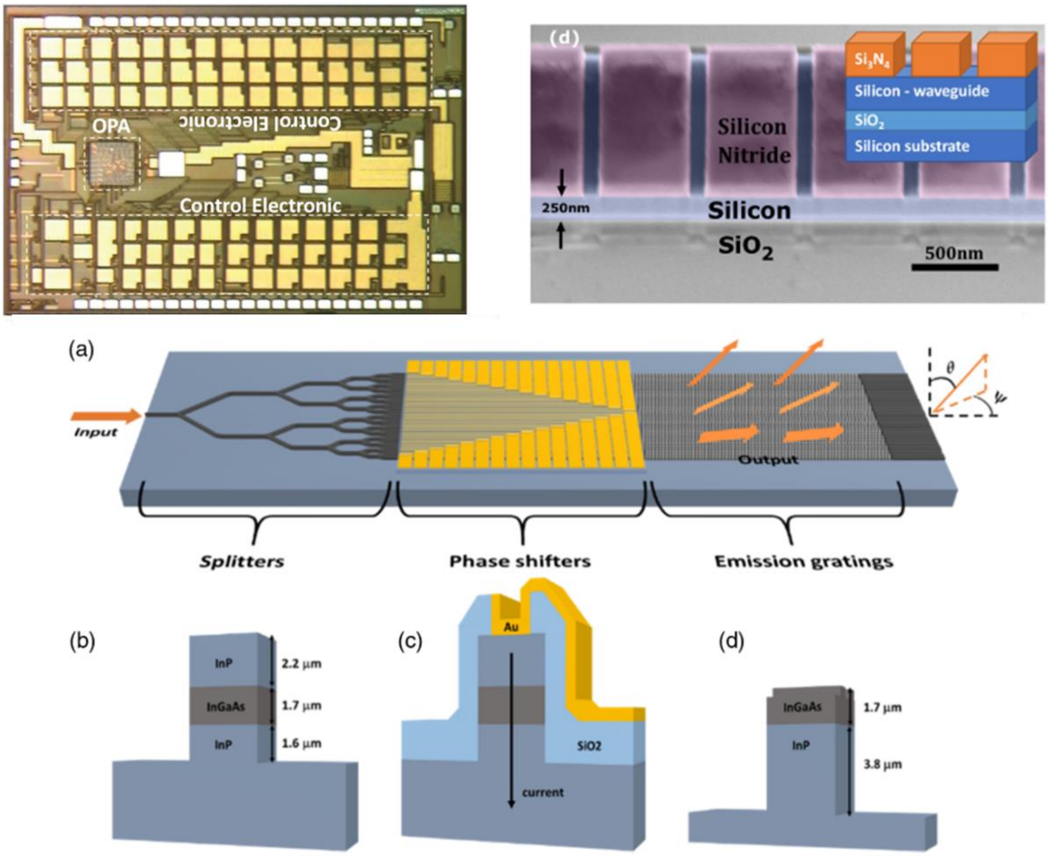

Fig. 1-25. CMOS-based OPA chip [36]; SiN platform for OPA[42]; InP-based OPA [44]

As mentioned before, we could conclude the problems of OPA: 1) Thermally tuning phase shifters may increase the extra power consumption of system; 2) Coupling loss of light source and OPA are always larger than 3dB that significantly increase the power consumption and reduce the detection range; 3) Difficulties in large-scaler and denser phase shifters integration lead to poor beam quality and poor resolution 4) Limited refractive index variation of silicon leads to limited beam scanning range 5) Coupling method of light source and OPA results in difficulties in size miniaturization.

Another important beam steering technique is based on focal plane switch array (FPSA)

[46–48]. A light wave antenna array will be fabricated and placed at the focal plane of a aspheric lens. The light will be coupled into a silicon photonics circuit and switchably coupled to different antennas by thermal or MEMS optics switches. Depending on the diffraction of lens, the emission angle will be steered by switching the operated antennas that was placed in different position in the array. The detailed principle could be found in Fig. 1-26. Vertical cavity surface emitting laser arrays (VCSELs) [49–53] are now also applied to replace the antennas in the array. In this case, the external light coupling is not required anymore. It could be obviously found that the total resolution points are simply equal to the number of antennas in the array.

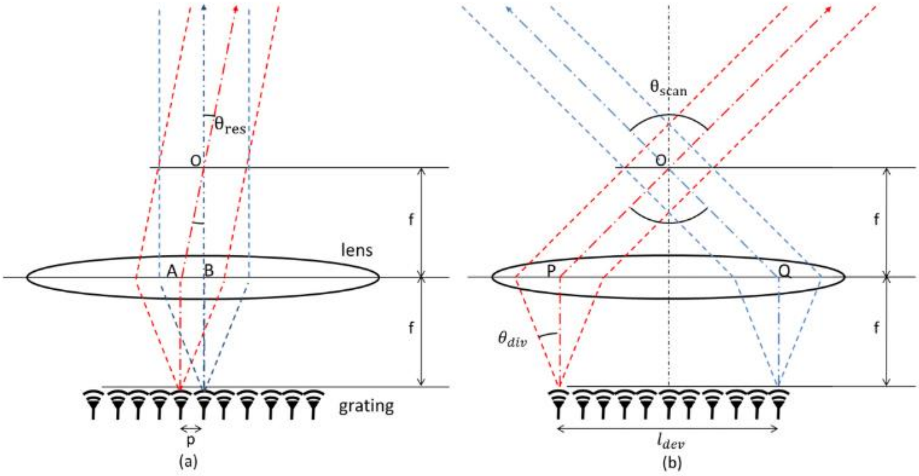

Fig. 1-26. Principle of FPSA [47]

A CMOS-based optical switch array was proposed and demonstrated [47]. It realized 2D integration of 20 switches array. It covers the FoV of around 6° and resolution of 20. It could be also integrated with a receiver on chip [54], which will be easier for realizing solid-state LiDAR. However, the limited resolution should be considered. Previously, a MEMS based FPSA was proposed and demonstrated. It integrates 128×128 switch arrays on the same chip. With a lens of 5mm, it realizes the large FoV of 70°×70° with resolution of more than 10,000. However, the lens used here is a complex lens system because the requirement for large numerical aperture. It will largely increase the module size and make it difficult for being applied in mobile devices. Besides, its resolution angle is larger than 0.5° in both direction, which is also difficult to be used in the long-range LiDAR.

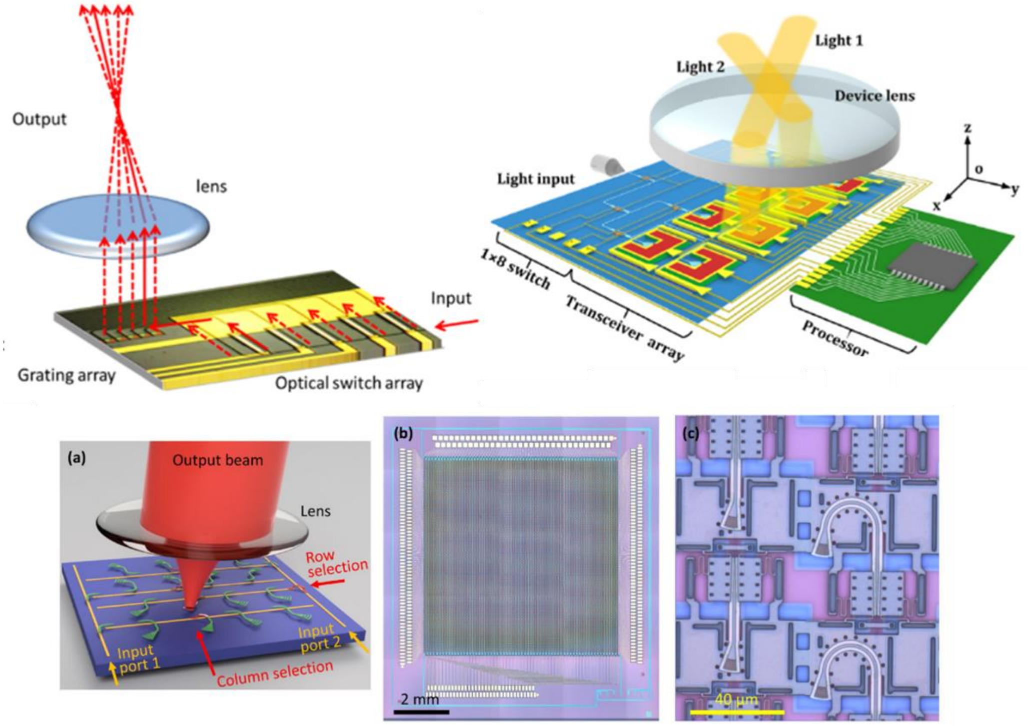

Fig. 1-27 CMOS-based FPSA[47]; Receiver integrated FPSA LiDAR [54]; MEMS-based FPSA [48]

In conclusion, although this method is easy to realize large-angle beam steering by using a larger chip and lens with smaller focal length, the resolution is difficult to realize >1,000 due to the difficulties in large-scale and dense integration. The switch array could be fabricated in 1D or 2D. In many cases, the lens-assisted beam scanning was only used in one direction, while the other beam steering techniques was applied to increase the resolution, such as photonic crystal slow-light waveguide [55] and grating emitters [56]. Also there are many other beam steering technologies such as liquid-based waveguides [57], dually modulated photonic crystals laser array [58], virtually imaged phase array [59] and the combination of these technologies [60]. The current high-impact result of these beam steering technologies was concluded in Figure 1-29. Consequently, the current beam steering technologies mainly has challenges of conflicts of following important performances:

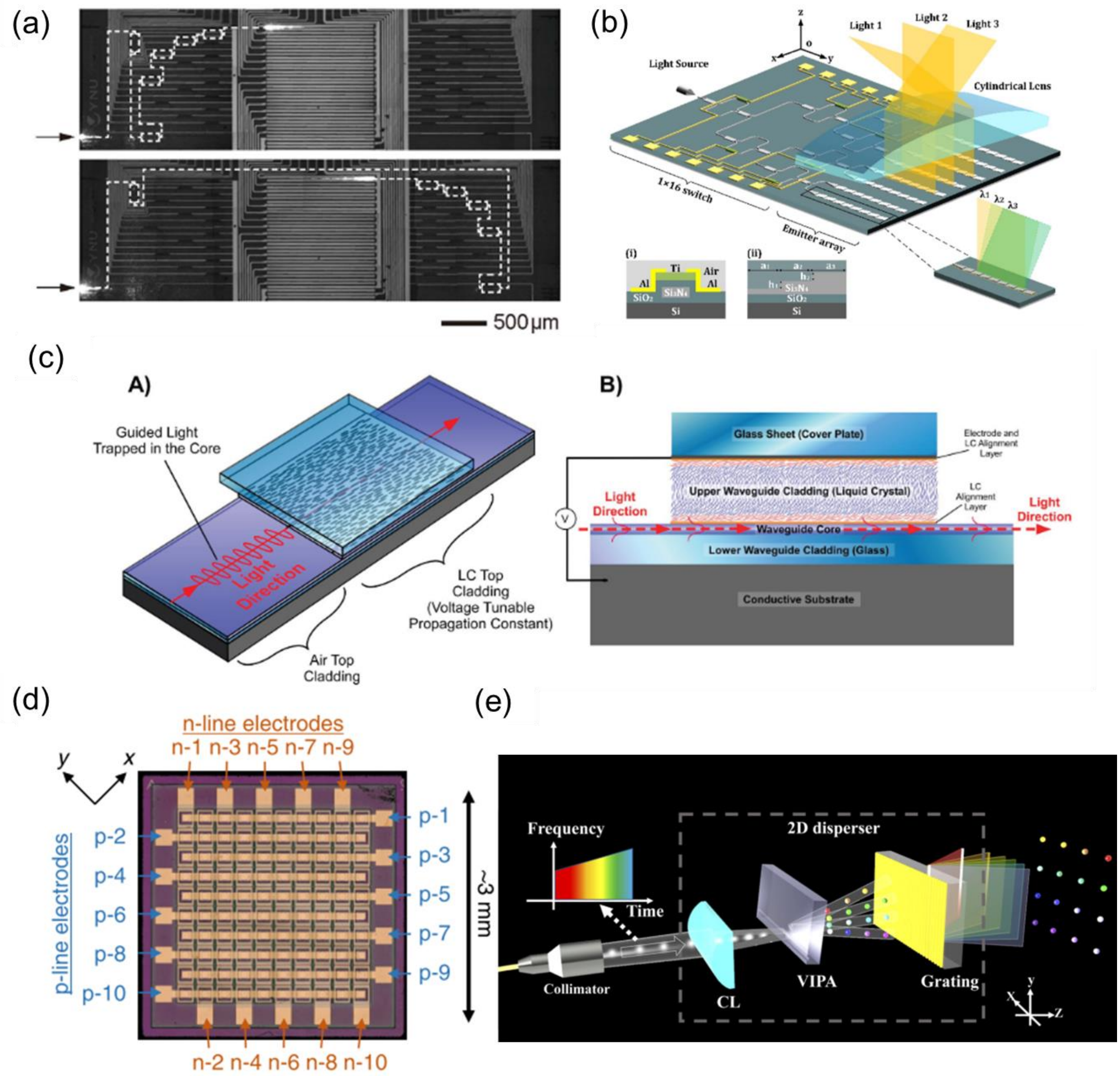

Fig 1-28 Beam scanning based on photonic crystal slow-light waveguide [55] and grating emitters [56], liquid-based waveguides [57], dually modulated photonic crystals laser array [58], virtually imaged phase array [60]

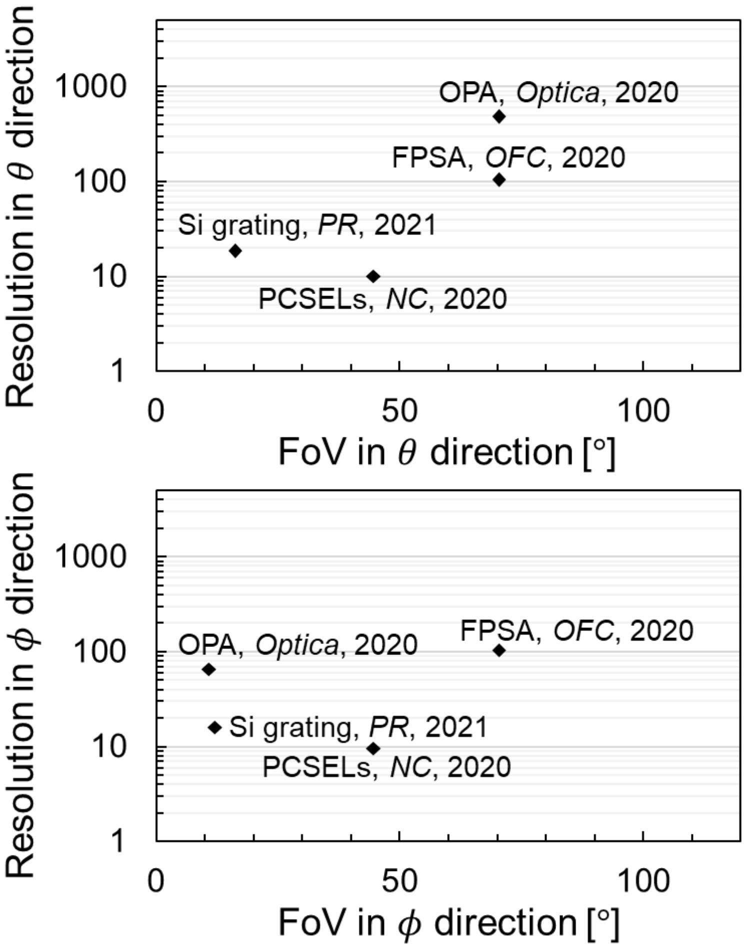

Fig. 1-29. The current result of various beam steering technologies.

1.2.3 Non-mechanical VCSEL beam scanners

To emerge the increasing requirement for non-mechanical beam steering technology, the passive slow-light VCSEL beam scanner based on VCSEL waveguide was proposed and fabricated previously [61–63]. The detailed structured was shown in Fig. 1-30. The beam scanner was fabricated based on the conventional VCSEL wafer, so it could be easily fabricated based on the conventional oxidation-confinement VCSEL fabrication process and could be easily large-scale manufactured with low cost. The beam scanner makes use of the large angular dispersion of VCSEL waveguide.

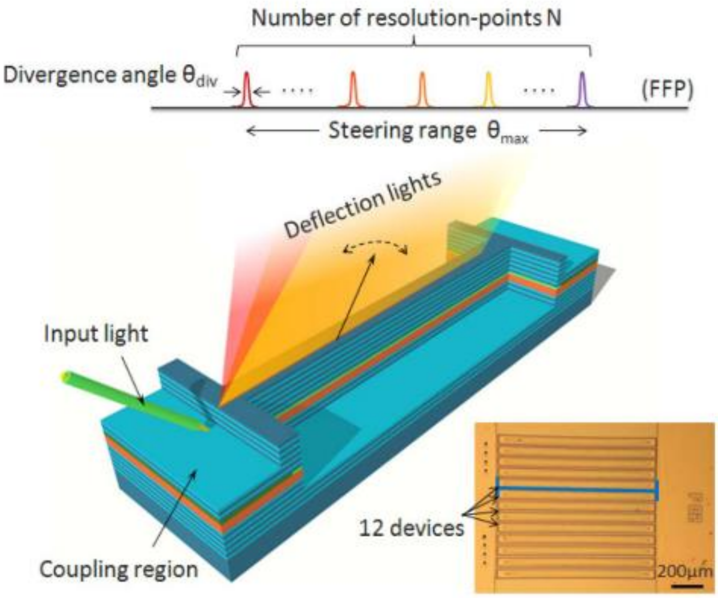

Fig. 1-30. Structure of VCSEL beam scanner [63].

When the light with tunable wavelength is coupled into the scanner, in [63] the large-angle beam steering far-field pattern (FFP) could be realized as shown in Fig. 1-17.

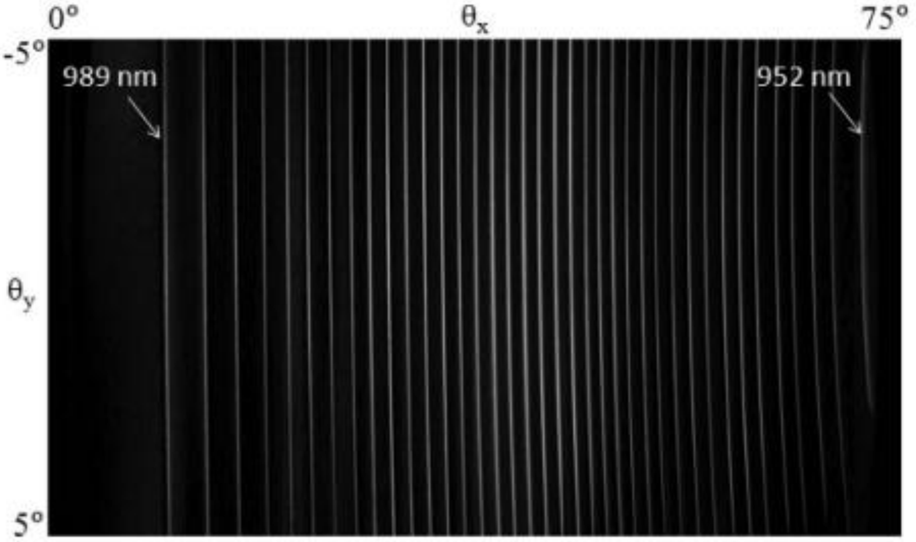

Fig. 1-31. Beam steering FFP [63].

The beam scanning range of >60° could be realized by tuning the coupled wavelength from 952nm to 989nm. Only 37nm tuning range is much smaller than the requirement of silicon-based grating scanner. Besides, the beam divergence is also as small as <0.03°, which is closed to the diffraction limit of the scanner. The total resolution of >1,000 is record number at that time. The problem of this beam scanner is still coupling loss. When a laser with power of >20mW was injected into the scanner, only less than 5mW could be coupled into the scanner. To compensate the coupling loss and propagation loss, the electrodes could be evaporated on the scanner and used to inject current to the scanner. Because the scanner was fabricated on the VCSEL wafer, the quantum wells (QWs) and injection of current could make the beam scanner work as an optical slow-light amplifier [64,65]. Thanks to the slower group velocity, the amplification gain could potentially larger than that in a edge emitting semiconductor optical amplifier. The potential power of >100W could be expected as calculated in Fig. 1-32 [65] by coupling light of several mW. The beam divergence may be a little poorer considering about the current injection uniformity, but it is still less than 0.03° by using a 6-mm long beam scanner. The scanning speed depends on the tuning speed of external tunable laser. MHz is also possible.

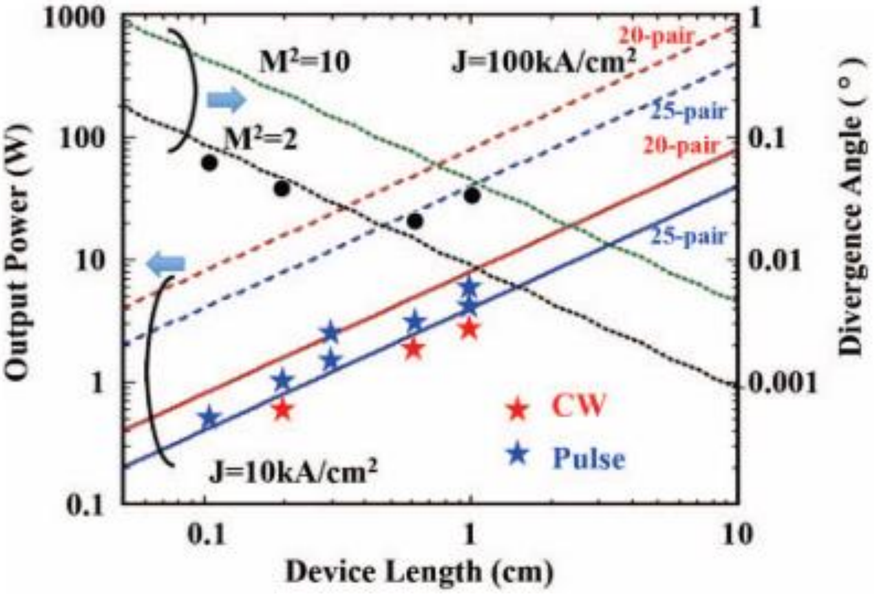

Fig. 1-32. Power and beam divergence expectation of amplification-added VCSEL beam scanner [65].

However due to the limited gain width of scanner, the operation wavelength tuning range was also limited especially for a long beam scanner. Previously, by using a 3-mm long scanner, the beam scanning range was degraded to 27°. For a longer device for smaller beam divergence, the condition might be more critical.

Previously, especially for the application in structured-light sensing and increasing the power density of fan beam. The folded-path beam scanner was proposed and fabricated by Morinaga, et, al.[66]. It used the fold-path aligned VCSEL beam scanner to realize interference between different scanners. The interference will occur at the camera side and make the beam split to different orders as shown in Fig. 1-33. By this structure the dot array pattern could be generated as shown in Fig 1-20 and the power could be also increased by the overlap of beam emitted from each segment. The FoV of 12° ×15° could be covered by only a 0.4mm^2 chip. The number of dots could reach >5,000. However, for the above-mentioned beam scanners, the external light source is required to couple the light with tunable wavelength. It may bring the problems for small-size integration for the application in mobile devices, for example mobile phones.

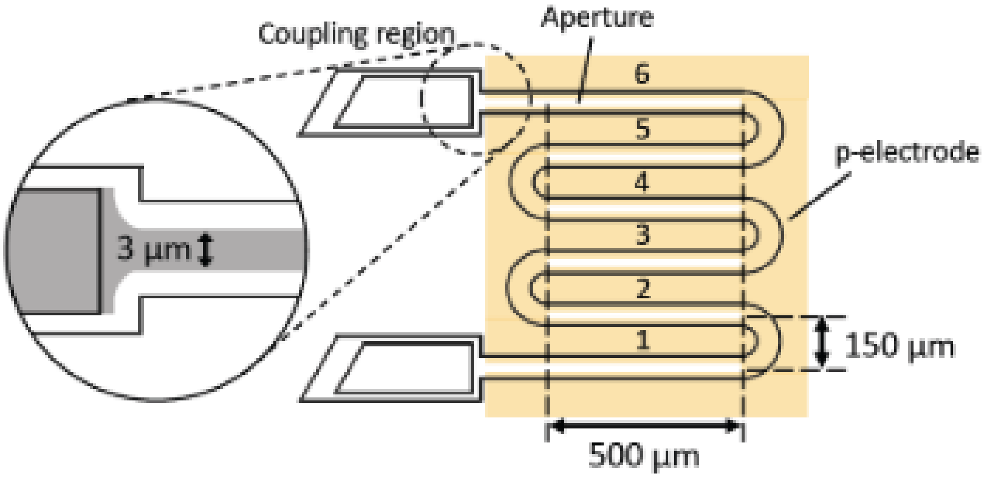

Fig. 1-33. Schematic of folded-path VCSEL amplifier dot projector and [66]

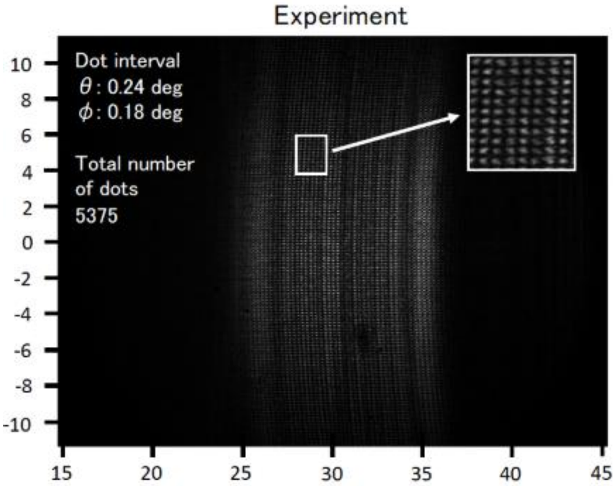

Fig. 1-34. Dot pattern generated by the device [66]

Previously, a slow-light laser was invented, which provides chance to integrate a laser to the beam scanner. The slow-light laser has same structure with beam scanner, the only difference of which is the surface grating should be loaded. It makes use of the slow-light lasing in the beam scanner and etching the grating to realize single mode operation. Several watts has been achieved by a long slow-light laser [67–69], which is enough to excite the beam steering in beam scanner segment. The shorter slow-light laser may be better for driving the beam steering because the electro-thermal efficiency may be larger. Even for the 500um slow-light laser, the power could be 80mW [70]. The schematic of slow-light laser was shown in Fig. 1-35.

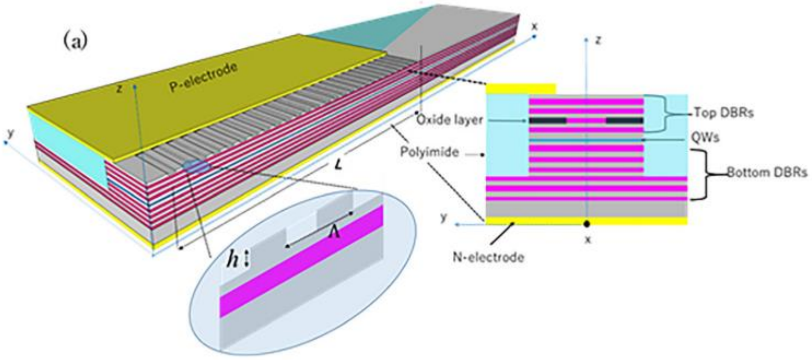

Fig. 1-35. The schematic of slow-light laser [68]

Another problem of VCSEL beam scanner is only 1D beam scanning and lower power density of fan beam. It is obvious, the spot beam has much larger beam intensity than the fan beam. Collimation of fan beam to spot beam will greatly improve the SNR and be significantly helpful to the application in long distance. However, if the fan beam is collimated to spot the FoV in the orthogonal direction will be very small, so it is essential to realize beam scanning in orthogonal direction.

1.3 Research purpose

Considering the problems of current beam scanner, our VCSEL beam scanner has narrow beam divergence, continuous beam steering, high scanning speed and high output power. The purpose of this thesis is to develop the VCSEL beam scanner by:

- Designing and fabricating long-length solitary VCSEL beam scanner for narrow beam divergence of <0.3°;
- Integrating a seed VCSEL to solitary VCSEL beam scanner for mm-scale compact packaging size;
- Improving the FoV and resolution to > 100° and >1,000 for both solitary beam scanner and beam scanner integrated to a seed VCSEL by introducing DOE-based optics;
- Designing and fabricating VCSEL beam scanners array to realize 2D spot-beam scanning for higher beam intensity;
- Improving the FoV and resolution to > 70° × 30° and >1,000 for 2D beam scanning module by introducing DOE-based optics;
- Applying the VCSEL beam scanners in 3D sensing including low-power-consumption structured-light sensing and ToF LidAR.

1.4 Organization of the thesis

- **Chapter 1**: The application of 3D sensing and previous work about beam scanner were introduced.
- **Chapter 2**: The principle, fabrication process and experimental result of solitary VCSEL beam and it integration to seed laser.
- **Chapter 3**: The method and experimental result of using counter-propagation integration and diffractive optics to enhance FoV and resolution of beam scanner will be proposed. and demonstrated.
- **Chapter 4**: The method and experimental result of 2D beam steering based on VCSEL beam scanner will be proposed and demonstrated. Its field of view and resolution will also be enhanced.
- **Chapter 5**: The VCSEL beam scanner in practical 3D sensing, such as structured-light sensing and LiDAR, will be demonstrated.
- **Chapter 6**: The prospective and potential of VCSEL beam scanner will be discussed and the thesis will be concluded.

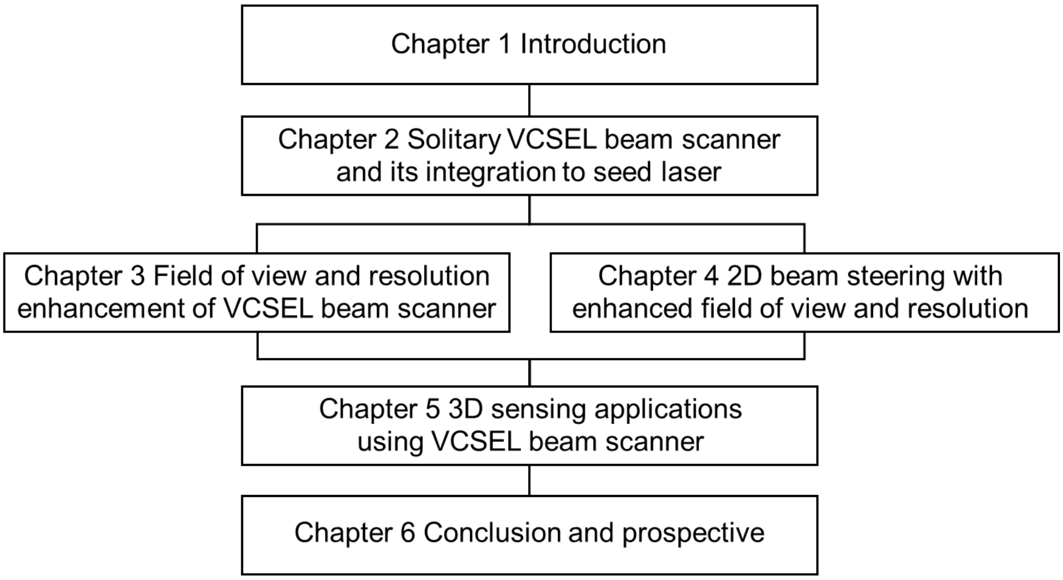

Fig 1-36 Organization frame of the thesis

Reference in Chapter 1

1-1. Yole developpment, *3D Imaging and Sensing – Technology and Market Trends 2021* (2021).

1-2. "https://support.apple.com/ja-jp/HT208109," .

1-3. B. D. Padullaparthi, J. Tatum, and K. Iga, *VCSEL Industry: Communication and Sensing* (John Wiley ¥& Sons, 2021).

1-4. https://corporatefinanceinstitute.com/resources/knowledge/other/intelligent-manufacturing-system-ims/, "Intelligent Manufacturing System (IMS)," .

1-5. Intel, *Intel RealSense White Paper* (n.d.).

1-6. J. Geng, "Structured-light 3D surface imaging: a tutorial," Adv. Opt. Photonics **3**(2), 128 (2011).

1-7. Y. An, J.-S. Hyun, and S. Zhang, "Pixel-wise absolute phase unwrapping using geometric constraints of structured light system," Opt. Express **24**(16), 18445–18459 (2016).

1-8. Y. Zhang, Z. Xiong, Z. Yang, and F. Wu, "Real-time scalable depth sensing with hybrid structured light illumination," IEEE Trans. Image Process. **23**(1), 97–109 (2014).

1-9. S. Zhang, "High-speed 3D shape measurement with structured light methods: A review," Opt. Lasers Eng. **106**(March), 119–131 (2018).

1-10. Z. Song, S. Tang, F. Gu, C. Shi, and J. Feng, "DOE-based structured-light method for accurate 3D sensing," Opt. Lasers Eng. **120**(December 2018), 21–30 (2019).

1-11. Z. Mor and B. Morgenstein, "Overlapping pattern projector," (2018).

1-12. S. Merlo, F. Carpignano, D. Riccardi, G. Rigamonti, and M. Norgia, "Infrared structured light generation by optical MEMS and application to depth perception," 4th IEEE Int. Work. Metrol. AeroSpace, Metroaerosp. 2017 - Proc. 518–522 (2017).

1-13. M. Beer, J. F. Haase, J. Ruskowski, and R. Kokozinski, "Background light rejection in SPAD-based LiDAR sensors by adaptive photon coincidence detection," Sensors (Switzerland) **18**(12), (2018).

1-14. S. Bellisai, D. Bronzi, F. A. Villa, S. Tisa, A. Tosi, and F. Zappa, "Single-photon pulsed-light indirect time-of-flight 3D ranging," Opt. Express **21**(4), 5086 (2013).

1-15. M. Okano and C. Chong, "Swept Source Lidar: simultaneous FMCW ranging and nonmechanical beam steering with a wideband swept source," Opt. Express **28**(16), 23898 (2020).

1-16. G. Shutter and F. Lidar, "Our Technology What is 3D Global Shutter Flash," (n.d.).

1-17. I. Poberezhskiy, A. Johnson, D. Chang, E. Ek, D. Natzic, G. Spiers, S. Penniman, and B. Short, "Flash lidar performance testing: configuration and results," Laser Radar Technol. Appl. XVII **8379**(May 2012), 837905 (2012).

1-18. B. I. Erkmen, "Computational ghost imaging for remote sensing," J. Opt. Soc. Am. A **29**(5), 782 (2012).

1-19. B. Schwarz, "Lidar: Mapping the world in 3D," Nat. Photonics **4**(7), 429–430 (2010).

1-20. H. W. Yoo, N. Druml, D. Brunner, C. Schwarzl, T. Thurner, M. Hennecke, and G. Schitter, "MEMS-based lidar for autonomous driving," Elektrotechnik und Informationstechnik **135**(6), 408–415 (2018).

1-21. C. V. Poulton, A. Yaacobi, D. B. Cole, M. J. Byrd, M. Raval, D. Vermeulen, and

M. R. Watts, "Coherent solid-state LIDAR with silicon photonic optical phased arrays," Opt. Lett. **42**(20), 4091 (2017).

1-22. R. Tetsuya, T. Tamanuki, H. Ito, H. Abe, R. Kurahashi, M. Seki, M. Ohtsuka, N. Yokoyama, M. Okano, and T. Baba, "Si photonic crystal optical antenna serial array and frequency-modulated continuous-wave light detection and ranging action," Appl. Phys. Lett. **119**(23), 231103 (2021).

1-23. A. McCarthy, R. J. Collins, N. J. Krichel, V. Fernández, A. M. Wallace, and G. S. Buller, "Long-range time-of-flight scanning sensor based on high-speed time-correlated single-photon counting," Appl. Opt. **48**(32), 6241–6251 (2009).

1-24. M. J. Sun, M. P. Edgar, G. M. Gibson, B. Sun, N. Radwell, R. Lamb, and M. J. Padgett, "Single-pixel three-dimensional imaging with time-based depth resolution," Nat. Commun. **7**(May), 1–6 (2016).

1-25. Y. Jiang, S. Karpf, and B. Jalali, "Time-stretch LiDAR as a spectrally scanned time-of-flight ranging camera," Nat. Photonics **14**(1), 14–18 (2020).

1-26. M. KOYAMA, "Light source module for LED lidar," in *25th International Laser Radar Conference, 2010* (2010), pp. 166–169.

1-27. T. Shiina, "LED mini-lidar for air and dust monitoring," in *International Symposium on Photoelectronic Detection and Imaging 2013: Laser Sensing and Imaging and Applications* (2013), **8905**, p. 890533.

1-28. C. Liu, P. Zhang, M. Xiang, X. Ma, C. Jiang, B. Tang, Q. Lu, and W. Guo, "Single-mode surface-emitting DFB lasers with a large-area oxidized aperture based on the surface grating," Opt. Lett. **45**(13), 3573 (2020).

1-29. D. Wang, C. Watkins, and H. Xie, "MEMS mirrors for LiDAR: A review," Micromachines **11**(5), 456 (2020).

1-30. S. T. S. Holmström, U. Baran, and H. Urey, "MEMS laser scanners: A review," J. Microelectromechanical Syst. **23**(2), 259–275 (2014).

1-31. H. Schenk, J. Grahmann, T. Sandner, M. Wagner, U. Dauderstädt, and J. U. Schmidt, "Micro mirrors for high-speed laser deflection and patterning," Phys. Procedia **56**(C), 7–18 (2014).

1-32. C. Winter, L. Fabre, F. Lo Conte, L. Kilcher, F. Kechana, N. Abelé, and M. Kayal, "Micro-beamer based on MEMS micro-mirrors and laser light source," Procedia Chem. **1**(1), 1311–1314 (2009).

1-33. X. Zhang, S. J. Koppal, R. Zhang, L. Zhou, E. Butler, and H. Xie, "Wide-angle structured light with a scanning MEMS mirror in liquid," Opt. Express **24**(4), 3479 (2016).

1-34. L. Ye, G. Zhang, and Z. You, "Large-aperture kHz operating frequency ti-alloy based optical micro scanning mirror for lidar Application," Micromachines **8**(4), (2017).

1-35. A. D. Yalcinkaya, H. Urey, D. Brown, T. Montague, and R. Sprague, "Two-axis electromagnetic microscanner for high resolution displays," J. Microelectromechanical Syst. **15**(4), 786–794 (2006).

1-36. M. J. R. Heck, "Highly integrated optical phased arrays: Photonic integrated circuits for optical beam shaping and beam steering," Nanophotonics **6**(1), 93–107 (2017).

1-37. D. Pastor, L. A. Bru, D. J. Goodwill, and E. Bernier, "Optical-phased array beam-steering using multi-input slab coupler in silicon nitride waveguides," in *Optical Fiber Communication Conference (OFC) 2021* (2021), p. W1D.4.

1-38. J. Sun, E. Timurdogan, A. Yaacobi, E. S. Hosseini, and M. R. Watts, "Large-scale nanophotonic phased array," Nature **493**(7431), 195–199 (2013).

1-39. H. Wang, Z. Chen, C. Sun, S. Deng, X. Tang, L. Zhang, R. Jiang, W. Shi, Z. Chen, Z. Li, and A. Zhang, "Broadband silicon nitride nanophotonic phased arrays for wide-angle beam steering," Opt. Lett. **46**(2), 286 (2021).

1-40. J. K. Doylend, M. J. R. Heck, J. T. Bovington, J. D. Peters, L. A. Coldren, and J. E. Bowers, "Two-dimensional free-space beam steering with an optical phased array on silicon-on-insulator," Opt. Express **19**(22), 21595–21604 (2011).

1-41. S. A. Miller, Y.-C. Chang, C. T. Phare, M. C. Shin, M. Zadka, S. P. Roberts, B. Stern, X. Ji, A. Mohanty, O. A. Jimenez Gordillo, U. D. Dave, and M. Lipson, "Large-scale optical phased array using a low-power multi-pass silicon photonic platform," Optica **7**(1), 3 (2020).

1-42. M. Zadka, Y.-C. Chang, A. Mohanty, C. T. Phare, S. P. Roberts, and M. Lipson, "On-chip platform for a phased array with minimal beam divergence and wide field-of-view," Opt. Express **26**(3), 2528–2534 (2018).

1-43. Y. Wang, G. Zhou, X. Zhang, K. Kwon, P.-A. Blanche, N. Triesault, K. Yu, and M. C. Wu, "2D broadband beamsteering with large-scale MEMS optical phased array," Optica **6**(5), 557 (2019).

1-44. J. Midkiff, K. M. Yoo, J.-D. Shin, H. Dalir, M. Teimourpour, and R. T. Chen, "Optical phased array beam steering in the mid-infrared on an InP-based platform," Optica **7**(11), 1544 (2020).

1-45. B. Li, C. Sun, H. Wang, Z. Chen, X. Nie, S. Deng, L. Yang, and A. Zhang, "Liquid-cladded optical phased array for a single-wavelength beam steering," Opt. Lett. **46**(19), 4948 (2021).

1-46. C. Li, X. Cao, K. Wu, X. Li, and J. Chen, "Lens-based integrated 2D beam-steering device with defocusing approach and broadband pulse operation for Lidar application," Opt. Express **27**(23), 32970 (2019).

1-47. D. Inoue, T. Ichikawa, A. Kawasaki, and T. Yamashita, "Demonstration of a new optical scanner using silicon photonics integrated circuit," Opt. Express **27**(3), 2499 (2019).

1-48. X. Zhang, K. Kwon, J. Henriksson, J. Luo, and M. C. Wu, "Large-scale Silicon Photonics Focal Plane Switch Array for Optical Beam Steering," in *Optical Fiber Communication Conference (OFC) 2021* (2021), pp. 5–7.

1-49. K. J. Ebeling, R. Michalzik, and H. Moench, "Vertical-cavity surface-emitting laser technology applications with focus on sensors and three-dimensional imaging," Jpn. J. Appl. Phys. **57**(8), (2018).

1-50. M. Kuramoto, S. Kobayashi, T. Akagi, K. Tazawa, K. Tanaka, T. Saito, and T. Takeuchi, "High-output-power and high-temperature operation of blue GaN-based vertical-cavity surface-emitting laser," Appl. Phys. Express **11**(11), 8–11 (2018).

1-51. K. Iga, "Forty years of vertical-cavity surface-emitting laser: Invention and innovation," Jpn. J. Appl. Phys. **57**(8), (2018).

1-52. M. Kuramoto, S. Kobayashi, T. Akagi, K. Tazawa, K. Tanaka, T. Saito, and T. Takeuchi, "Enhancement of slope efficiency and output power in GaN-based vertical-cavity surface-emitting lasers with a SiO2-buried lateral index guide," Appl. Phys. Lett. **112**(11), (2018).

1-53. M. Kuramoto, S. Kobayashi, T. Akagi, K. Tazawa, K. Tanaka, K. Nakata, and T. Saito, "laser arrays," (2019).

1-54. C. Li, K. Wu, X. Cao, G. Zhang, X. Li, and J. Chen, "Monolithic transceiver for lens-assisted beam-steering Lidar," Opt. Lett. **46**(22), 5587 (2021).

1-55. H. Ito, Y. Kusunoki, J. Maeda, D. Akiyama, N. Kodama, H. Abe, R. Tetsuya, and T. Baba, "Wide beam steering by slow-light waveguide gratings and a prism lens," Optica **7**(1), 47 (2020).

1-56. C. Li, X. Cao, K. Wu, G. Qiu, M. Cai, G. Zhang, X. Li, and J. Chen, "Blind zone-suppressed hybrid beam steering for solid-state Lidar," Photonics Res. **9**(9), 1871–1880 (2021).

1-57. S. R. Davis, G. Farca, S. D. Rommel, S. Johnson, and M. H. Anderson, "Liquid crystal waveguides: new devices enabled by >1000 waves of optical phase control," Emerg. Liq. Cryst. Technol. V **7618**(July), 76180E (2010).

1-58. R. Sakata, K. Ishizaki, M. De Zoysa, S. Fukuhara, T. Inoue, Y. Tanaka, K. Iwata, R. Hatsuda, M. Yoshida, J. Gelleta, and S. Noda, "Dually modulated photonic crystals enabling high-power high-beam-quality two-dimensional beam scanning lasers," Nat. Commun. **11**(1), 1–10 (2020).

1-59. V. Voskerchyan, Y. Tian, F. M. Soares, and F. J. Diaz-otero, "Photonic-Integrated and Highly-Scalable FMCW LiDAR Concept based on Titled Grating Couplers," (1), 2–5 (n.d.).

1-60. Z. Li, Z. Zang, Y. Han, L. Wu, and H. Y. Fu, "Solid-state FMCW LiDAR with two-dimensional spectral scanning using a virtually imaged phased array," Opt. Express **29**(11), 16547 (2021).

1-61. X. Gu, T. Shimada, A. Fuchida, A. Matsutani, A. Imamura, and F. Koyama, "Beam steering in GaInAs/GaAs slow-light Bragg reflector waveguide amplifier," Appl. Phys. Lett. **99**(21), 211107 (2011).

1-62. X. Gu, T. Shimada, and F. Koyama, "Giant and high-resolution beam steering using slow-light waveguide amplifier," Opt. Express **19**(23), 22675 (2011).

1-63. X. Gu, T. Shimada, A. Matsutani, and F. Koyama, "Miniature nonmechanical beam deflector based on bragg reflector waveguide with a number of resolution points larger than 1000," IEEE Photonics J. **4**(5), 1712–1719 (2012).

1-64. M. Nakahama, X. Gu, A. Matsutani, T. Sakaguchi, and F. Koyama, "High Power Non-mechanical Beam Scanner based on VCSEL Amplifier," 2016 21st Optoelectron. Commun. Conf. held jointly with 2016 Int. Conf. Photonics Switch. **1**, 4–6 (2016).

1-65. Z. Ho, J. Hayakawa, K. Shimura, K. Kondo, X. Gu, A. Matsutani, A. Murakami, and F. Koyama, "High Power and High Beam Quality VCSEL Amplifier," Conf. Dig. - IEEE Int. Semicond. Laser Conf. **2018-Septe**, 229–230 (2018).

1-66. M. Morinaga, X. Gu, K. Shimura, A. Matsutani, and F. Koyama, "Compact Dot Projector based on Folded Path VCSEL Amplifier for Structured Light Sensing," 2019 Conf. Lasers Electro-Optics, CLEO 2019 - Proc. **1**(c), 4–5 (2019).

1-67. A. M. A. Hassan, M. Ahmed, M. Nakahama, and F. Koyama, "High-power, quasi-single-mode vertical-cavity surface-emitting laser with near-diffraction-limited and low-divergence beam," Jpn. J. Appl. Phys. **59**(9), 90904 (2020).

1-68. A. M. A. Hassan, X. Gu, M. Nakahama, S. Shinada, M. Ahmed, and F. Koyama, "High power surface grating slow-light VCSEL," Appl. Phys. Express **14**(9), 092006 (2021).

1-69. A. M. A. Hassan, X. Gu, M. Nakahama, S. Shinada, M. Ahmed, and F. Koyama, "High-power operations of single-mode surface grating long oxide aperture VCSELs," Appl. Phys. Lett. **119**(19), 191103 (2021).

1-70. S. Hu, A. Hassan, X. Gu, M. Nakahama, and F. Koyama, "Surface grating loaded

VCSEL with single mode power of over 80 mW," IEICE Electron. Express **18**(11), 20210202 (2021).

Chapter 2

Solitary VCSEL beam scanner and its integration to seed laser

In this chapter, the details about operation principle, optimized design, fabrication process and experimental characteristics of VCSEL beam scanner will be discussed. The brief introduction of slow-light laser will also be shown. The important thing is the operation principle, optimized design and fabrication of integration of slow-light seed laser and VCSEL beam scanner. Its optical and electrical characteristics will also be discussed.

2.1 Solitary VCSEL beam scanner

2.1.1 Principle of solitary VCSEL beam scanner

The schematic of solitary VCSEL beam scanner is shown in Fig. 2-1. It was fabricated based on the conventional VCSEL wafer. In my study, I chose to use the epi wafer with resonance wavelength of 855nm. The wafer was deposited layer by layer using metal organic chemical vapor deposition (MOCVD) on the GaAs substrate. The composition of each layer is $Al_xGa_{1-x}As$, which is compatible for 855nm-band lasing. By repeatedly deposition of $Al_xGa_{1-x}As$ layer with different x and different thickness the distributed bragg reflector (DBRs) will be formed. A number of pairs of DBRs will form the top and bottom DBRs, which sandwich a $Al_xGa_{1-x}As$ quantum wells (QWs). Thanks to the high-reflectivity of top and bottom DBRs, the resonance will formed between the top and bottom DBRs at specialized wavelength λ_r (Resonance wavelength). It also leads to the

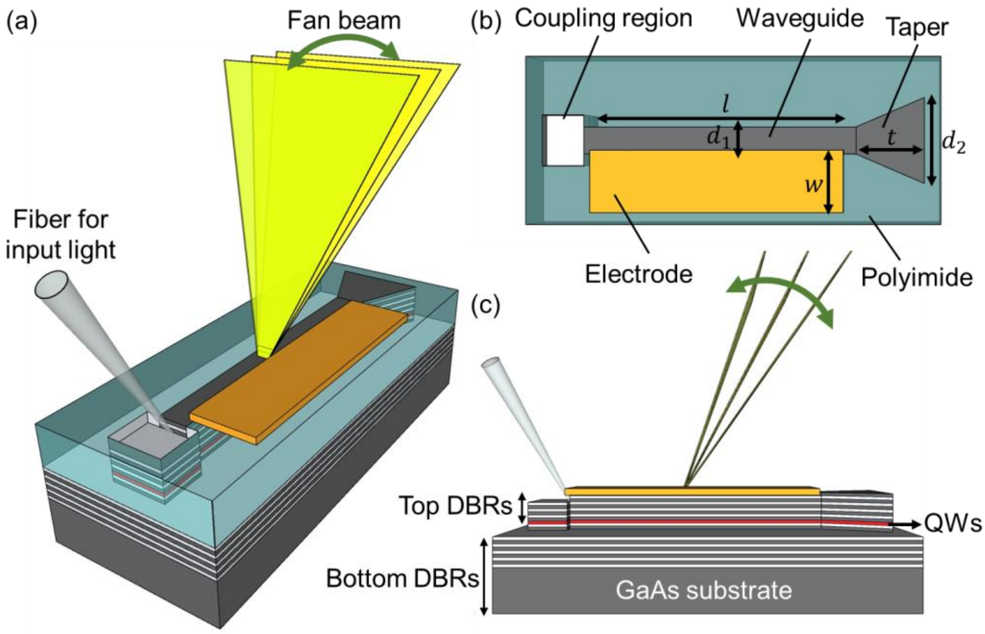

Fig. 2-1. The schematic of VCSEL beam scanner

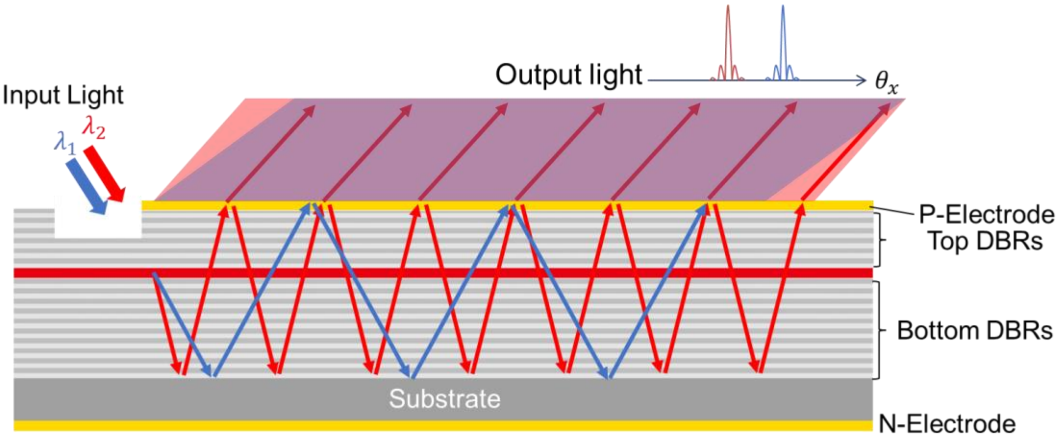

Fig. 2-2. Zigzag propagation in the VCSEL waveguide of two wavelength

narrow-width single mode lasing of VCSEL. In other sides, thanks to the high reflectivity of top and bottom DBRs, if the light was coupled to the resonance, the device could also work as a flat VCSEL waveguide, the light will propagate in zigzag path. It turns out that the light group velocity is slower than that of straight propagation in the same material, so the light propagating in this mode was called slow-light mode as shown in Fig. 2-2. The difference of our VCSEL waveguide and conventional flat waveguide is the top reflectivity. In our case the top reflectivity may be only around 99%, which provides possibility to make light emit from the top surface when propagating in the waveguide. It also leads to another difference from conventional passive waveguide: Current injection is needed to compensate the emission when the light propagating in the scanner. Actually, not only compensating the emission loss but amplifying could be expected by injecting current above the threshold of VCSEL lasing. When the incident light was coupled to the scanner, the threshold of vertical lasing will get larger with incident power increasing. Another property of the slow-light mode in the VCSEL waveguide is high dispersion. In Fig. 2-2 It could be found that when the wavelength of coupled light tuning, the propagation direction in the waveguide will be deflected and therefore the emission angle from the surface will also be tuned. The relation between wavelength λ_{in} and emission angle θ_d from surface has been deviated as Eq. 2-1,

$$sin\theta_d = n_{wg}\sqrt{1-\lambda_{in}^2/\lambda_r^2} \tag{2-1}$$

where n_{wg} is the refractive index of top DBRs. It could be seen that only the coupled light with wavelength of smaller than λ_r is meaningful, so the λ_r is also called cutoff wavelength of this wafer. Moreover, the Photoluminescence (PL) wavelength of QWs also should be designed away from λ_r to make the effective amplification spectrum as large as possible. This relation between wavelength λ_{in} and emission angle θ_d could be also plotted straighter as Fig. 2-3. It is found when the λ_{in} is closed to λ_r, the scanning efficiency is very large, but it is not good to choose the operation wavelength at this region because when the wavelength is closed to the resonant wavelength and injecting current above the threshold the waveguide may self lase. It will leads to reduction of output power. Also set PL wavelength away from the resonant wavelength

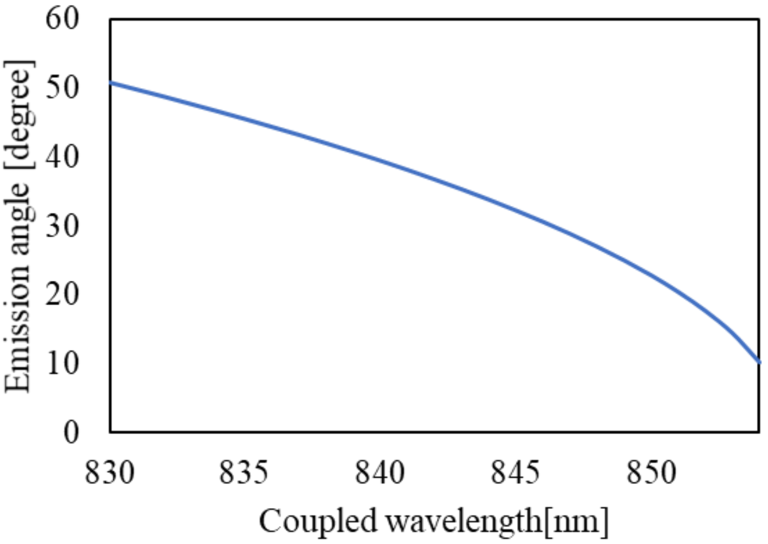

Fig. 2-3. Zigzag propagation in the VCSEL waveguide of two wavelength

could also avoid the self lasing to an extent. Normally, the range from 830nm to 845nm may be chosen as operation range, where the scanning efficiency is almost linear as 1.24°/nm that is much larger than that of silicon-based grating.

After discussion of the principle of beam scanning by using VCSEL waveguide/amplifier. The beam divergence is another important issue that should be discussed. The beam divergence should be related to the aperture size of beam scanner. As shown in Fig. 2-4. The diffraction limited beam divergence θ_{div} of an aperture $l \times d_0$ could be calculated as Eq. 2-2 [1–3], d_0 is oxidized aperture width,

$$sin\theta_{div} = M^2\lambda_{in}/(lcos\theta_d) \tag{2-2}$$

where M^2 is the quality factor of beam, thanks to the single mode capability, it could be 1~2 depending on the current injection uniformity and fabrication defect. This FFP of the beam emitted from the scanner could be also proved by the Fresnel diffraction of near field pattern of the VCSEL scanner. The simulated FFP was shown in Fig. 2-5 by using MATLAB and assuming 1mm×5um aperture and deflection angle of 33°. By using Eq.

Fig. 2-4. Aperture size illustration

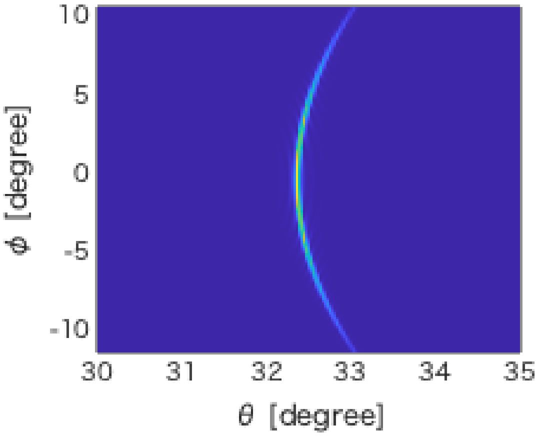

Fig. 2-5. Simulated FFP of beam scanner

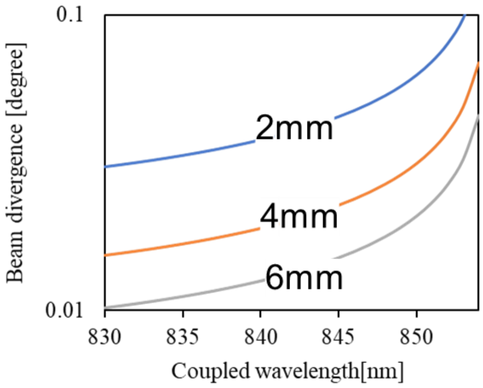

Fig. 2-6. Relation between beam divergence and coupled wavelength

2-2, the relation between wavelength and beam divergence could be plotted in Fig. 2-6 assuming M^2=1. It could be found that the beam divergence could be smaller than 0.1°in

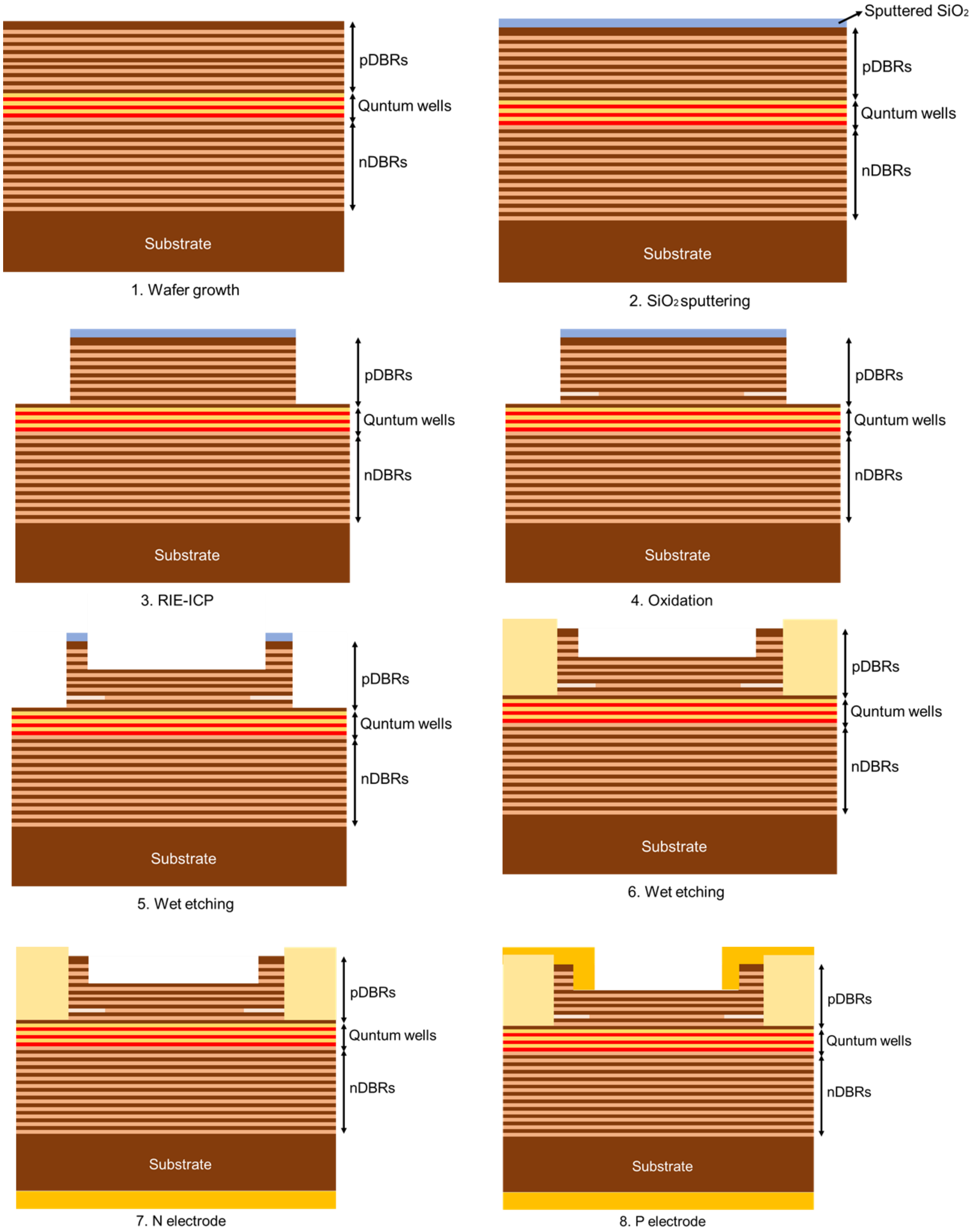

Fig. 2-7. Fabrication process of solitary VCSEL beam scanner

the whole observed wavelength and could be as small as 0.01° for 6mm-long devices. The waveguide is followed by a taper shape, which is used to attenuate the lateral reflection at the end

2.1.2 Fabrication process of solitary VCSEL beam scanner

The solitary beam scanner has almost same fabrication process with conventional VCSEL. It will go through wafer growth, wafer cutting for suitable processing sample size, reactive ion etching (RIE)-inductively coupled plasma (ICP) dry etching for mesa form, wet oxidation, polyimide passivation, wet etching for coupling region (different from conventional VCSEL, because conventional VCSEL does not need coupling region), n-electrode evaporation and p-electrode evaporation. In my study, the process after wafer growth will be finished. RIE-ICP was also finished by institute outside the university.

① Wafer growth finished by MOCVD, and the topmost layer of wafer should be doped larger to reduce the contact resistance. This layer was also called contact layer. The sample need to be cut from the original wafer. The original wafer may be 4-inch or 6-inch large, but our process machine only permits the sample of 2mm×2mm.

② SiO_2 sputtering: The surface of wafer is easy to be defected before finishing the process, so the SiO_2 need to be sputtered as a protection layer. The machine used here is as Fig. 2-8 shows:

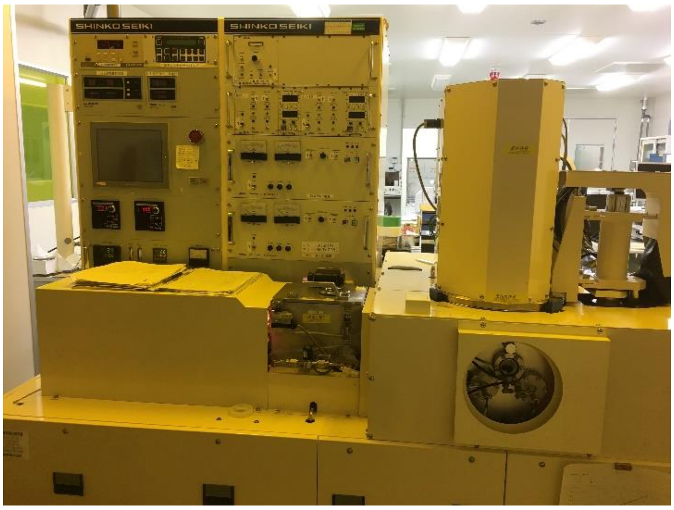

Fig. 2-8 Material sputtering machine

③ RIE-ICP: The ICP dry etching is used to form the mesa pattern of scanner as shown in Fig. 2-6. Only when the mesa pattern was formed, the aperture could be oxidized as our deign. To finish ICP dry etching, the resist patterning is needed to realize selective etching. The region that we do not want to etch should be protected by the resist. To realize this function, we need to firstly coat the resist AZ 5200NJ and OAP by spin coater on the whole sample, then using a mask to expose where we hope to develop and finally by using the AZ developer to remove the resist on the region that we hope to do ICP dry etching. The function of OAP is to stick the AZ5200NJ and SiO_2.The process was shown in Fig. 2-9. The coating and exposure condition are shown in table 2-1. After patterning, BHF is needed to remove the left SiO_2 in the region that we hope to etch. After finishing ICP dry etching, the resist should be removed by Acetone, 502A solution and oxygen plasma etching. Depending on the condition, it is possible to only using one of above-mentioned process to remove the resist.

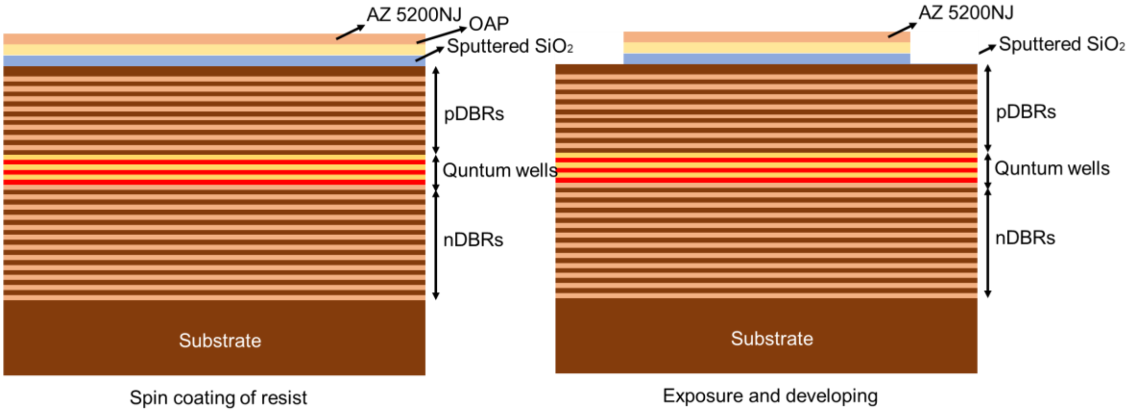

Fig. 2-9 Resist patterning process

Table 2-1. Spin coating and exposure condition for ICP patterning

Process	Condition
Spin coating	Speed: 4000rpm for 40s
Baking	Time: 90s
Exposure	Time: 6-8s
BHF etching	Time: 1min-2min

④ Oxidation: When the wafer was grown, an oxidation layer with higher Al composition was buried. By using the following chemical reaction, the oxidation could be implanted by flooding water carried by nitrogen at high temperature. In my study, the composition of Al is 98%. The oxidation temperature should be controlled properly. If temperature is too high, the oxidation will be very fast, and the mesa may be damaged when oxidation. If temperature is too low, the oxidation may not take place. In my study, the temperature was selected as 370°C. Before oxidation, the BHF is needed to remove the oxidation film of the sample due to natural oxidation to make oxidation uniform.

$$2AlAs + 3H_2O \rightarrow Al_2O_3 + 2AsH_3$$

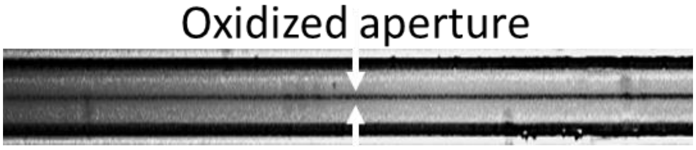

Fig. 2-10 Photo of oxidized aperture

⑤ Coupling region: Because the top reflectivity is so high, the external light is difficult to be coupled into the scanner. To increase the coupling efficiency, the coupling region should be formed by etching several layers to reduce the reflectivity. In my study, I choose to etch the mesa until 6-8 layers above QWs. The etching depth is usually around 2.2μm. This etching does not need critical etching uniformity and clear edging shape. Wet etching by acid is also promising. By making the solution as H_2SO_4:H_2O_2:H_2O=1:8:80, the etching speed of 2um/min could be obtained. Before selective etching, the resist patterning process as mentioned before is also needed. Also after etching, the resist should be removed, but the 502A and plasma etching is not needed anymore because the resist is not so hard as that after high-temperature ICP.

⑥ Polyimide passivation: The mesa is now exposed to the air. It is unsafe for the structure. Besides, the electrode should be evaporated on the mesa and extended out of mesa for probe touching. Passivation polyimide is required to support the electrode and protect the structure. The polyimide passivation method is similar to the resist patterning, but because the polyimide is passive resist the region that is exposed will NOT be developed. The process details are shown in Table 2-2. The spin coating speed here is much more important than that in previous resist patterning because the thickness of polyimide is very important and critical. If the thickness is too large or too small, the polyimide may be higher or lower than the mesa surface too much to support the electrodes.

Table 2-2. Spin coating and exposure condition for polyimide

Process	Condition
Spin coating	Speed: 3000-5000rpm for 40s
Baking	Time: 90s
Exposure	Time: 20-25s

⑦ The order n electrode and p electrode could be exchanged. Here the n electrode is evaporated firstly. The evaporation composition and thickness are shown in table 2-3. The AuGe could be used to form alloy with contact layer of wafer to decrease the resistance of the device after annealing. The annealing process could be together with annealing of p electrodes.

Table 2-3. Evaporation composition and thickness for n electrode

Metal	Condition
AuGe	100nm
Au	200nm

⑧ p electrode: To evaporate p electrode, the resist patterning is also needed because it is also selective evaporation. This time because the weight of metal is so large, and the evaporation temperature is high it is difficult to use previous resist. It will be very difficult to remove the resist after evaporating. To solve the problem, PMGI will replace the OAP. The PMGI could be easily removed by remover PG after evaporation. Thus, the electrode of undesired region will be lift off. The process details and evaporation composition were also shown in Table. 2-4.

Table 2-4. Evaporation composition and thickness for p electrode

	Metal	Thickness
1st time	Au	20nm
	Zn	60nm
	Au	200nm
1st time or	Ti	30nm
	Au	200nm

2nd time	Cr	30nm
	Au	200nm

Zn or Ti could be used to form alloy with contact layer of wafer to decrease the resistance of the device after annealing. The resistance is very important for high-power operation. In our experiment, we find Zn has better resistance than Ti, but the annealing temperature of Zn is higher than Ti. Sometimes higher annealing temperature may damage the mesa. It is noted there are two kinds of evaporation methods, and two kinds of metals could be used in p electrode evaporation. The first method is one-round evaporation, while the other method is two-round evaporation: only small-area was evaporated in the 1st round and the electrode will be extended by the 2nd round evaporation as shown in Fig. 2-11. The reason why two-round evaporation is needed is the smoothness of polyimide may not be enough for dense sticking of large-area electrode. In the experimental we found that if using one-round evaporation, the bubbles maybe observed on the electrode as Fig. 2-12 shows. The Cr has much better sticking to the polyimide, so it could be used for large-area electrode evaporation, but Cr could not be used to form alloy with contact layer of wafer, so 1st time evaporation is essential.

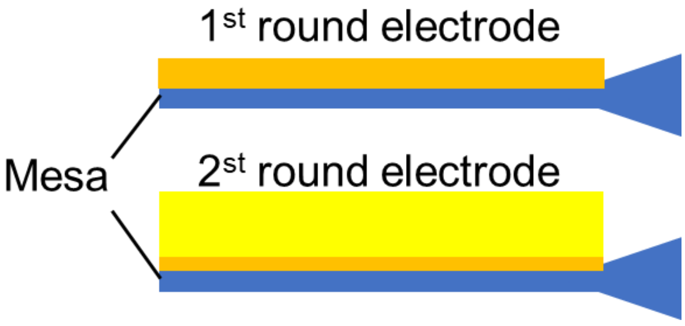

Fig. 2-11 Two-round electrode evaporation process

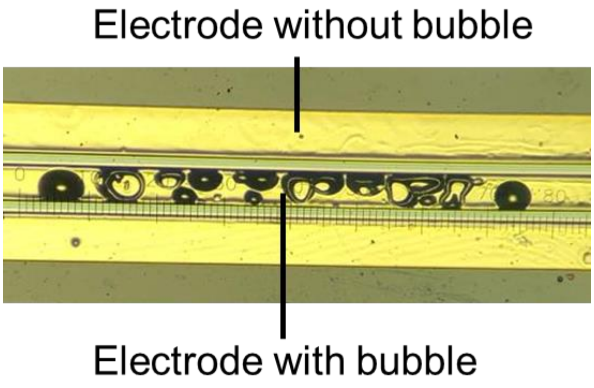

Fig. 2-12 Bubbles on the electrodes

2.1.3 Characteristics of solitary VCSEL beam scanner

The photo of final fabricated device is shown in Fig. 2-13. Its length is about 2mm. Of course, the varied-length beam scanner was also fabricated on the same chip including 3mm, 4mm and 6mm. The first assessment of the beam scanner is the electrical properties including the open voltage and resistance.

Fig. 2-13 The photo of fabricated solitary beam scanner

The electrical characteristics could be measured by VCSEL laser tester. The relation between injected current and voltage could be plotted as Fig. 2-14 shows. Its open voltage is smaller than 1.5V. Because the measurement step here is 1mA, the open voltage could be smaller by more precise measurement. However, for a 2-mm long devices, the open voltage of 1.5V is absolutely acceptable, while for the small devices for example 5um VCSEL it may be more critical. Another important parameter is the slope resistance, which could be evaluated by the slope of the plotted *I-V* line. Actually, the relation between *I* and *V* is not absolutely linear, we could find that the slope is getting smaller with *I* increasing. In average, the slope was measured as 1.7Ω, which enables high voltage for high current injection and high power.

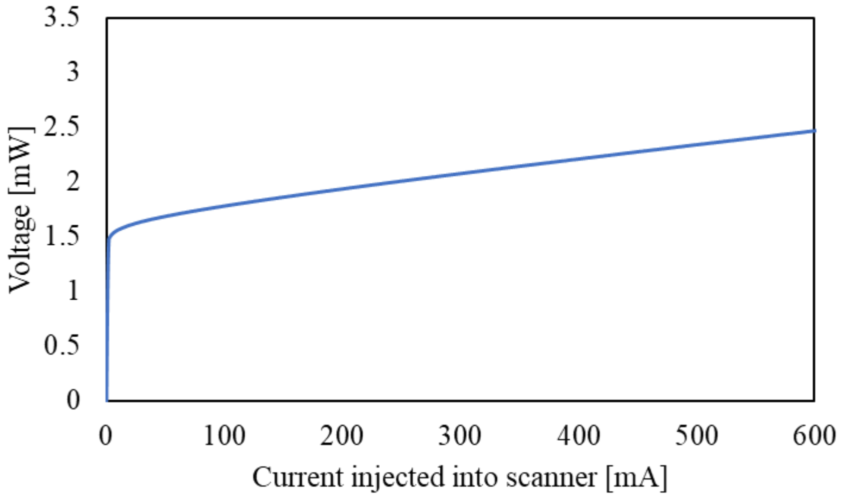

Fig. 2-14 Electrical characteristics of a 2mm-long VCSEL beam scanner

Then the optical performance of the beam scanner will be demonstrated. The important value is spectrum, near-field pattern (NFP), FFP and power under continuous wave (CW) and pulsed operation. Firstly, NFP and FFP will be given. The measurement setup schematic that was used to measure the NFP and FFP was shown in Fig. 2-15. The photo of real system was shown in Fig. 2-16 [4]. Considering the principle of our beam scanner, to realize beam steering, a lensed fiber is equipped to couple the light from the external tunable laser source and a electrical probe is used to inject current to realize the amplification.

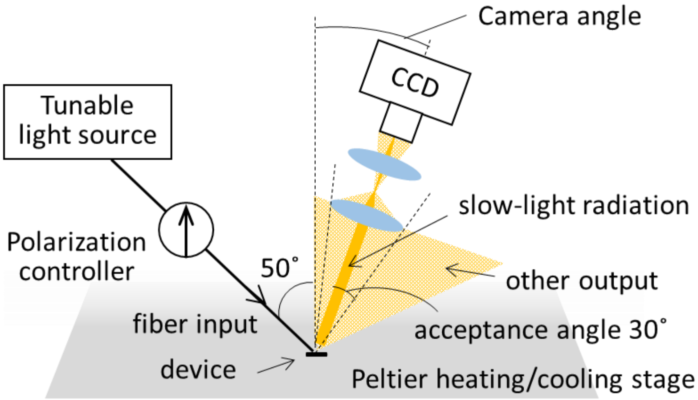

Fig. 2-15 The schematic of NFP and FFP measurement setup

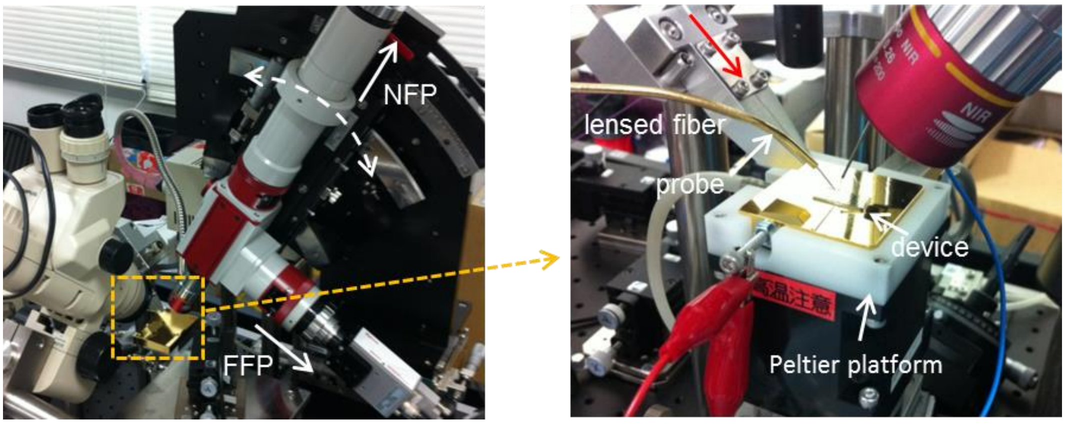

Fig. 2-16 The photo of NFP and FFP measurement setup

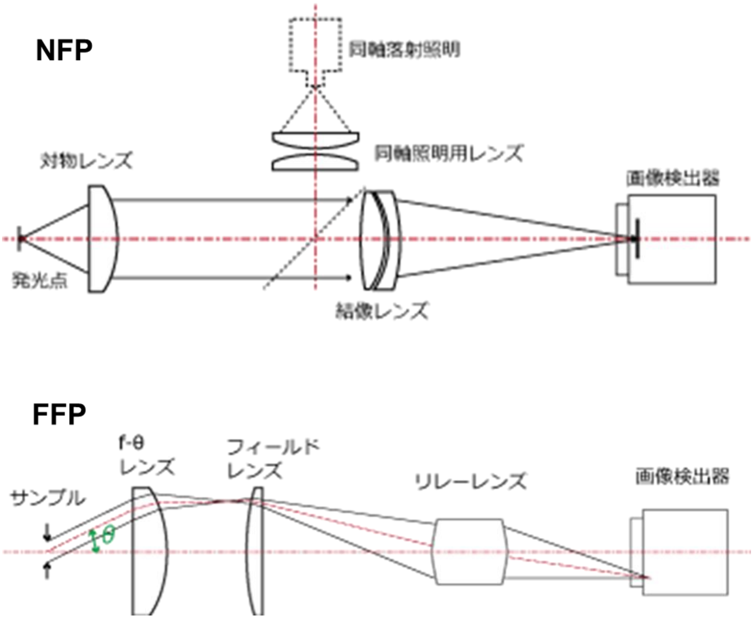

Fig. 2-17 The structure of NFP and FFP optics design (From Synos)

A rotatable CCD camera was used to capture the NFP through object and imaging lens directly and FFP through a $f-\theta$ lens based light analyzing optics. The details of the NFP and FFP structured was shown in Fig. 2-17 [5,6]. By using the system, the observed NFP of beam scanner when the coupled wavelength λ_{in} is 840nm and injected current $I_{scanner}$ is 160mA was shown in Fig. 2-18.

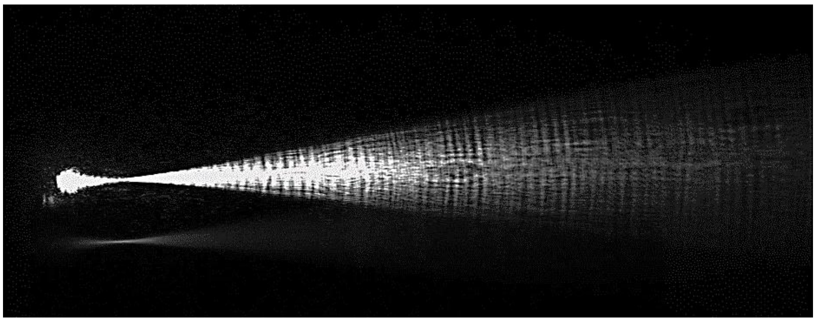

Fig. 2-18 The NFP of 2mm-long device

The slow light propagation could be found from the NFP. The former part seems to be stronger than the latter part is firstly due to the current injection uniformity and thus the ASE of former part will make it looks stronger especially being observed in the ASE emission angle. The colleagues also measured the result without ASE by a ASE cutoff structured shown in Fig. 2-19 [7].

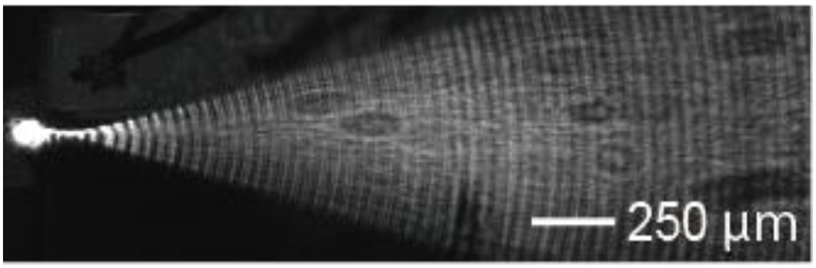

Fig. 2-19 The NFP of ASE cutoff structure based beam scanner

It could be found the uniformity becomes more uniform. The FFP will be observed then. The FFP was measured at a varied λ_{in} and fixed $I_{scanner}$=160mA. The beam image captured at different λ_{in} will be superimposed in the same figure. Through varying the

λ_{in} from 842.5nm to 850.5nm by 18 steps, the overlapped FFP was shown in Fig. 2-20. It could be found that the total scanning range of 18° ×14° ($\phi \times \theta$). In this thesis, θ refers to the horizontal direction and ϕ refers to the orthogonal direction in2D space. It indicates the beam scanning efficiency of 2.25°/nm in θ the FoV in ϕ could be enlarged by smaller aperture width d_1 due to the diffraction limit.

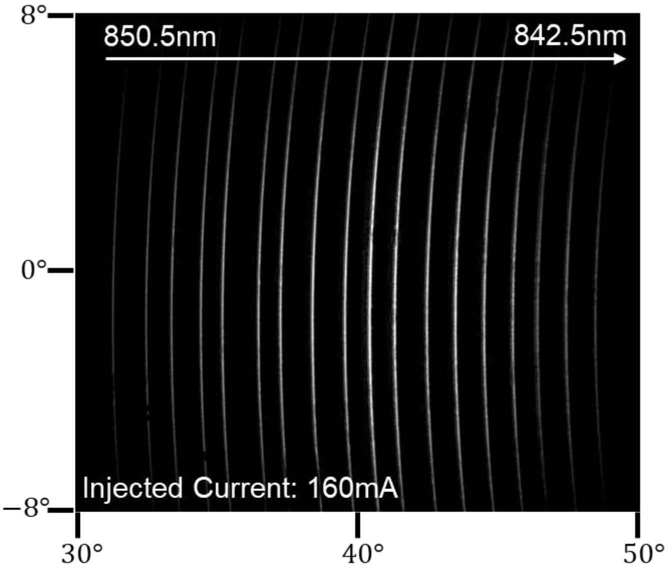

Fig 2-20 Overlapped FFP of 2mm-long VCSEL beam scanner

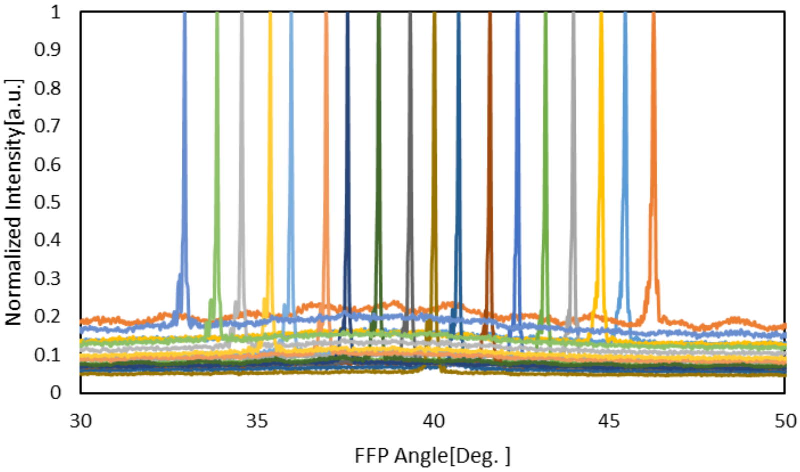

Fig. 2-21 Normalized beam profile of VCSEL beam scanner

The beam divergence is another important factor because it decides the total resolution number as FoV/beam divergence (FWHM, Full Width Half Maximum). The beam profile of the whole steering range is reported in Fig. 2-21. It shows good side-mode suppression with narrow beam divergence. The detailed beam divergence was shown in Fig. 2-22. The beam divergence is always smaller than 0.01 degrees in the whole detect range. The average beam divergence is around 0.07°, which indicates the resolution points number of about 257.

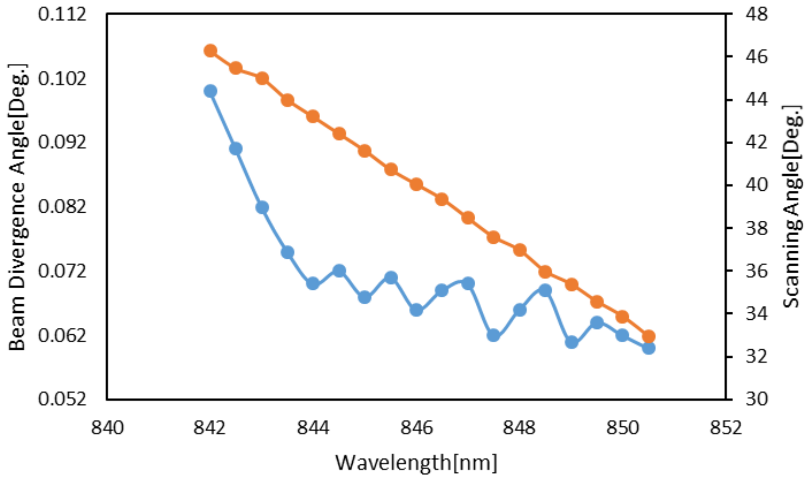

Fig. 2-22 Beam steering of a 2mm-long VCSEL beam scanner

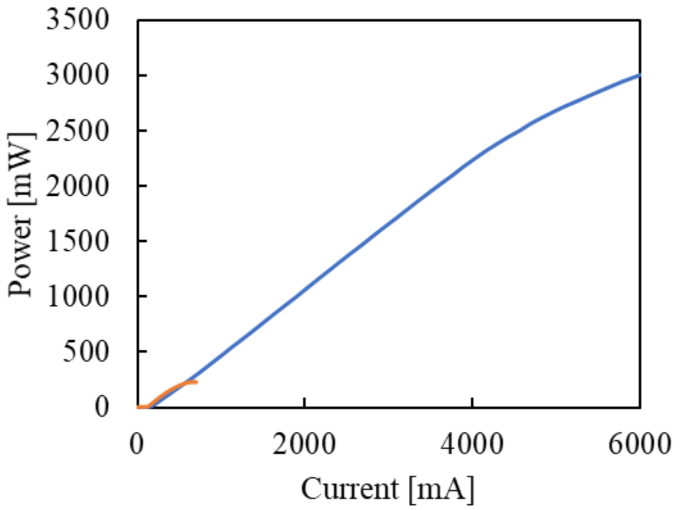

Fig. 2-23 Optical power of 2mm-long beam scanner (CW and Pulse)

Then the power of the device will be measured both under CW or pulse operation. Under CW operation, the power is easy to be saturated due to the heating effect. For the pulse operation the heating effect could be smaller, so the saturation current will be larger, which enables larger power. The result was shown in Fig. 23, where the orange line indicates the CW power, which is saturated very quickly at around 400mA. However for the pulse operation (pulse width is 100ns, blue line in the figure), the power could reach around 3W when the current is increasing to 6A.

As shown in Fig 1-14, the power and beam divergence is highly related to the scanner length. To enlarge the maximum power and reducing the beam divergence 6mm-long beam scanner was also fabricated. The electrical properties for such long beam scanner is not only determined by the resistance of scanner itself but also the contact resistance of current probe is also important, so in the *I-V* curve. The significant reduction of resistance could not be found. Its optical properties was measured as following. Firstly, the FFP measurement was implanted as shown in Fig. 2-24.

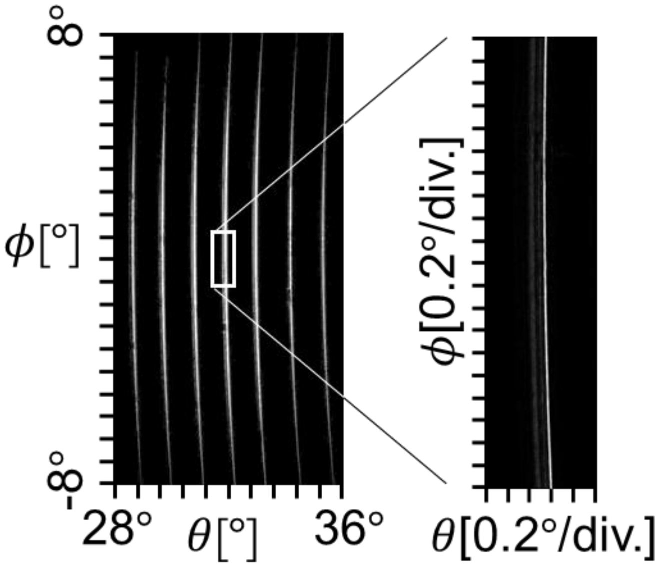

Fig. 2-24 Overlapped FFP of 6mm-long solitary beam scanner

The measurement was finished when the λ_{in} is varied from 841nm to 844.5nm and $I_{scanner}$ = 400mA. The beam is steered to around 7°, which is smaller than the 2mm-long beam scanner because of smaller amplification spectrum width of longer devices. The beam divergence is difficult to be directly witnessed by the current setup due to the limited capturing aperture of FFP setup and limited resolution. The high-resolution mode of FFP measurement may be helpful to confirm the beam divergence, the FFP observed under high-resolution mode was shown in the zoomed figure in Fig. 2-24. It could be found that significant improvement of beam divergence was obtained. The beam divergence could less than 0.03° which is smaller than half of that of 2mm-long devices. The correspondence of wavelength with deflection angle and beam divergence could be found in Fig. 2-25. It also shows stable beam divergence at the whole beam steering range. The average beam divergence is about 0.023°, which indicates the resolution of 308. We could see that the resolution is increased by extending the scanner length even if the total beam steering range was smaller thanks to the smaller beam divergence.

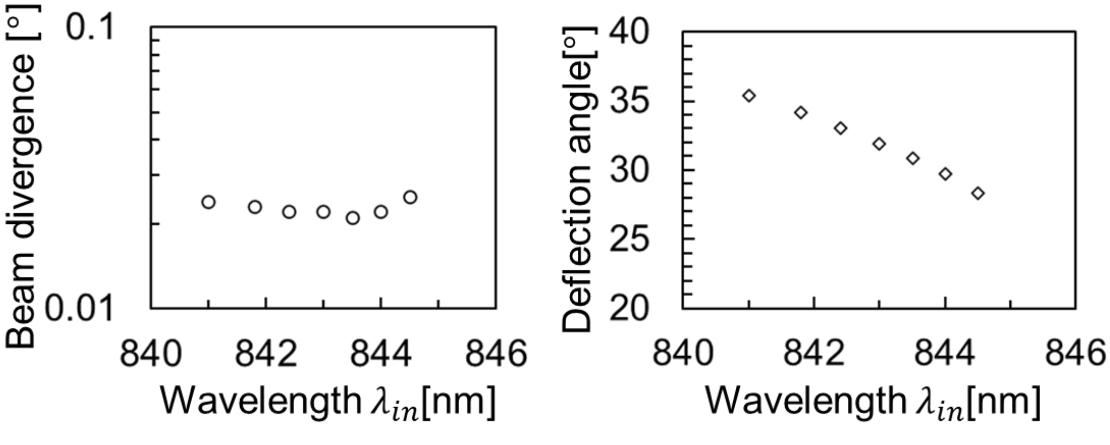

Fig. 2-25 Correspondence of wavelength with deflection angle and beam divergence

The power of 6mm-long device was also measured. It is expected to obtain larger power thanks to the capacity for larger injection current. The measurement result under CW and pulse operation is shows in Fig. 2-26. It could be seen that the power could increased to more than 8W by extening the scanner length. Considering the optical power efficiency of around 40%, the electrical driver power consumption may be 20W to realize the output optical power of 8W.

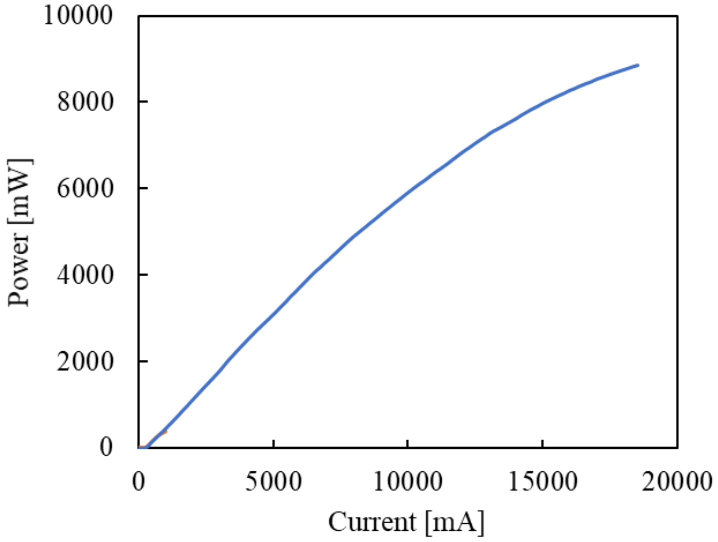

Fig. 2-26 Optical power of 6mm-long beam scanner (CW and Pulse)

2.2 The solitary beam scanner integrated to conventional VCSEL

2.2.1 Principle of integration of integration to a conventional VCSEL

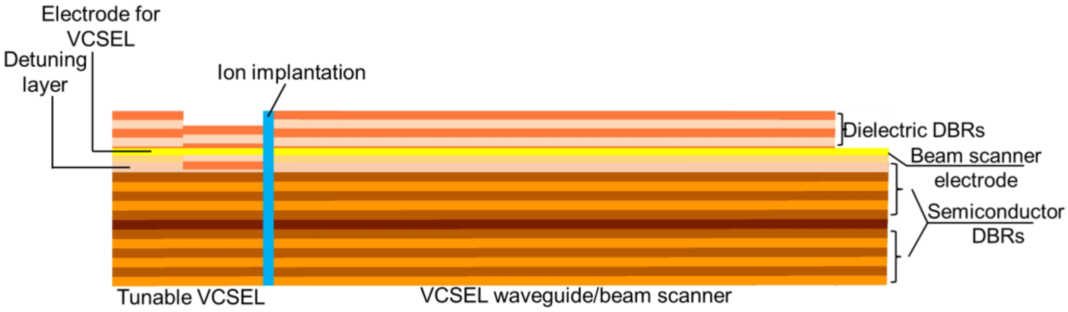

Fig 2-27 Schematic of integration of solitary VCSEL beam scanner and VCSEL

The requirement of external light source for solitary beam scanner is very critical for its manufacturing and small size. The on-chip integration of seed laser and beam scanner has very significant meaning for practical use and reflects on the irreplaceable merit of proposed VCSEL thanks to the purely and mature solid-stated fabrication, whici indicates much lower cost and much compact size

Because the VCSEL beam scanner has the same wafer structured with VCSEL, the VCSEL could be easily formed at the beginning of VCSEL beams scanner as a seed laser and be isolated by ion implantation. Thanks to the electro-thermal effect of VCSEL, by tuning the current injected into the VCSEL the wavelength will be red shifted. In this case, the seed VCSEL could replace the external light source in the previous section 2.2. However, as explained in 2.1.1, the wavelength should be smaller than the resonant wavelength of beam scanner. If VCSEL is directly formed at the beginning of scanner, the seed VCSEL will have the same lasing wavelength with resonant wavelength λ_r. When injecting the current to the seed VCSEL I_{VCSEL}, the red shift of lasing wavelength will preclude its coupling and propagation in the VCSEL beam scanner. In this case, the wavelength detuning structure was proposed [8] as shown in Fig. 2-27. To realize the wavelength detuning, it is needed to make shallow etching as around 3-5 layers above the active region. It is to say the half-VCSEL (Only 3-5 pairs of top DBRs) wafer should be used. After wet etching for detuning the dielectric DBRs will be deposited to obtain enough reflectivity. The detailed designing method and etching depth could be analyzed by the Optical transfer matrix method [9] . The relation of etching depth and detuning wavelength was calculated by our colleagues before [10] as shown in Fig. 2-28. By using the Fimmwave, the coupling efficiency of VCSEL to scanner could be also calculated as shown in Fig. 2-29. From these two figures, the following conclusion could be obtained. By etching 0-80nm at 5 pairs above the active region, the wavelength detuning of VCSEL could be 0-20nm. However, etching 100nm may reduce the reflectivity that may make the VCSEL fail to lase. Therefore we choose 50 nm as the target etching depth, it could provide the top reflectivity of around 99% and wavelength detuning of around 10nm. From the coupling efficiency figure, it could be known that the coupling efficiency of larger than 70% at targeted etching depth. Assuming the power of VSCEL is 3mW, the coupled power from VCSEL to scanner may be larger than 1mW, depending on the previous calculation, the power of beam scanner could reach watt class.

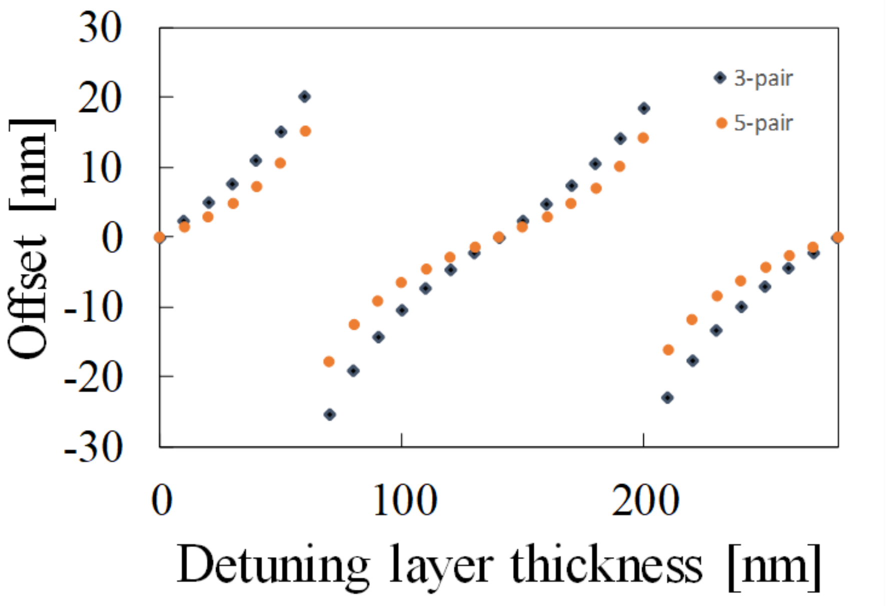

Fig. 2-28 The relationship between wavelength detuning and etching depth [10]

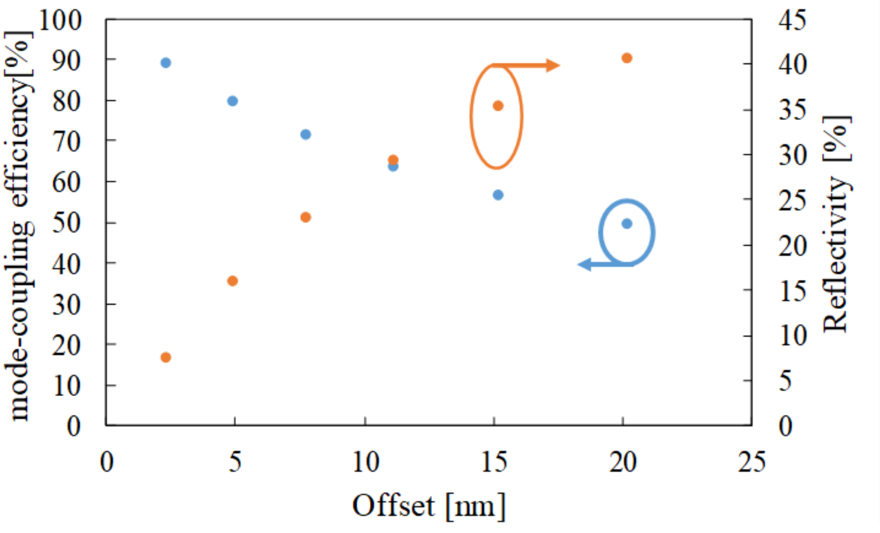

Fig. 2-28 The relationship between wavelength detuning and couple efficiency [10]

2.2.2 Fabrication process of VCSEL beam scanner integrated to the seed VCSEL

Although the half VCSSEL was used here, the fabrication process is almost same as shown in section 2.1.2. In this section, only the process that is different from 2.1.2 will be shown. The first different step is the ion implantation before ICP to make VCSEL and beam scanner isolated. The resist patterning is also needed for ion implantation, the region that will be ion implanted will be opened by resist developing. The developing method is same as ICP and resist removement process is also similar to that of ICP. The ion implanted sample will be shown in Fig. 2-29. In the figure the ICP and oxidation was already finished, too.

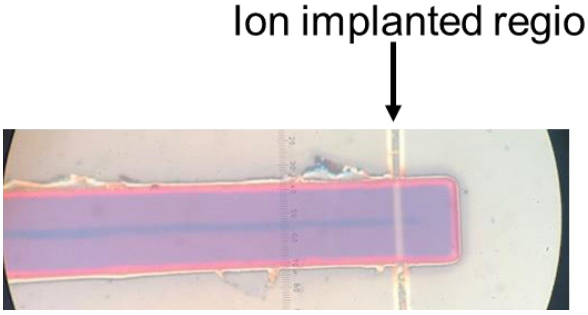

Fig. 2-29 Ion implanted device photo

Another difference is that because the seed VCSEL is integrated, the wet etching process for coupling region is not required anymore. However, after electrode evaporation, the wet etching is needed for wavelength detuning as mentioned in the last section. This etching is very shallow, the solution will be also thinner that was used in the wet etching for coupling region. Later, the dielectric DBRs will be deposited on the mesa. What we chose here as dielectric DBRs are SiO_2 and Ta_2O_5. Their high refractive difference makes it easier to get enough reflectivity, so only 7.5 pairs are needed. The photo of final device is shown in Fig. 2-30.

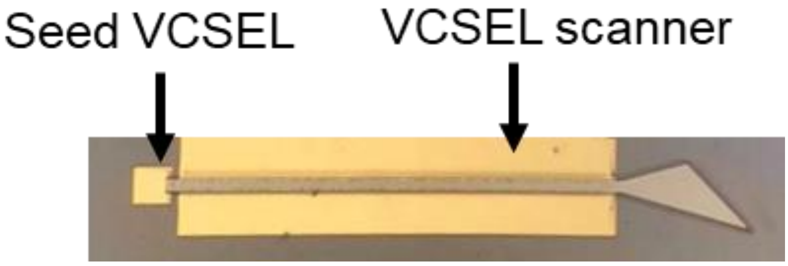

Fig. 2-30 The photo of fabricated devices

2.2.3 Characteristics of beam scanner integrated to the seed VCSEL

The characteristics of seed VCSEL should be discussed firstly. The electrical resistance, optical power will be demonstrated in Fig. 2-31. The resistance is around 230Ω from the slope of *I-V* curve in Fig. 2-31 and the optical power could be as large as 3mW as expected. It means high slope-efficiency of 0.82W/A, which will reduce the power consumption of driving the seed VCSEL. The slope resistance is a little high due to the defect when making the wet etching and small aperture size (as small as 3um).

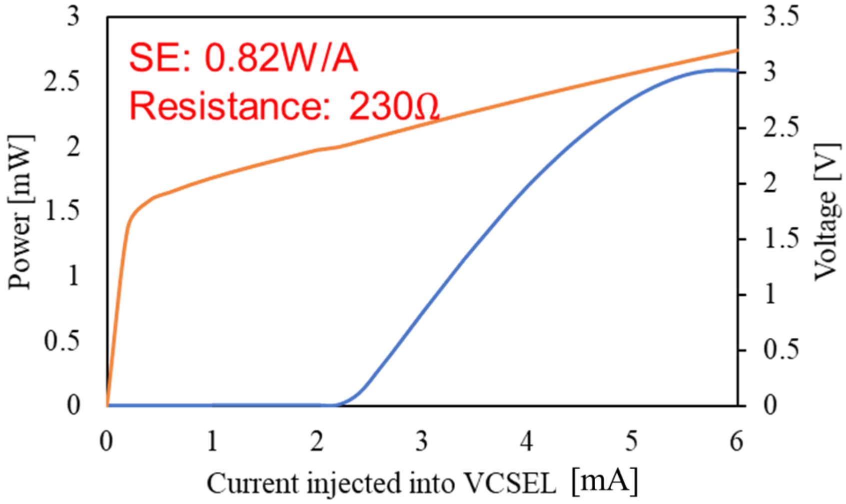

Fig. 2-31 The power and electrical properties of seed VCSEL

The spectrum should be compared to the spectrum of beam scanner, because the detuning should be checked to enable the mode coupling. The Spectrum of both were overlapped shown in Fig. 2-32 when the I_{VCSEL} =5mA and $I_{scanner} = 160mA$. It could be found that the wavelength for seed VCSEL and scanner are 862nm and 867.4nm, the wavelength detuning is about 5.4nm. When the I_{VCSEL} is smaller at the threshold of 2mA, the detuning should be larger due to the blue shift of seed VCSEL. When the detuning is larger, larger beam steering range could be expected.

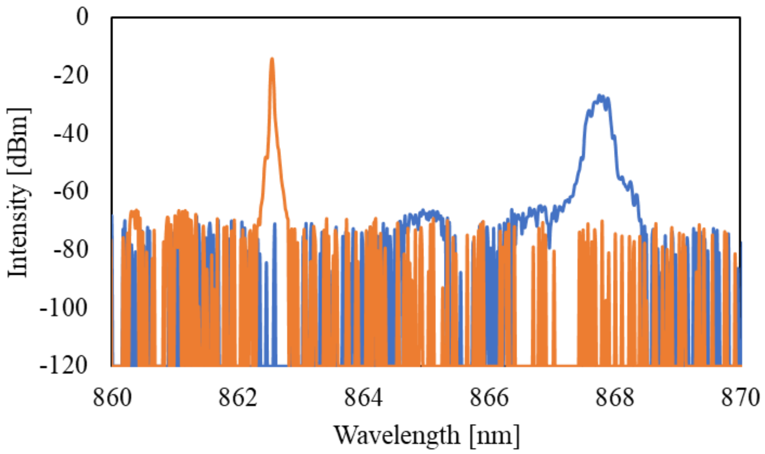

Fig. 2-32 The spectrum of seed VCSEL and scanner

The FFP will be shown in Fig. 2-33 by tuning the I_{VCSEL} from 2mA-5.7mA. The overlapped FFP will be shown. It is found that more than 12° could be steered in this wavelength tuning range. The tuning efficiency is about 3.2°/nm, which is larger than that in the previous section. It could be explained by the closer operation wavelength to resonant wavelength of beam scanner as witnessed in the Fig. 2-3. Its average beam divergence is around 0.12°, which is larger than previous result because the scanner length is only 1mm. It also indicates the resolution of about 100.

Fig. 2-33 Overlapped FFP of 1mm-long beam scanner integrated to seed VCSEL

The power characteristics of beam scanner was shown in Fig. 2-34, it could reach power of more than 50mW, but actually when the current is high, the fluctuation could be observed from the curve. It means the mode instability happens, so the stable power of the proposed beam scanner is around 10mW, which may be limited by the coupled power from seed VCSEL.

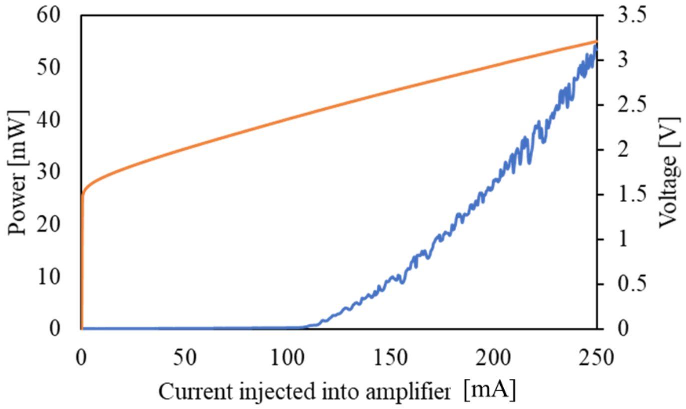

Fig. 2-34 The power and electrical properties of seed VCSEL

The beam scanning speed is also measured as shown in Fig. 2-35. Thanks to the good modulation characteristics of VCSEL, the 3dB cutoff scanning frequency could be larger than 100kHz.

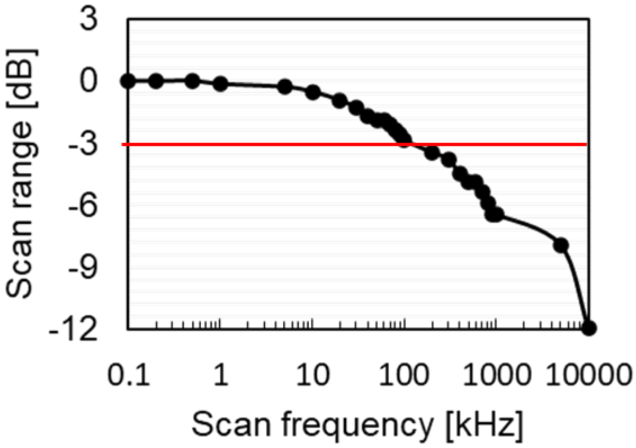

Fig. 2-35 Beam scanning response with different scanning frequency

2.3 The solitary beam scanner integrated to slow-light VCSEL

2.3.1 Principle of solitary beam scanner integrated to slow-light VCSEL

As mentioned in the last section, the coupled power of seed VCSEL is too small to obtain high power of beam scanner stably. The improvement of increasing the power of seed VCSEL is very important to make the beam scanner available to be used in long-range 3D sensing. Fortunately, the slow-light lasing was found in a long-length VCSEL [11]. Previously, limited by the cavity size of conventional VCSEL, the conventional vertical-mode power over 3mW is difficult. When the cavity length is getting larger, the single mode quality will be much poorer. The finding of slow-light lasing provides the possibility of lateral mode control of a longer-length VCSEL, which may greatly increase the power of VCSEL. This kind of VCSEL using slow-light mode is called slow-light VCSEL. If the slow-light VCSEL could be used as the seed laser of beam scanner, the coupled power and then the output power of scanner could be greatly enhanced.

Slow-light lasing of VCSEL originates from the slow light propagating in the VCSEL cavity. As found, not only when the light was coupled to the scanner but also the excited light in the cavity without external coupling, should the slow light propagate in the cavity. That is to say, conventional vertical-mode light and slow light both exist in the VCSEL cavity. There must be the gain competition between them. As discussed before, the wavelength of slow light should be smaller than the vertical light, so if the gain was blue shifted from the vertical light wavelength (resonance wavelength), the slow light mode will get merit. Besides, the slow light always has higher reflectivity at the top DBRs, so through reducing the top reflectivity, it is possible to make only slow-light mode lasing and suppress the vertical-light lasing due to larger loss. Based on the principle, the epi wafer used for slow-light VCSEL should has following points: PL wavelength blue shift from resonant wavelength about 25nm and the number of top DBR pairs is reduced by 1 pairs compared to the conventional VCSEL. It is noted because wavelength of slow-light lasing mode is naturally smaller than the resonance wavelength. The wavelength detuning used for section 2.2 is not needed anymore, so full-VCSEL wafer is proper for fabricating VCSEL beam scanner integrated to seed slow-light VCSEL.

Even the above-mentioned method was adopted to suppress the vertical lasing, the single mode of slow-light lasing is still difficult. However, the lateral propagation of slow-light mode makes it possible to make mode selection by using grating like that used in distributed feedback (DFB) lasers as shown in Fig. 2-36. The grating was etched at the surface of long-length VCSEL. The taper shape is added at the end to increase the asymmetricity of the laser to realize unidirectional emission angle.

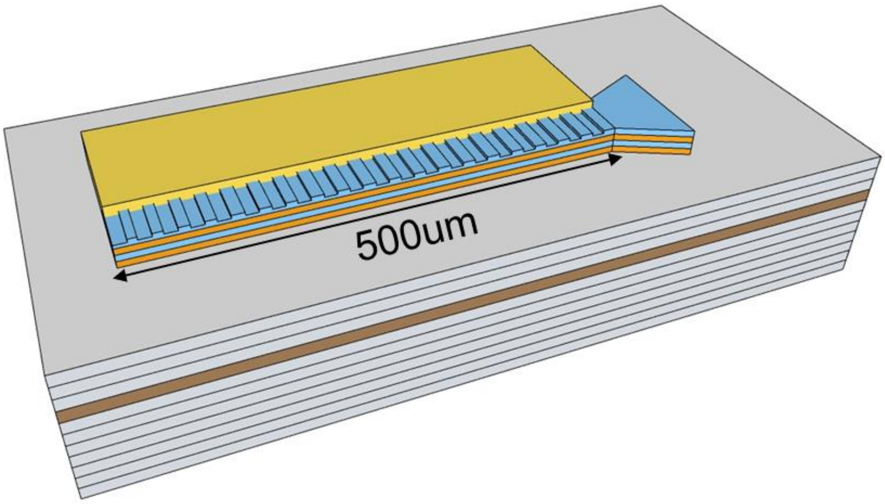

Fig. 2-36 The Schematic of slow-light VCSEL

However, the grating design should be a little different from DFB lasers, because the effective index of slow-light mode is smaller than that of lasing mode in DFB lasers. The effective index of etched and no etching region for slow-light mode could be simulated in Fimmwave as shown in Fig. 2-37 when the resonant wavelength is 855nm, where orange line is high index and blue line is low index. Taking designed wavelength of 830nm as an example, the high index is 0.794 and low index is about 0.790. The refractive index of SCH layer was reduced to cutoff the guided wave. Because the grating pitch of slow-light VCSEL (>500nm) is larger than that in DFB lasers by more than 3 times, the conventional lasing mode in DFB lasers cannot be lased in surface-grating slow-light VCSEL.

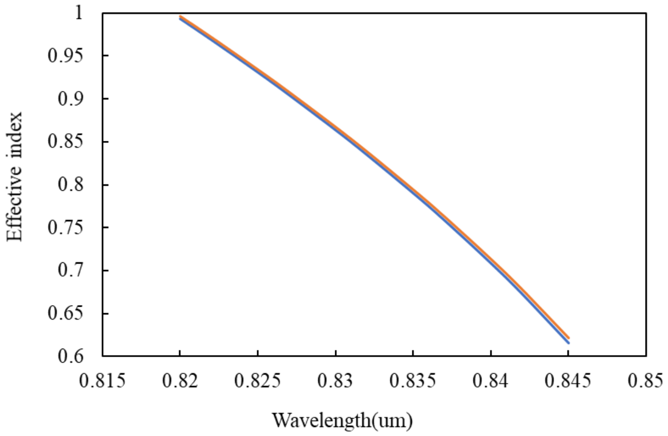

Fig. 2-37 The simulated effective index of high and low region

The grating pitch Λ could be calculated by the Eq. 2-3, where λ_{VCSEL} is the designed lasing wavelength for the slow-light VCSEL and N_{eff} is the average effective index of the grating. Considering the design wavelength of 830nm, the grating pitch is about 523nm including 261nm etching region and 261nm no-etching region.

$$\Lambda = \lambda_{VCSEL}/(2N_{eff}) \tag{2-3}$$

Knowing the principle of slow light VCSEL, the integration of slow-light VCSEL and VCSEL beam scanner could be proposed as shown in Fig. 2-38. The beginning part of VCSEL beam scanner could be regarded as a slow-light seed VCSEL by loading the surface grating. The electrode should be separated for independent control, but the ion implantation is not required anymore, because when the length of seed VCSEL is increased to about 1/4 of beam scanner, the current leakage is not strong as the condition when a conventional VCSEL is integrated. Similarly, thanks to the electro-thermal effect of seed VCSEL, by tuning the current injected into the seed VCSEL I_{VCSEL}, the beam scanning could be achieved.

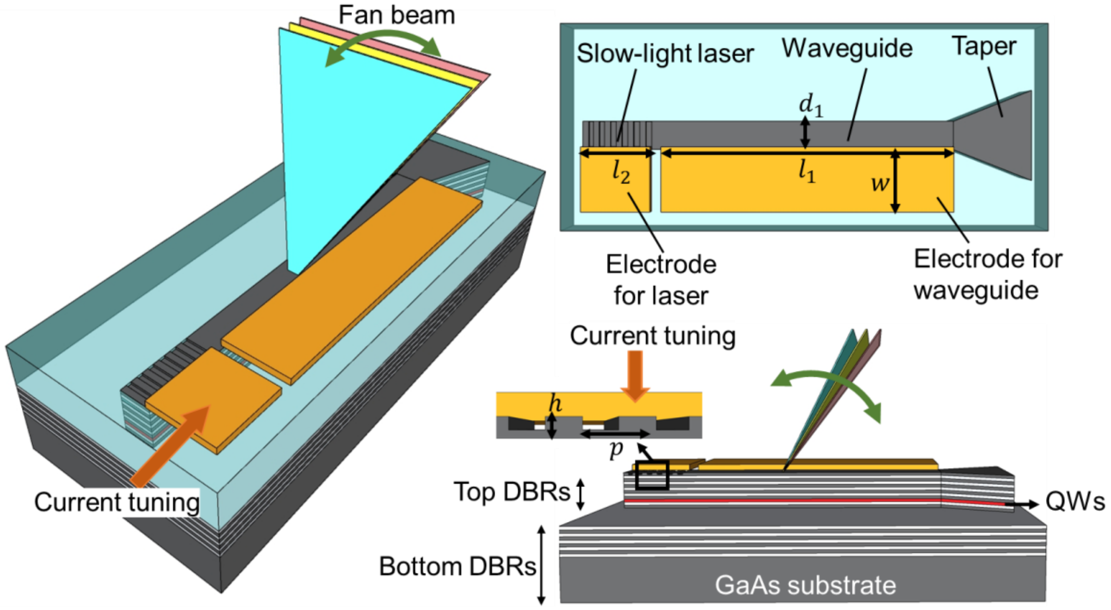

Fig. 2-38 The Schematic of slow-light seed VCSEL integrated VCSEL beam scanner

2.3.2 Fabrication of solitary beam scanner integrated to slow-light VCSEL

In this section, the fabrication difference between the scanner and previous solitary scanner will be introduced. Because they are both fabricated on the full wafer, the fabrication process is almost same. Of course, the first difference is no requirement of wet etching for coupling region thanks to the integration to the seed VCSEL. Another important difference is the requirement of grating patterning and etching. The process of forming a grating is also selective etching. The first problems is patterning method of laser lithography and electron beam lithography (EBL). Laser lithography is a very fast and cheap lithography method with 1μm pricison (using UV laser), while EBL is a relatively slow and expensive lithography with 10nm precision. For the 520nm pitch grating forming, the EBL seems to be a better choice, while laser lithography could be used for higher order grating patterning. After EBL patterning, the selective etching should be done. ICP dry etching and wet etching are both available. Considering the controllability and etching stability of ICP, the ICP is recommended. In this study, 30nm etching depth was found the optimized etching depth for forming the grating. The photo of grating after selective etching is shown in Fig. 2-39.

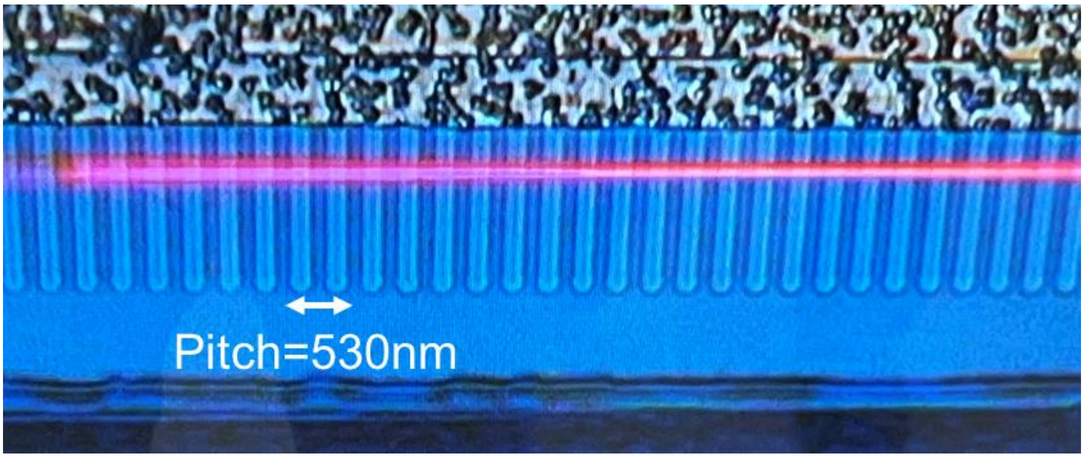

Fig. 2-39 The photo of grating after selective etching

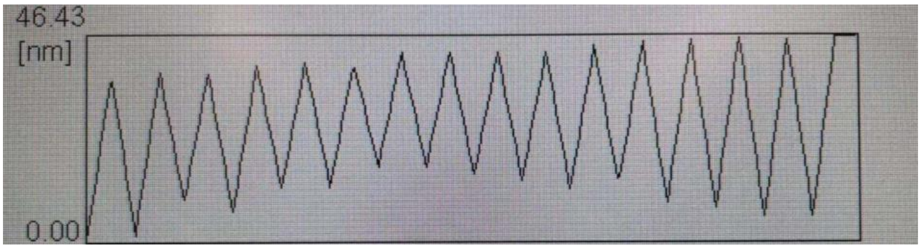

Fig. 2-40 The etching depth measurement by using atom force microscopy

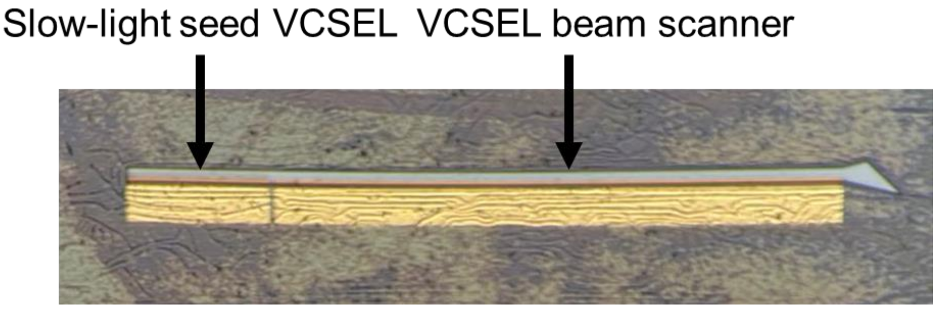

Fig. 2-41 Photo of fabricated beam scanner integrated to a seed VCSEL

The etching depth was confirmed by the atom force microscopy (AFM) as shown in Fig. 2-40. It could be also confirmed by Scanning electronics microscopy. The photo of finally fabricated beam scanner is shown in Fig. 2-41. The length of slow-light seed laser and beam scanner is 0.5mm and 2mm respectively.

2.3.3 Characteristics of solitary beam scanner integrated to slow-light VCSEL

The characteristic of slow-light laser will be firstly demonstrated. When injecting current of about I_{VCSEL}=150mA, the FFP was shown in the left figure in Fig. 2-42, it should be single mode. By Eq. 2-3, the pitch size determines the slow-light lasing wavelength of beam scanner, so by varying the pitch size, we could obtain varied slow-light lasing wavelength for different devices. The left figure shows the FFP when the pitch size was designed as 530nm, while the right figure shows FFP of 600nm. Depending on the Eq. 2-1. If the lasing wavelength is changed, the emission angle will also be changed if resonance wavelength of the wafer is same. It could be witnessed in Fig. 2-42. The left figure corresponds to the lasing wavelength of around 835nm and the right figure indicates the lasing wavelength of around 840nm

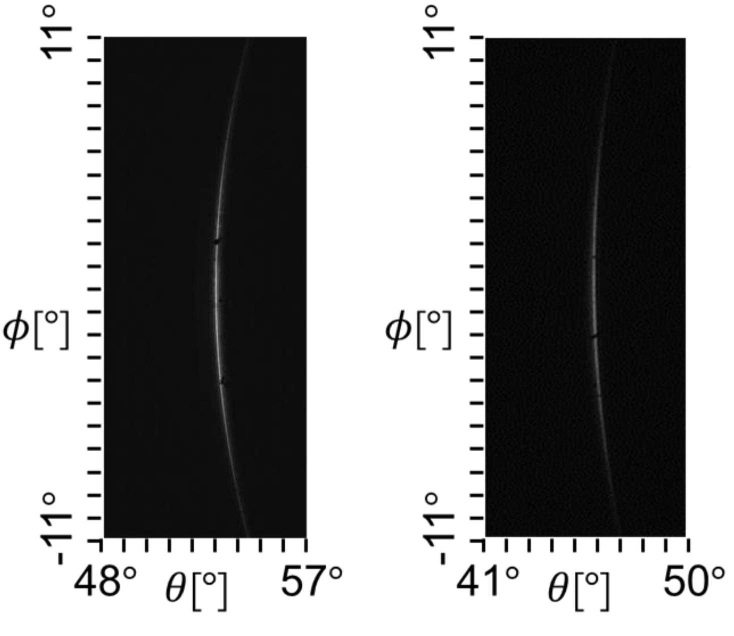

Fig. 2-42 FFP of slow-light seed laser with pitch of 530nm and 600nm

When varying the current I_{VCSEL}, the lasing wavelength of slow-light seed laser will be tuned thanks to the electro-thermal effect which varying the refractive index of DBRs. When the I_{VCSEL} varying from 50mA to 350mA, the lasing wavelength could be observed through the spectrum shown in Fig. 2-43. The stable single mode lasing could be obtained in the whole tuning range. And the tuning range of >5.8nm could be obtained, which may lead to beam steering range of larger than 7° that will be discussed later. Besides, the power of slow-light seed laser should be also measured. The power-current curve is shown in Fig. 2-44. It could be found that the power is much larger than that of conventional VCSEL, the slope efficiency is not as large as conventional VCSEL shown previously because the slow-light laser has left and right emission due to the symmetricity of the slow-light laser. Although the symmetricity is avoided to some extent by the asymmetrical device layout but difficult to be absolutely avoided without being followed by a taper shape.

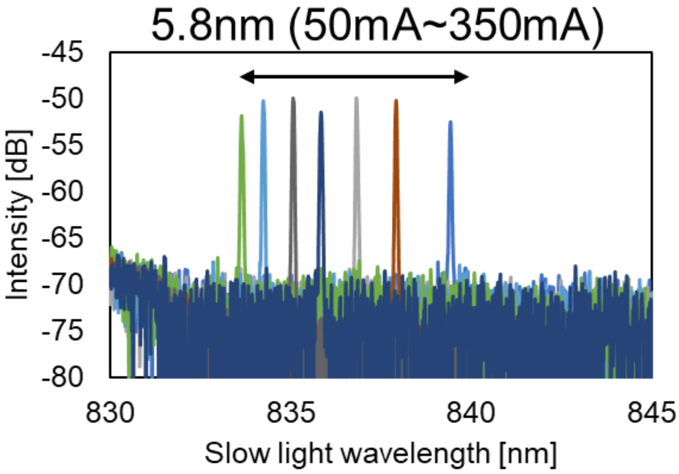

Fig. 2-43 Spectrum when the I_{VCSEL} varying

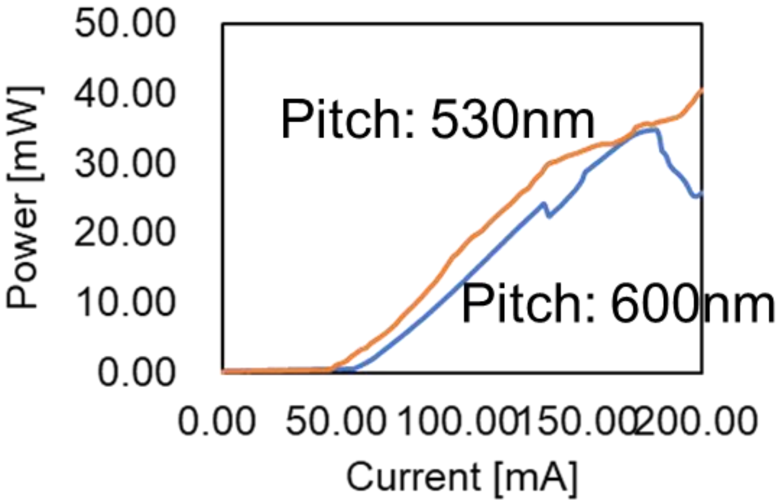

Fig. 2-44 Power of slow-light seed laser

The light from slow-light seed VCSEL was coupled into the beam scanner. With injecting current to the beam scanner, the light will be amplified. With wavelength tuning of slow-light seed VCSEL, the output beam could be also steered. The beam steering performance of beam scanner will be demonstrated. Firstly, the FFP when the I_{VCSEL} tuning from 40mA to 267mA and injecting $I_{scanner}$ of 200mA. The overlapped FFP of emitted beam is shown in Fig. 2-45. The beam steering range of >7° was obtained, which could be further extended by injecting more current to seed VCSEL, but the intensity degradation maybe larger. From the zoomed figure, it could be also found that the beam divergence could be controlled smaller than 0.08°

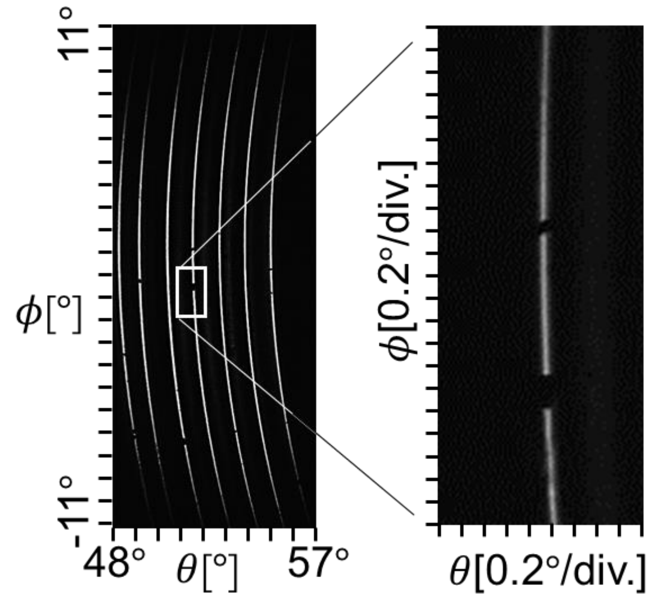

Fig. 2-45 Overlapped FFP of 2mm-long beam scanner integrated to seed VCSEL

The beam divergence in the whole beam steering range was also measured as shown in Fig. 2-46. It could be found that in the whole beam steering range, the beam divergence is very stable at 0.07°, which indicates the total resolution number of nearly 100, which could be further increased by extending the scanner length.

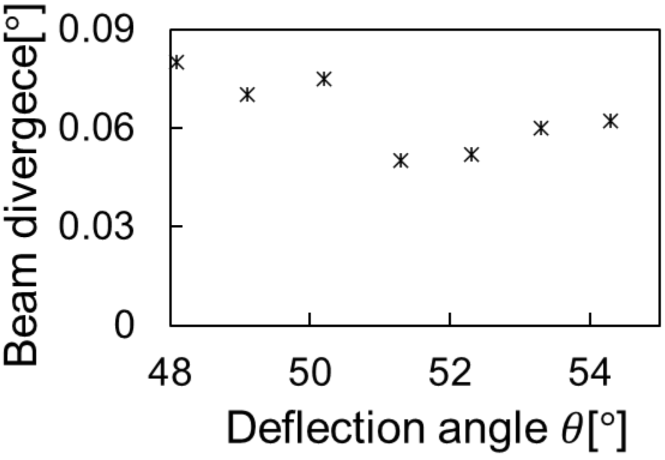

Fig. 2-46 Beam divergence of 2mm-long beam scanner integrated to seed VCSEL

The power characteristics of the beam scanner is another important factor that effects the practical availability of the beam scanner in long-distance detection. It was shown in Fig. 2-47. With injecting pulsed current of 4A, the power could reach 2W and could be further improved by extending the scanner length.

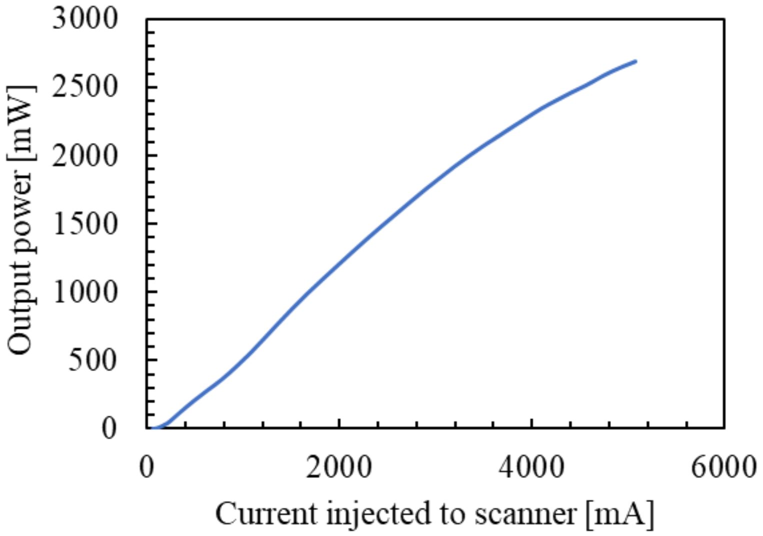

Fig. 2-47 Power of beam scanner

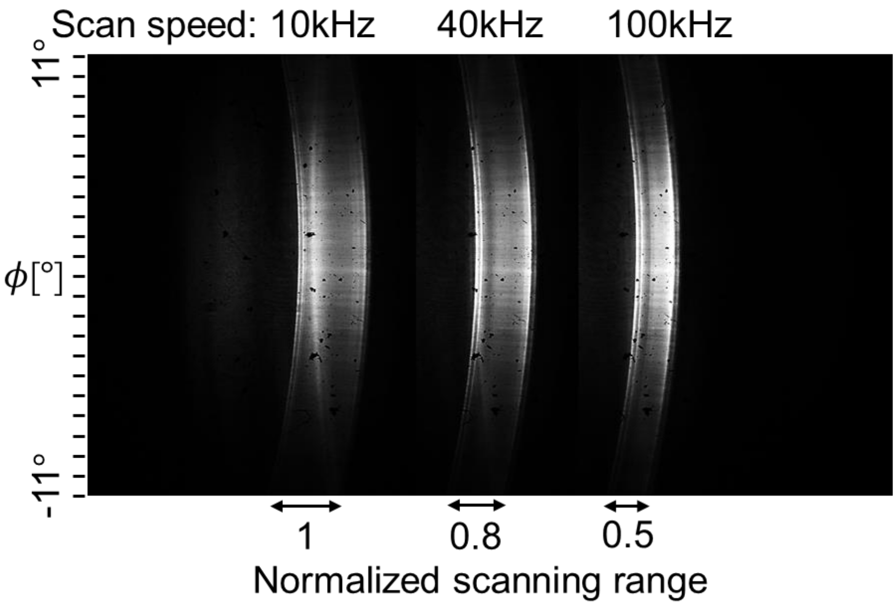

Fig. 2-47 Scanning range with different scanning frequency

The beam scanning speed was also measured considering the length extension. The sine-wave voltage with different frequency was added to the seed VCSEL, through observing the beam scanning range. Its maximum scanning speed could be obtained. The scanning range when sinewave frequency of 10kHz, 40kHz and 100kHz were measured as shown in Fig. 2-48. It could be found that the 3dB scanning range cutoff speed could be larger than 100kHz, which is compatible with most 3D sensing applications.

Reference in Chapter 2

2-1. P. F. Mcmanamon, S. Member, T. A. Dorschner, D. L. Corkum, L. J. Friedman, D. S. Hobbs, M. Holz, S. Liberman, H. U. Y. Q. Nguyen, D. P. Resler, R. C. Sharp, and E. A. Watson, "Array Technology," **84**(2), (1996).

2-2. F. Xiao, W. Hu, and A. Xu, "if," **44**(26), 5429–5433 (2005).

2-3. X. Gu, T. Shimada, and F. Koyama, "Giant and high-resolution beam steering using slow-light waveguide amplifier," Opt. Express **19**(23), 22675 (2011).

2-4. D. Dissertation, "Slow-light Bragg Reflector Waveguide-based Functional Devices for Use in Next-generation Optical Networks 顧 暁冬," (September), (2014).

2-5. "SYNOS WEB / シナジーオプトシステムズ株式会社 WEB SITE 製品の概要 FFP 計測光学系 M-Scope type F FFP 計測光学系の方式," 11–13 (2021).

2-6. M. Apo, "SYNOS WEB / シナジーオプトシステムズ株式会社 WEB SITE 製品の概要 高機能 NFP 計測光学系 M-Scope type S 高機能 NFP 計測光学系の方式," 11–13 (2021).

2-7. 博士論文: 高出力 VCSEL ビームスキャナに関する研究 (Study on high-power VCSEL-based beam scanners), 許在旭, (2020).

2-8. S. Hu, X. Gu, M. Nakahama, and F. Koyama, "Non-mechanical beam scanner based on VCSEL integrated amplifier with resonant wavelength detuning design," Chin. Opt. Lett. **19**(12), 121403 (2021).

2-9. L. Y. Bahar, "Transfer matrix approach to layered systems," J. Eng. Mech. Div. **98**(5), 1159–1172 (1972).

2-10. 修士論文: 面発光レーザと面発光レーザ増幅器の 高効率光結合集積化に関する研究, 鷹箸雅司, (2020).

2-11. A. M. A. Hassan, M. Ahmed, M. Nakahama, and F. Koyama, "High-power, quasi-single-mode vertical-cavity surface-emitting laser with near-diffraction-limited and low-divergence beam," Jpn. J. Appl. Phys. **59**(9), 90904 (2020).

Chapter 3

Field of view and resolution enhancement of VCSEL beam scanner

In this chapter, DOE-based optics and counter-propagation integration will be applied to enhance the field of view and resolution points number of VCSEL beam scanner demonstrated in chapter 2.

3.1 Field of view and resolution enhancement of solitary VCSEL beam scanner

Before talking about the method used to enhance the FoV and resolution, the target of FoV should be acknowledged as shown in table 3-1.

Table 3-1. FoV, power, size requirement of 3D sensing

Sensing range	FoV requirement	Power requirement	Size requirement	Cost
100m	30° × 30°	100W	Normal	High
50m	60° × 60°	25W	Normal	Normal
10m	90° × 90°	1W	Critical	Cheap
1m	120° × 120°	0.01W	Critical	Cheap

It is said that in the long-range application, the power is very important, the power penalty due to optics should be as small as possible, while for short-range applications, the power is not that important, the power penalty due to optics should be allowed to an extent. And the size and cost management in short-range is very important for short-range applications.

3.1.1 FoV and resolution enhancement of single solitary scanner

A straight and easily imaged way to expand the FoV of bean scanner is using a FoV expanding lens, for example a positive lens under defocusing operation. However, it is needed to consider that our beam scanner could be regarded as a expanded light source not a spot light source, it will lead to great overlap when beam steering. The simulation is made in Zemax. In the assumption, the beam scanner size is 2mm×3μm, the simulation result was shown in Fig. 3-1. The left figure shows original beam steering fan beam without expanding lens, they are clear 5 fan beams. Then a FoV expanding lens was added to the light source, the FoV was indeed expanded, but the beam divergence of 5 fan beams were greatly expanded larger than the expansion of steering range. Actually, when the light source is a spot light source for example the aperture is 3μm×3μm, it is possible to use a lens to expand the FoV. For expanded light source like VCSEL beam scanner, unless the focal length of lens is very large so that the VCSEL beam scanner could be regarded as a spot light source.

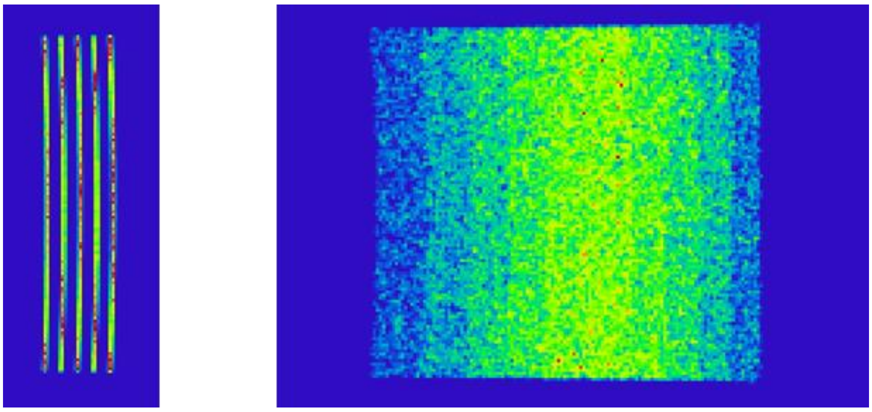

Fig 3-1 Simulation result of fan beam scanning without lens and with lens

Recently, for structured-light sensing dot pattern generation, diffractive optical element (DOE) was applied to expand the FoV of VCSEL array and shape the beam as design [1,2] as shown in Fig. 3-2. The DOE is a kind of flat optics on which the micro structured was formed to realize the specified function as shown in Fig. 3-3. The DOE could shape the beam to an designated pattern, such as lines, dots, matrix or random patterns.

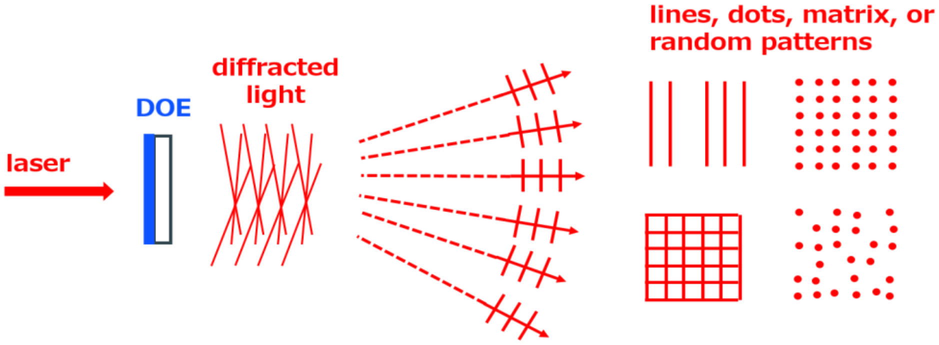

Fig. 3-2 Function of DOE to shape the beam

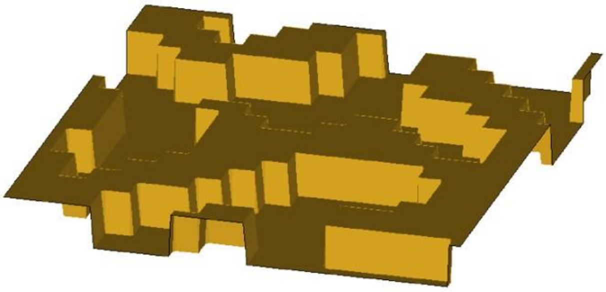

Fig. 3-2 Microstructure of DOE

There is a kind of DOE arising our attention that functions as a beam splitter [3]. The detailed function is shown in Fig. 3-2. A beam come from laser illuminates to a DOE, then the single beam will be split to designed orders of beams. In this figure, the designed number is 3 The separation between different orders observed the grating diffraction equation as shown in Eq. 3-1,

$$sin\theta_m = m\lambda/\Lambda \tag{3-1}$$

where θ_m is the diffraction angle of mth order, λ is the wavelength of incident light, Λ is the pitch size of the diffractive grating. There is some difference between the DOE and conventional grating, because DOE could adjust the intensity of different orders by adjusting the duty ratio within the pitch. In most cases, the intensity of different orders will be designed same.

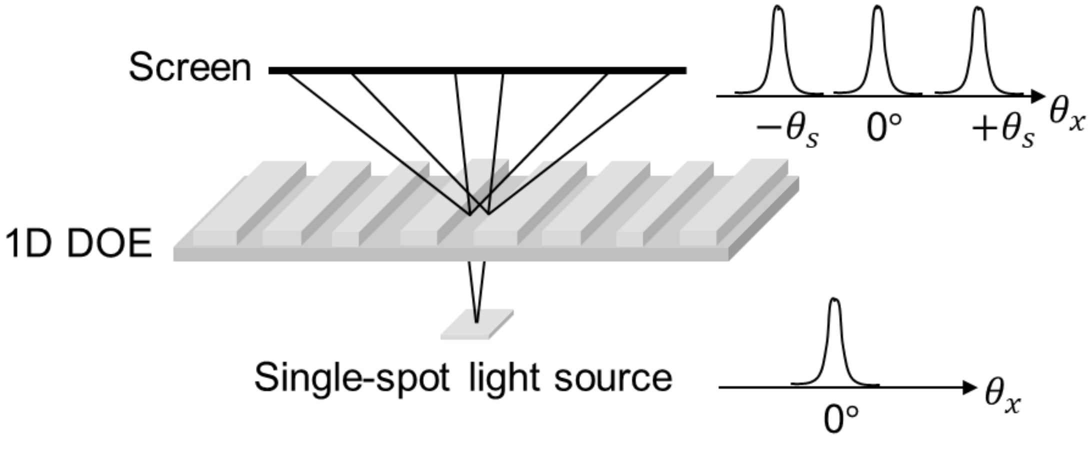

Fig. 3-3 Function of DOE as a beam splitter

Then we could assume such condition: *if the original beam scanned from 0th order to +1st order, the -1st order may be steered to 0th order and 1st order may also be steered for the similar angle* as illustrated in the Fig. 3-4. If this assumption is correct, when the beam steering angle θ_o of original light source is equal to the separation between different orders of DOE $\theta_s = \theta_1 - \theta_0$. The original FoV of θ_o will be increased to $\theta_2 - \theta_{-1}$. When the light is normally incident to the DOE, the $\theta_2 - \theta_{-1} \approx 3\theta_s$. Thus, we could conclude a more general statement that when θ_o=θ_s, by using a *n*-spot DOE, the FoV could be enhanced to $n\theta_s$= $n\theta_o$.

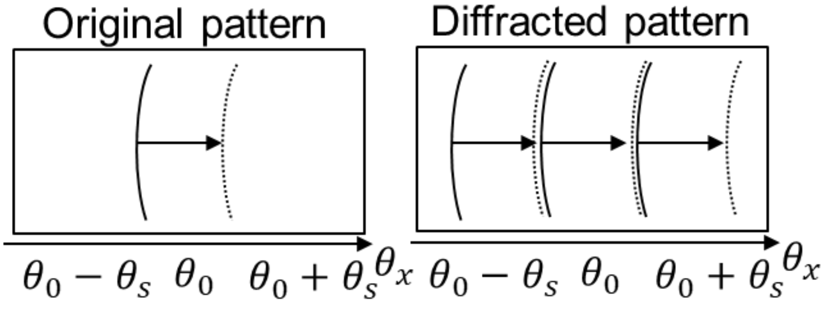

Fig. 3-4 Function of DOE using in beam steering devices

Then the deviation of the above-mentioned assumption. Here we need to discuss a more general condition for arbitrary incident angle to the DOE. When the incident angle is not normal, the diffraction angle θ'_m and the incident angle θ_i,

$$sin\theta_m = sin\theta_i - sin\theta_m \tag{3-2}$$

where θ_m is the diffraction angle of normal incident of a specialized DOE. Considering the condition of beam steering angle θ_o=θ_s=$\theta'_1 - \theta'_0$. The incident angle should be considered as from $\theta_{i(begin)} = \theta'_0$ to $\theta_{i(end)} = \theta'_1$. Therefore, at the beginning state, the diffraction angle $\theta'_{m(begin)}$ is:

$$sin\theta'_{m(begin)} = sin\theta'_0 - sin\theta_m \tag{3-3}$$

At the end state, the diffraction angle of the previous order $\theta'_{m-1(end)}$ could be derived as:

$$\begin{aligned} sin\theta'_{m-1(end)} &= sin\theta'_{+1(begin)} - sin\theta_{m-1} \\ &= sin\theta'_0 - sin\theta_1 - sin\theta_{m-1} \\ &= sin\theta'_0 - \left(\frac{\lambda}{\Lambda} + \frac{(m-1)\lambda}{\Lambda}\right) \\ &= sin\theta'_0 - \frac{m\lambda}{\Lambda} \\ &= sin\theta'_0 - sin\theta_m \\ &= sin\theta'_{m(begin)} \end{aligned} \tag{3-4}$$

It means when the beam steered from 0th order to 1st order, or the orders will be steered to the next order and therefore all the separation will be fulfilled even the incident angle is not normal. In this derivation, the wavelength was assumed constant, but for our beam scanner there might be a little difference for different deflection angle, this will lead to a very small space of <0.1° between highest order and sub-highest order when beam steered from 0th order to 1st order. This small space could be neglected, or it could be covered by a little over steering. From Eq. 3-1, we could also know that the separation between different orders may not be same especially for higher orders as shown in Fig. 3-5. In details, for the minus order, the separation will be smaller that of plus order. Therefore, the FoV enhancement may be larger than *n* times by using a *n*-spot DOE.

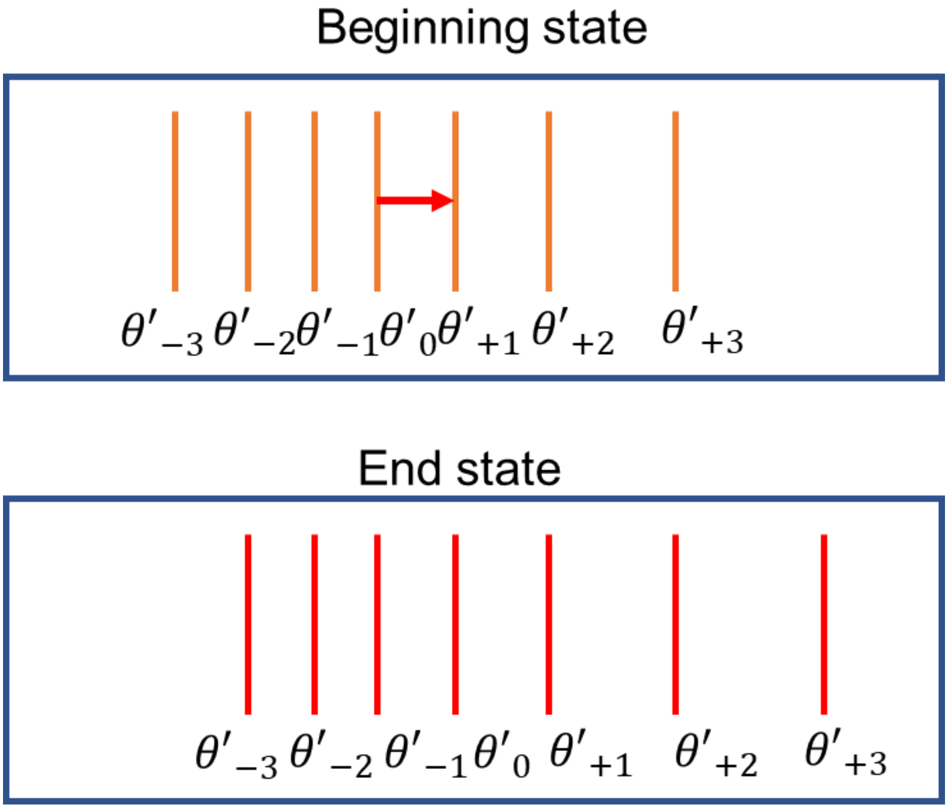

Fig. 3-5 Steering begin state and end state when the incident angle is not normal

Then a 3-spot DOE will be firstly used to demonstrate the FoV enhancement performance. The detailed microstructure of DOE was shown in Fig. 3-6. The grating structure could be easily seen. Its pitch size is about 4μm. As shown in Eq. 3-1 and the correspondence of separation and pitch size shown in Fig. 3-7, the separation for normal incident should be around 12° by using 840nm-band beam scanner. It could be also found the smaller diffraction separation angle indicates the larger pitch size will enable the easier lithography and fabrication process. In our study, the separation should be designed not lager than the maximum beam scanning angle θ_{max}. The duty ratio and etching depth were designed to make the only -1st, 0th, 1st order appear with similar intensity. Actually, from 835nm~850nm, the separation variation is as small as <0.2 ° as wavelength dependence of separation angle is shown in Fig. 3-8, which is why it is noted that the wavelength varying in the beam steering may not affect the fulfilling of separation, especially the wavelength varying is only less than 7nm in all of experiment shown in the following sections.

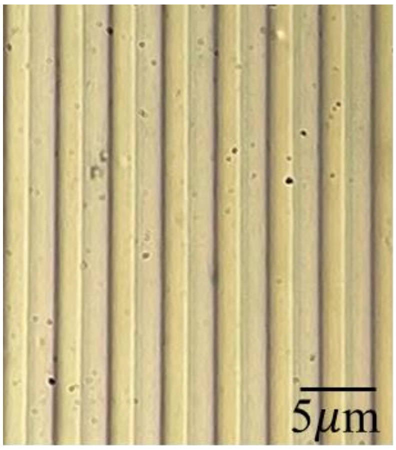

Fig. 3-6 The detail structure of a 3-spot DOE under microscopy

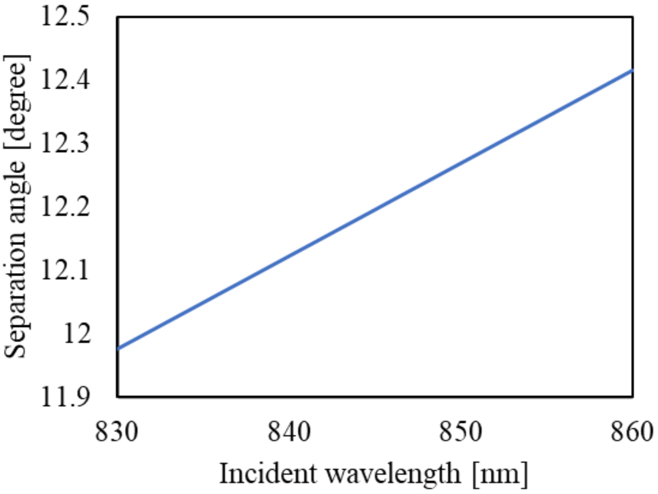

Fig. 3-7 Wavelength dependence of separation angle

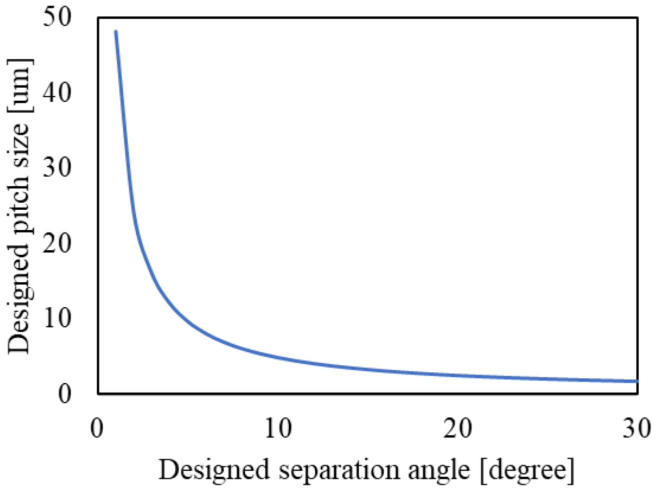

Fig. 3-8 Design of pitch size depending on the separation angle

Based on the previous analyzing of DOE, the flow of deigning the DOE could be obtained as Fig. 3-9 shows. Firstly, the pitch size should be designed based on the required separation angle. It is noted that the separation angle should be smaller than maximum steering angle of beam scanner. Then depending on the application, the number of spot should be decided to get the FoV of $n\theta_s$. The sub microstructure within the pitch should be designed based on the requested number of orders. If the designed microstructure is too small to be fabricated, the θ_s and n should be decided again and if the manufacturability is okay, the DOE could be fabricated by the lithography and selective etching.

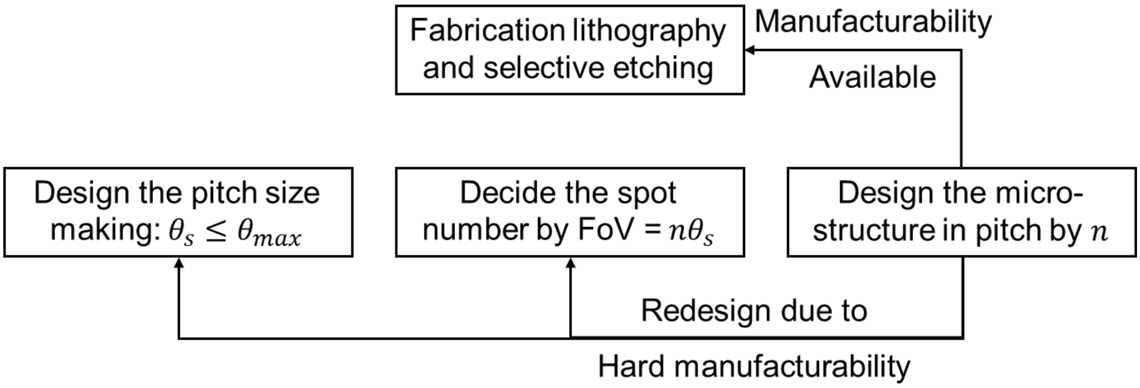

Fig. 3-9 Flow of deigning the DOE

Here, some examples of available DOE and its expectation of FoV that will be used in the study was shown in Table 3-2.

No.	θ_s	*n*	Expected FoV*	Application
①	12°	3	>36°	Single scanner
②	6°	7	>42°	Counter-propagation**
③	4°	10	>40°	2D beam steering***

* The real FoV should be highly depending on the incident angle and always be larger

** The counter-propagation beam scanner needs larger FoV to cover the vertical field but increasing θ_s and *n* of ① is difficult.

*** The maximum beam steering angle for lens collimation (that is required for 2D beam scanning) is limited to 4°

To measure the FFP of solitary beam scanning equipped with a 3-spot DOE ①, the experimental setup as shown in Fig. 3-10 was established. The fiber and probe are used to couple external light to the scanner and inject the current to the scanner. A 3-spot DOE is set 1cm above the beam scanner. The light will go through the DOE and be captured by the FFP camera.

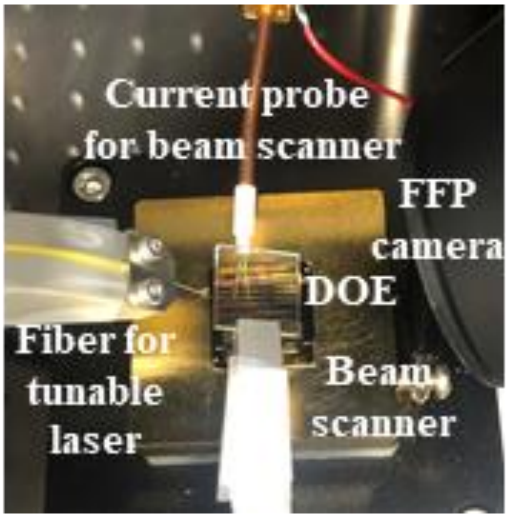

Fig. 3-10 The setup of measuring the beam scanner equipped with a 3-spot DOE

Firstly, When the wavelength of 840nm was coupled to the beam scanner and current of 500mA was injected into the scanner. The FFP with and without being equipped with DOE was shown in Fig. 3-11 and Fig. 3-12.

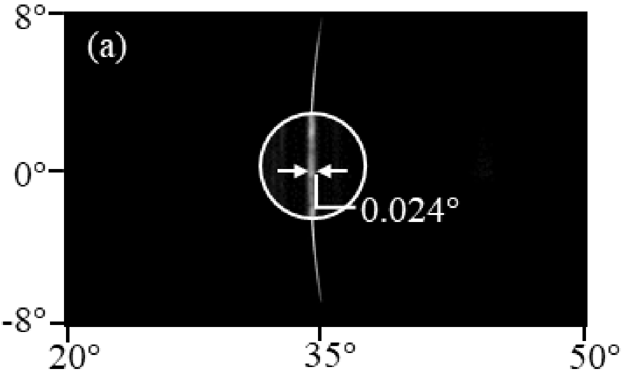

Fig. 3-11 The FFP of measurement without equipment of DOE

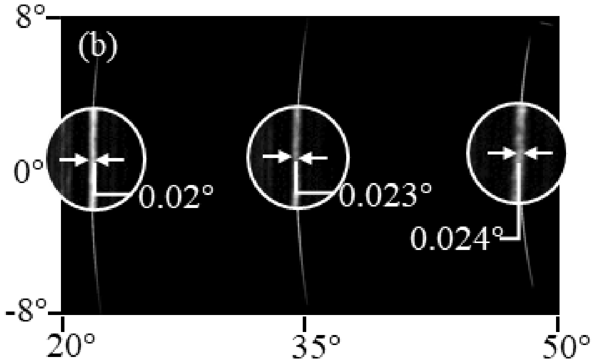

Fig. 3-12 The FFP of measurement with equipment of DOE

The zoomed figure in the circle is the FFP measured under high-resolution mode to indicate the beam divergence. We could see that the beam was split to three beams with separation angle of around 12°, which may be affected by the incident angle. The split three beams also maintain unchanged beam divergence. The beam intensity variation of three beams is also smaller than 10%. Then when tuning the wavelength of coupled light from 836.8nm to 844.5nm, the beam was scanned by 12° to cover the separation between 0th order and 1st order. The overlapped FFP of beam steering is shown in Fig. 3-13.

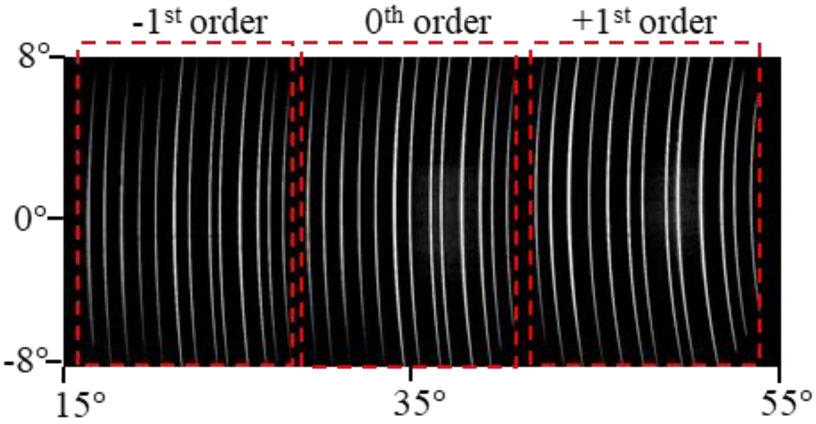

Fig. 3-13 The FFP of measurement with equipment of DOE

We could find that the separation was just fulfilled. The total FoV also was increased from 12° to >36°. Considering the unchanged beam divergence of about 0.023°, the resolution was increased to >1,200.

3.1.2 *FoV and resolution enhancement of counter-propagation solitary scanner*

It is easy to be imaged that because the single scanner could scan from 15° to 55°, the symmetrical FoV of -15° to -55° could be also covered if a counter-propagation beam scanner could be covered. However, if still a 3-spot DOE was used there will be a gap from -15° to 15° is not covered, which leads to big problem for real application. A promising way is to increasing the number of spots of DOE for example by using a 7-spot DOE. The FoV could be further enhanced and thus cover the vertical direction. However, 7-spot DOE with separation of 12° is very difficult to be fabricated. To remain the intensity of the larger order diffraction more precise microstructures should be made in the 4μm pitch, which is difficult to be manufactured. Therefore, although we chose a 7-spot DOE ②, the separation angle was reduced to around 6°. It means the pitch size of grating will be increased to around 8um, which enables the microstructure design and fabrication. The detailed schematic of the counter-propagation beam scanner equipped with DOE is shown in Fig. 3-11.

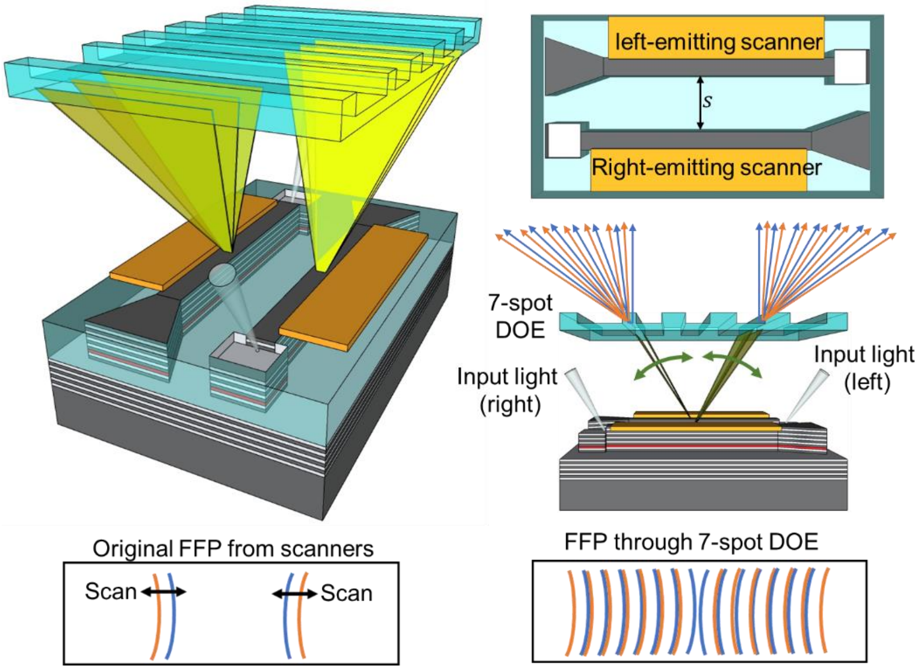

Fig. 3-11 Schematic of the counter-propagation beam scanner equipped with DOE

The counter-propagation scanners were fabricated as shown in Fig. 3-12. The length is 6mm for smaller beam divergence.

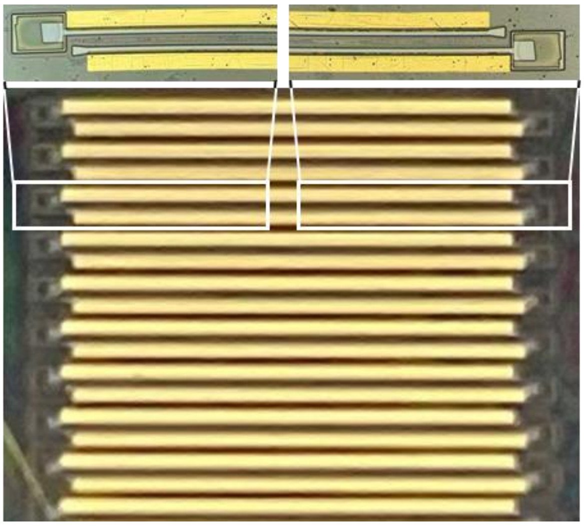

Fig. 3-12 Photo of counter-propagation solitary beam scanners

To finish the counter-propagation measurement, the setup shown in Fig. 3-13 was established. Two fibers were used to couple the light to counter-propagation scanners.

Probe could switch between two scanners to select the operation scanner. A 7-spot DOE was put above the scanner.

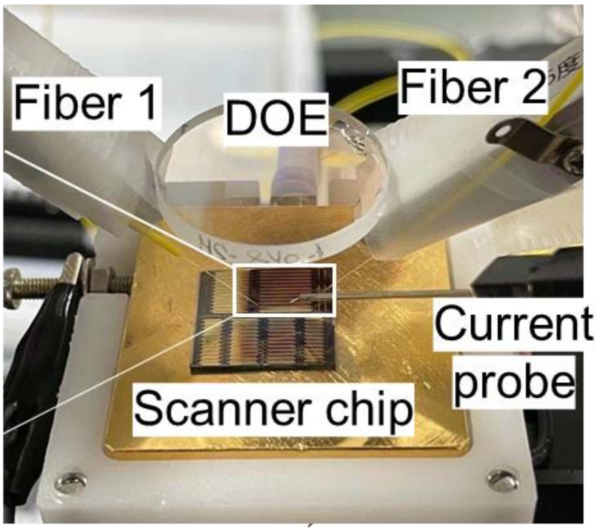

Fig. 3-13 Photo of setup to measure the counter-propagation scanners with DOE

Firstly, the static FFP when the wavelength is fixed at 844.5nm and 841nm were shown in Fig.3-14 for right-emitting beam scanner. When wavelength is 844.5nm we could find the separation between 0th order and 1st order is about 7.1° from the figure. It is different from the designed 6°, because the incident angle when the wavelength is 844.5nm is around 28° but not normal. If the incident angle getting larger, the separation will also get larger. Actually, by tuning the wavelength from 844.5nm to 841nm, the beam of 0th order will just overlap with 1st order. It could be seen that all the other orders were also covered by the previous order. It witnessed the previous statement discussed in Section 3.1.1. The Static FFP when the wavelength is fixed at 841.6nm and 845nm for the counter-propagation beam scanner was also measured. They show the asymmetrical FFP as shown in Fig 3-15.. The tuning wavelength could be a little different because the uniformity though the wafer. As mentioned previously, the separation between different order may be different because the incident angle from beam scanner is not normal. When the incident angle is 28°, the separation between different orders is varied from 6.7° to 8.8°

for the right-emitting beam scanner. The similar result could be found for left-emitting beam scanner, the separation varied from 6.5° to 9.3° from Fig. 3-16. The difference between left- and right-emitting scanner may come from the measurement precision of the system and the placement angle of DOE.

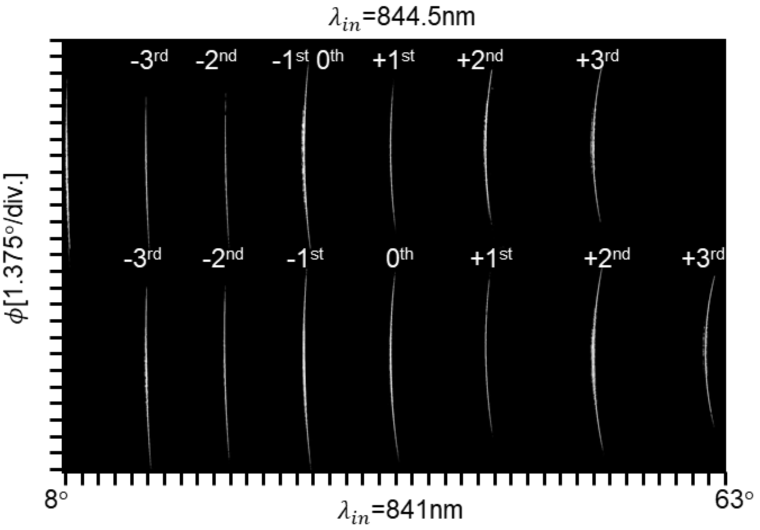

Fig. 3-14 Static FFP for right-emitting beam scanner

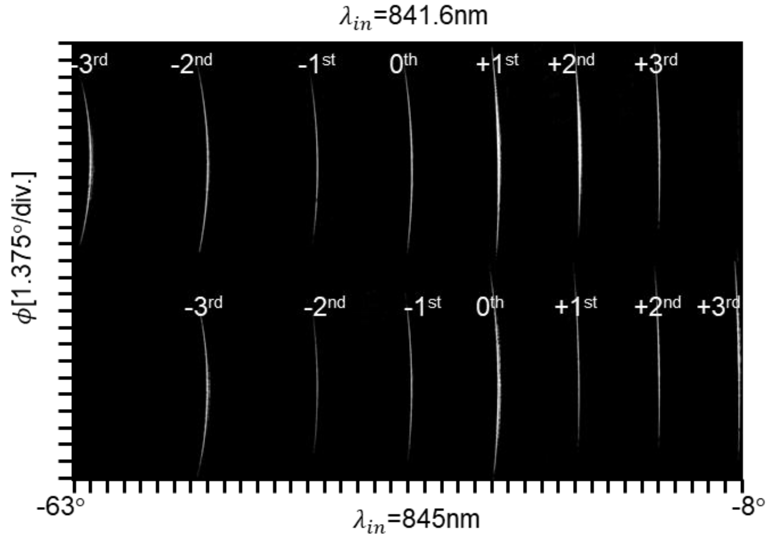

Fig. 3-15 Static FFP for left-emitting beam scanner

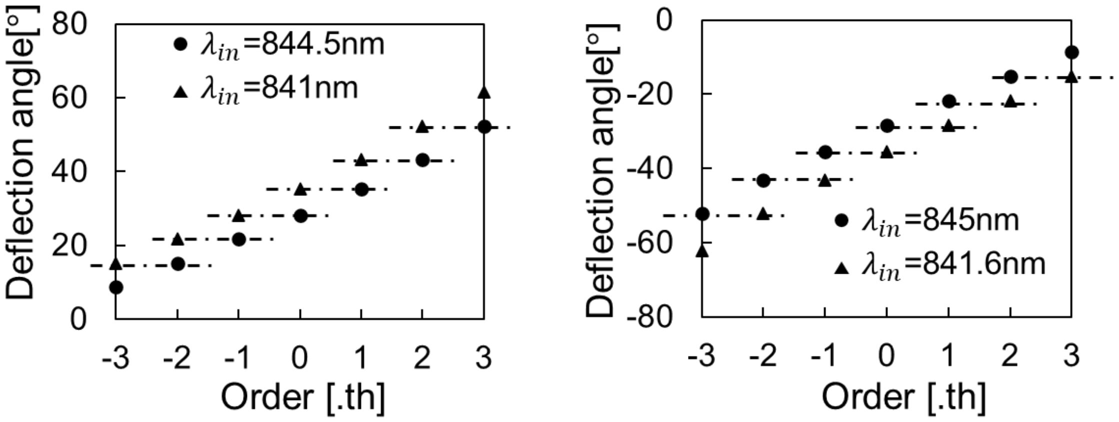

Fig. 3-16 The deflection angle of different orders when beam was steered from 0th order to 1st order for right- (left figure) and left- (right figure) emitting beam scanner

Then the wavelength of coupled light was tuned by four steps from 841nm to 844.5nm for right emitting beam scanner and 841.6nm to 845nm for left-emitting beam scanner. The overlapped beam scanning FFP was shown in Fig. 3-17, where the top figure and bottom figure correspond to the right and left emitting beam scanner respectively. It covers the symmetrical field of view of around 55° aligned in two sides of vertical direction.

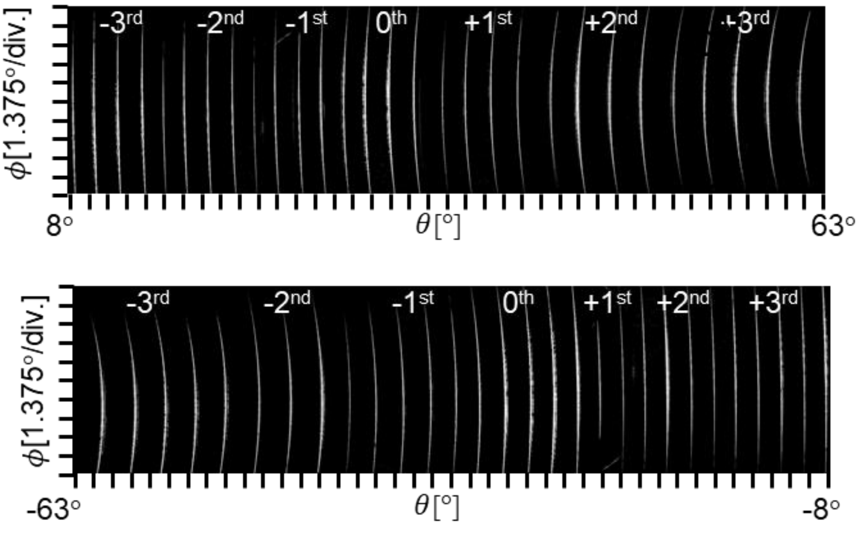

Fig. 3-17 The overlapped FFP of beam scanning for counter-propagation beam scanners

As mentioned before, because the incident angle is not normal, the actually single-side FoV is much larger than the expected FoV for DOE ② in Table 3-2. From the Fig. 3-17, It could be also found that there is a gap between -8° to 8°, the method to cover this region will be discussed later. To show the resolution of this scanner, the beam divergence was measured under high-resolution mode of FFP camera as shown in Fig. 3-18. The beam divergence will be increased with order increasing as Eq. 3-1 shows. Therefore, the beam divergence is almost periodically increasing with the order increasing. The average beam divergence between the 0^{th} order and 1^{st} order for right- and left-emitting beam scanner are around 308, so the total resolution points in the whole FoV is $308\times14=4312$, which meet the requirement for almost all the 3D sensing applications. The beam intensity fluctuations (Defined as the standard deviation of all beam intensity/ average beam intensity of all beams) could be 36%. The beam intensity fluctuations were affected by many factors including beam intensity variation of beam scanner (that may result from the gain difference of different wavelength or the intensity variation of external light source for different wavelength. This issue actually does not contribute significantly to the final result and could be solved by adjusting the $I_{scanner}$ to compensate the gain difference for different λ_{in}), and the intensity variation of different orders split by the DOE (that may result from the design method of DOE. In most case, the design was made for normal incident. Therefore, when the beam is not normally incident to the DOE, the beam intensity variation may occur. Another thing is the fabrication process of DOE may also lead to the intensity variation, even in design the intensity could be almost same. Normally, the good intensity uniformity should be designed by smaller microstructure in the pitch and even the multi-step selective etching is needed [3 – 6]. It also requires the improvement in the fabrication process of DOE, for example introducing EBL in the fabrication process. Despite the intensity fluctuation, the weakest intensity could be regarded as the evaluation target of depth measurement accuracy, because if the weakest beam could provide enough accuracy, the stronger beam must be better.)

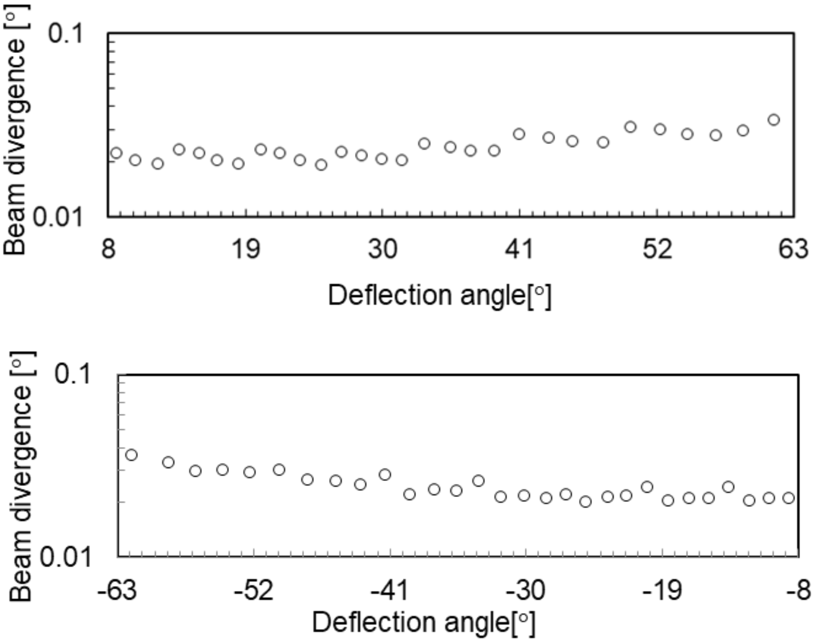

\

Fig. 3-18 The beam divergence in the total beam steering range

To cover the vertical range, firstly we could reduce the scanner length to 2mm. As mentioned previously, the shorter scanner has larger amplification spectrum width. It is to say that we could choose larger operation wavelength to make the deflection angle closer to the vertical range. An example was shown in Fig. 3-19. It successfully covers the vertical range. However, as discussed before, the shorter scanner has larger beam divergence, thus smaller resolution points number. Combing the 2mm and 6mm beam scanner on the same chip may be possible, but the total chip size and the yield will be another problem. Besides, by combing two-length scanner will lead to the overlap of beam scanning in some region, which will increase the intensity uniformity received by the camera in the real applications.

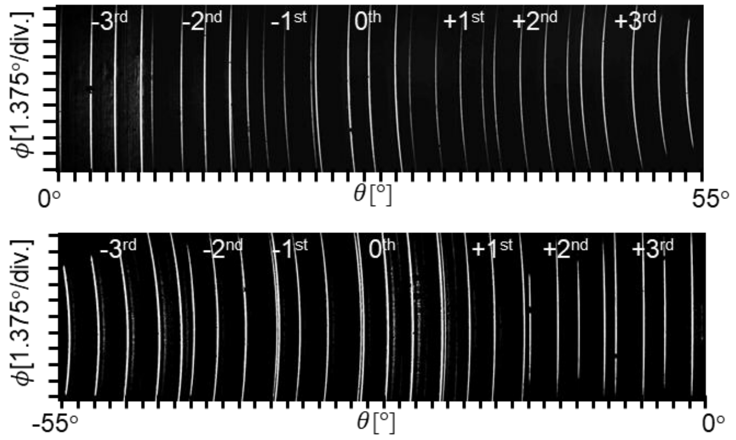

Fig. 3-19 Overlapped FFP by using a 2mm-long beam scanner

Actually, as shown in Eq. 1-1, the deflection angle is related to the operation wavelength λ_{in} and resonant wavelength. If the resonant wavelength could be reduced, the deflection angle could be smaller. As calculation based on Eq. 1-1, by reducing the resonant wavelength by 5nm, the 6mm-long beam scanner could cover the vertical range with the DOE and the beam intensity could be better because the incident angle is closer to normal direction. To reduce the resonant wavelength, it is to a little reduce the thickness of each pair of DBRs. It is easy to be realized in new fabrications. Another choice is to change the available λ_{in}. Actually, the external tunable laser could provide enough tuning range to cover the vertical range by current resonant design. However because the limited amplification spectrum of the beam scanner, the available λ_{in} is limited. The amplification spectrum is related to the PL wavelength of quantum wells. It is also easy to make the PL wavelength red shift when wafer growth to make the available λ_{in} closer to the resonant wavelength and thus to make the deflection angle closer to the vertical direction as calculated by Eq. 1-1. The red shift of PL wavelength of 5nm is enough.

3.2 Field of view and resolution enhancement of solitary VCSEL beam scanner integrated to the seed laser

3.2.1 FoV and resolution enhancement of single scanner integrated to the conventional VCSEL

Thanks to the easier manufacturability and compactness availability, the FoV and resolution enhancement of the integrated beam scanner is very important. Firstly the FoV and resolution of the single beam scanner will be demonstrated. Because the DOE ① has separation angle of 12°, the beam scanner integrated to the slow-light VCSEL may not be compatible. Therefore, the beam scanner integrated to the conventional VCSEL was used to make the demonstration. The measurement setup is similar to that of solitary beam scanner, where the lensed fiber was replaced by another current probe to drive the VCSEL as shown in Fig. 3-20.

Fig. 3-20 Setup to measure the beam scanner integrated to a conventional VCSEL

Firstly, the static FFP when the I_{VCSEL} =3mA and $I_{scanner}$=50mA was captured in Fig. 3-21 (without equipment of DOE) and 3-22 (with equipment of DOE). The original beam divergence is about 0.12°, and by using a DOE, the beam was split to three beams with same separation of 12°, similar beam divergence and similar beam intensity.

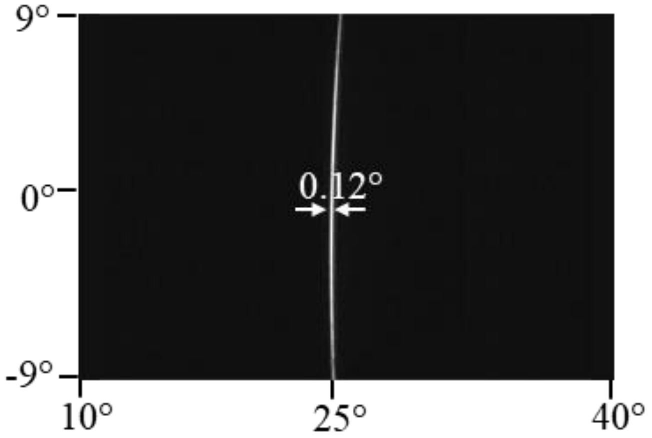

Fig. 3-21 Static FFP of beam scanner without equipment of DOE

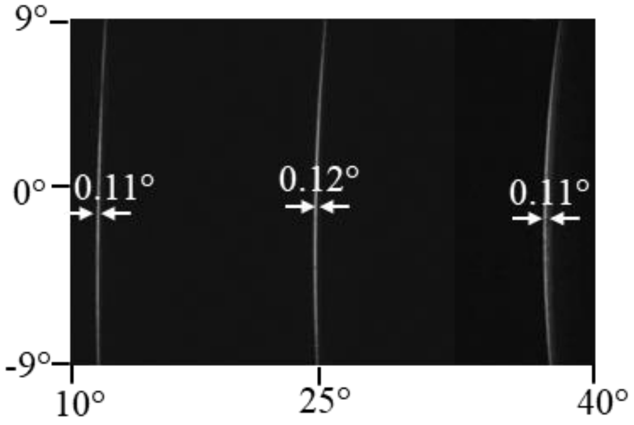

Fig. 3-22 Static FFP of beam scanner with equipment of DOE

Then by tuning the I_{VCSEL} from 1.5mA to 5mA, the beam will scan from 19° to 31° and covered the separation between 0th and 1st order. As discussed before, the all the separation will be covered at the same time, so the total field of view from 7° to 43°, which cover the FoV of 36° as shown in Fig. 3-23. Considering the unchanged beam divergence of around 0.12°, the resolution number could be increased from 100 to 300.

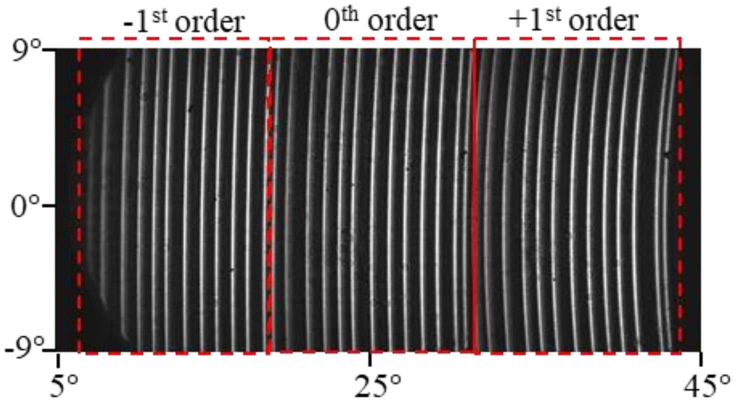

Fig. 3-23 Overlapped FFP of beam scanner with equipment of DOE

The beam scanner used here is a 1mm-long scanner, the resolution could be improved by extending the scanner length. This 1mm-long scanner equipped with a 0.625mm DOE will provide a very compact beam steering module. Its module size will be smaller than 1mm×1mm×1mm, which could be directly used in the mobile phones for short-range applications.

3.2.2 FoV and resolution enhancement of counter-propagation scanner integrated to the slow-light VCSEL

In this section, the DOE ② was selected to enhance the FoV and resolution of beam scanner due to limited maximum beam scanning angle of beam scanner and available fabrication process of DOE. Before measuring the counter-propagation beam scanners, the problem of too large deflection angle of beam scanner makes it difficult to cover the vertical range. Not like the solitary beam scanner to red shift the PL wavelength or blue shift the resonant wavelength, the slow light lasing request enough shift between PL wavelength and resonance wavelength. A simple and efficient way is to add a mirror to make the deflection angle closer to the vertical direction. However, adding a flat mirror above the beam scanner is very difficult in manufactory and very difficult to reflect the light from both of counter-propagation scanner to vertical direction. In the previous structured-light sensing, a prism was used to hold the DOE for package manufactory [2] and also as shown in Fig. 3-24. If the prism is coated by high-reflectivity materials, such as dielectrics and gold. The prism will form as a mirror to reflect the light coming from the beam scanner.

Fig. 3-24 The previous module using a prism mirror to reflect the light [2]

Therefore, the following module for enhancing the FoV and resolution by equipping the prism mirrors, DOE and counter-propagation scanners are proposed in Fig. 3-25.

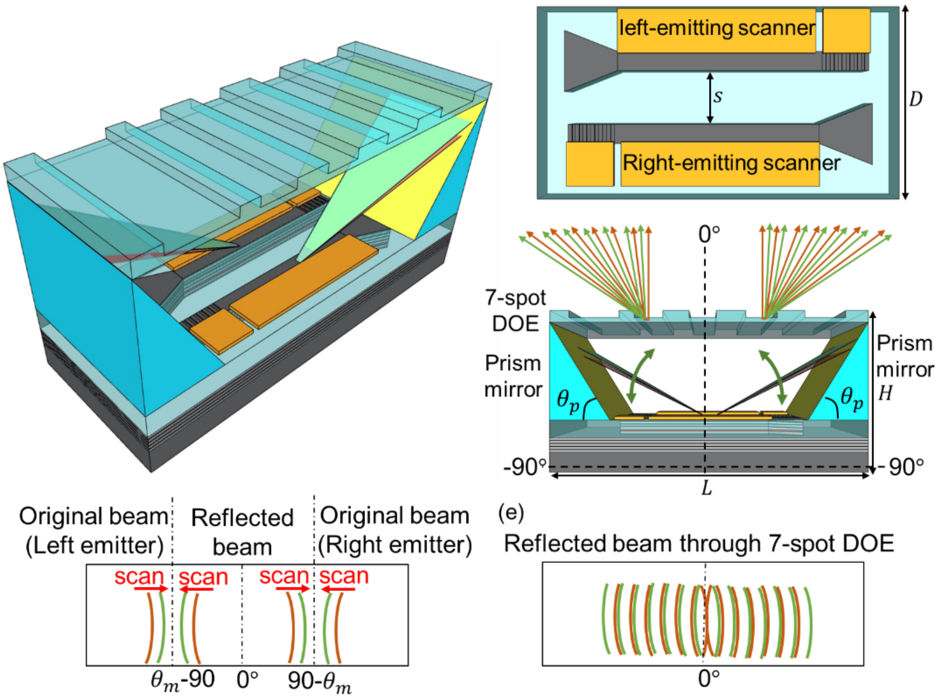

Fig. 3-24 The proposed beam scanning module

Because the introducing of optics, we call the total system including beam scanner and optics beam scanning module. The scanned beam from right- and left- emitting beam scanner will be mirrored by the prism mirror and then split by the DOE to cover the entire FoV including the vertical range. To make the beam scanner range cover the vertical range, the slope angle of prism should be exactly controlled. Assuming the largest deflection angle is θ_{dm}, and a n-spot DOE with separation of θ_s is used to enhance the FoV, the slope angle of prism θ_p should be design as Eq. 3-5, why the largest deflection angle is considered is after reflection by mirror the beam of original largest deflection angle will goes to the closest beam to vertical in the whole beam scanning range.

$$180 - 2\theta_p - \theta_m - \frac{n-1}{2}\theta_s = 0 \tag{3-5}$$

where the θ_s is considered constant for all the orders, in the real application, it could be calibrated before large-scale manufactory. Actually, this calculation is only related to the minus orders of DOE, whose separation will be almost same as deign. The relation between the largest deflection angle and designing of prism slope angle ② (7-spot, θ_s= 6°) is shown in Fig. 3-25.

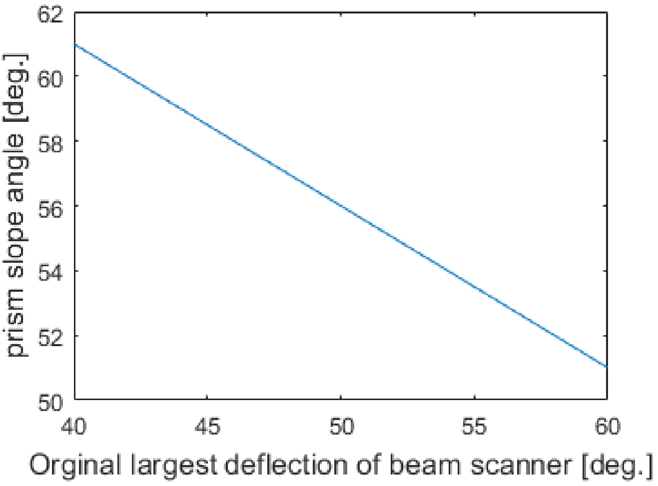

Fig. 3-25 The relation between the largest deflection angle and prism slope angle

In this study, the θ_{dm} should be 55°, so he θ_p should be 53.5°. For the certainty of covering the vertical range 54° was chosen, which enables the beam to cover the -1°. The expectation of the size of prism is also important because it aims at making a compact module. The slop of prism mirror should be large enough to accept all light emitted from the extended light source as shown in Fig. 3-26.

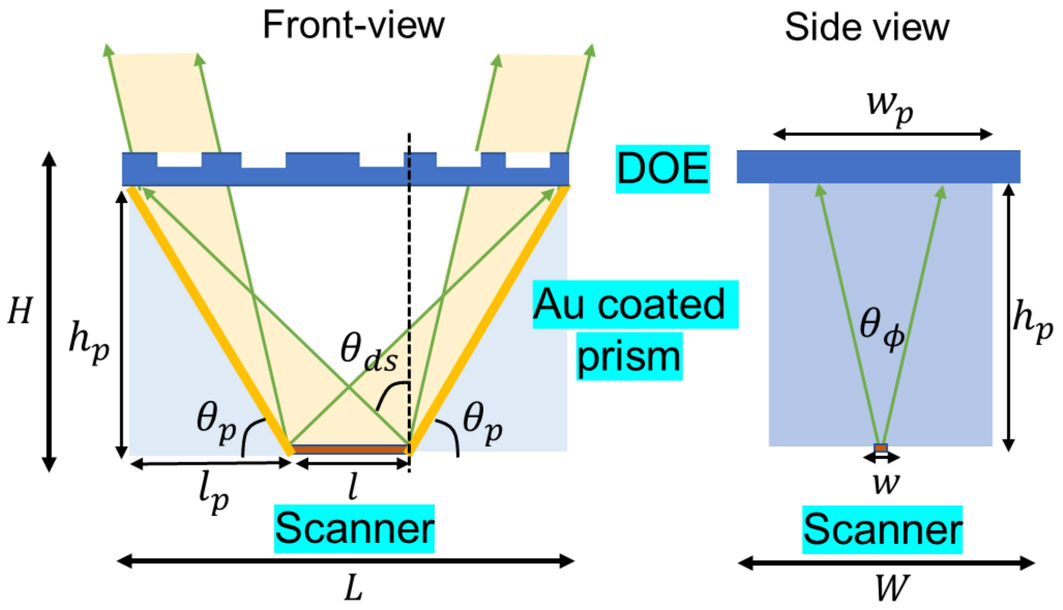

Fig. 3-26. The illustration of prism mirror design

In the estimation of size of prism, the smallest deflection angle of θ_{ds} should be considered and the beam divergence in θ direction is too small to affect the design, so it was assumed to be 0. Thus, the size of prism mirror h_p, l_p, w_p could estimated as Eq. 3-6,

$$l_p = \frac{l tan(90-\theta_{ds})}{tan\theta_p - \tan(90-\theta_{ds})}$$

$$h_p = tan\theta_p \cdot l_p \tag{3-6}$$

$$w_p = 2h_p \tan\left(\frac{\delta\phi}{2}\right)$$

where the l and w are the length and width of beam scanner, $\delta\phi$ is beam divergence of beam scanner in ϕ direction. The total module size H, L, W could be also calculated by Eq. 3-7.

$$L = 2l_p + l$$

$$H = h_p + t_{DOE} + t_{wafer} \qquad 3\text{-}7$$

$$W = 1.5w_p$$

where t_{DOE} and t_{wafer} are the thickness of DOE and wafer, their summation may be 1mm. The W is calculated as $1.5w_p$ to make the clear aperture enough. Based on the above-mentioned Eq. 3-5~3-7. Because the steering range should be covering the θ_s, $\theta_{ds}= \theta_{dm} - \theta_s$. The total module size with different scanner length and different kinds of DOE could be calculated as shown in Fig. 3-27. It could be found that larger scanner length requires larger module size. Especially in this study, 2-mm scanner and a 7-spot DOE was used. It could be found that the module size could be 9mm×6mm×5mm, which might be the smallest electrical driven beam scanner with larger than 100° beam steering range. By shortening the beam scanner length to 1mm, the module size could be almost half to 4.5mm×3mm×2.5mm. Of course, the total resolution points may be half and the beam divergence may be increased to 0.1°, for short-range detection that has been used in mobile phones it is enough. By using a DOE with smaller number of spots, for example 3-spot DOE as shown in the orange line in the Figs. The total module size could be reduced to 3mm×3mm×2mm, which may be more compatible for the application in mobile devices. Actually, prism could replace the prism mirror by refracted deflection, which will be shown later. It may improve the module size even for application with long scanner length.

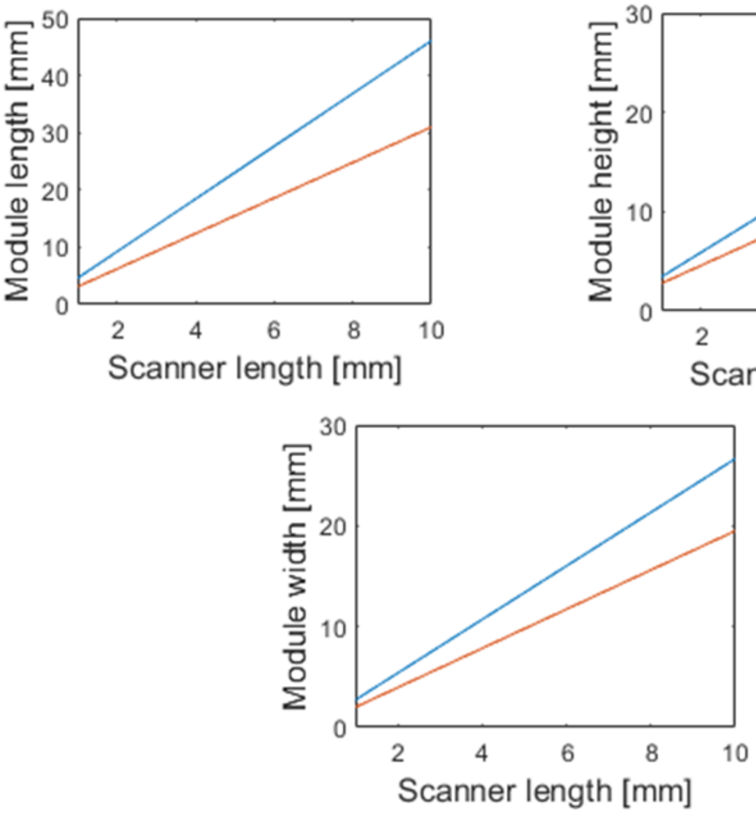

Fig. 3-27 The relation between scanner length and module size (orange: 3-spot DOE; blue: 7-spot DOE)

Here, a table is also shown about the choice of using different scanner length and different DOE for different potential applications, where $\delta\theta$ is the beam divergence in θ direction and the height of module may be most critical in most applications.

n	θ_s	FoV	l	$\delta\theta$	H	Potential application
3	6°	>36°	1mm	0.1°	2.8mm	Mobile phones
7	6°	>84°	1mm	0.1°	3.4mm	Mobile phones
7	6°	>84°	2mm	0.06°	5.8mm	House robot or LiDAR

Then the measurement by using the 2mm-long counter-propagation beam scanner and a 7-spot DOE will be demonstrated. The measurement setup was shown in Fig. 3-28. The photo of scanner chip was also shown in the left. Two prism mirrors were stacked on the scanner chip and DOE was placed on the prism mirror. Two probes were used to drive the slow-light VCSEL and the beam scanner. The light emitted from the module will be captured by the FFP camera.

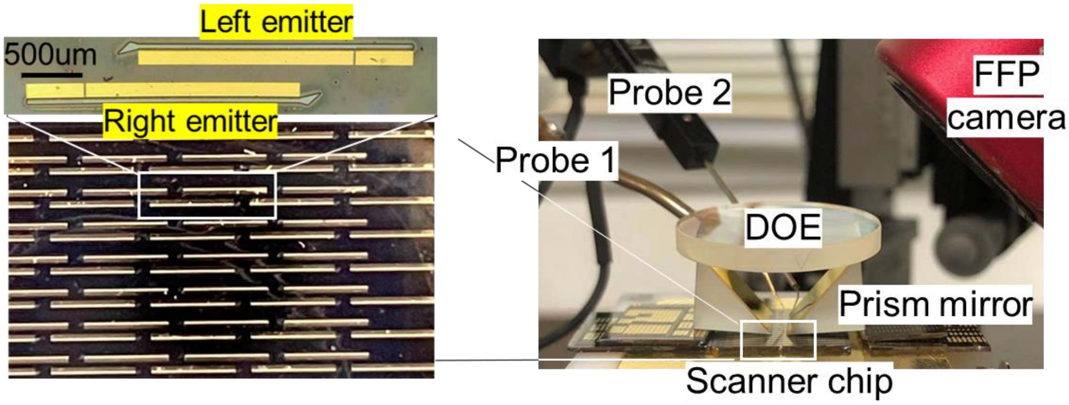

Fig. 3-28 The measurement setup of counter-propagation beam scanner

The static FFP when the I_{VCSEL} is 40mA and 267mA for left-emitting beam scanner and 40mA and 270mA for right-emitting beam scanner were shown in Fig. 3-29. The two different current corresponds to the start and end state of beam scanning, which just cover the separation between 0th and 1st order. As previously mentioned, the other separation will be covered at the same time. And different from that of solitary beam scanner, the beam was mirrored, so the curve direction was also inversed. The smallest order covered the vertical direction thanks to the deflection of prism mirror. The separation between 0th and 1st order is around 7°, which is larger than the design due to the non-normal incident.

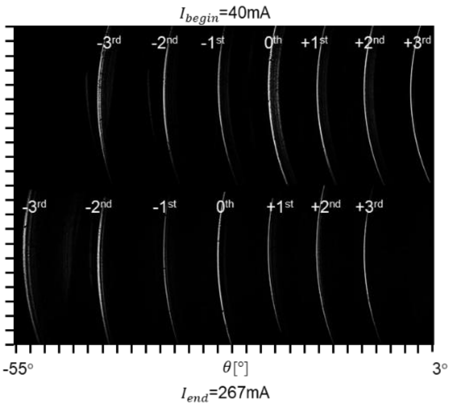

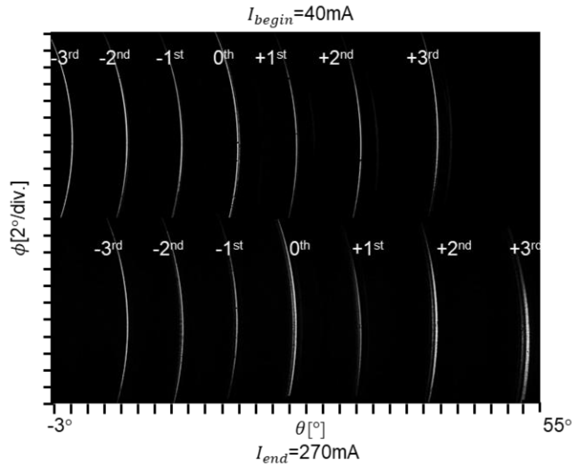

Fig. 3-29 The static FFP of counter-propagation beam scanner (Top: left-emitting beam scanner; Bottom: right-emitting beam scanner)

The overlapped beam steering when the I_{VCSEL} was tuned by 4 steps was shown in Fig. 3-30. The continuous FoV without gap from -55° to 55° was covered. To claim the total resolution points number, the beam divergence was also measured through the who FoV as shown in Fig. 3-31. Similar to the solitary beam scanner, when the beam is diffracted to the larger order, the beam divergence shows increasing tendency. The resolution will be decided by the original beam divergence when the beam was steered from 0^{th} order to 1^{st} order. The average beam divergence is 0.07° the resolution points number in the original 0^{th} to 1^{st} order should be 100. There fore the total resolution with DOE and counter-propagation should be >1400. In some region, the side mode could be found, although it is very weak. It could be avoided by better fabrication process including the electrode optimization, oxidation optimization and the grating forming optimization. The grating depth and etching depth may be critical, but it could be improved and be used to get narrower beam divergence [7].

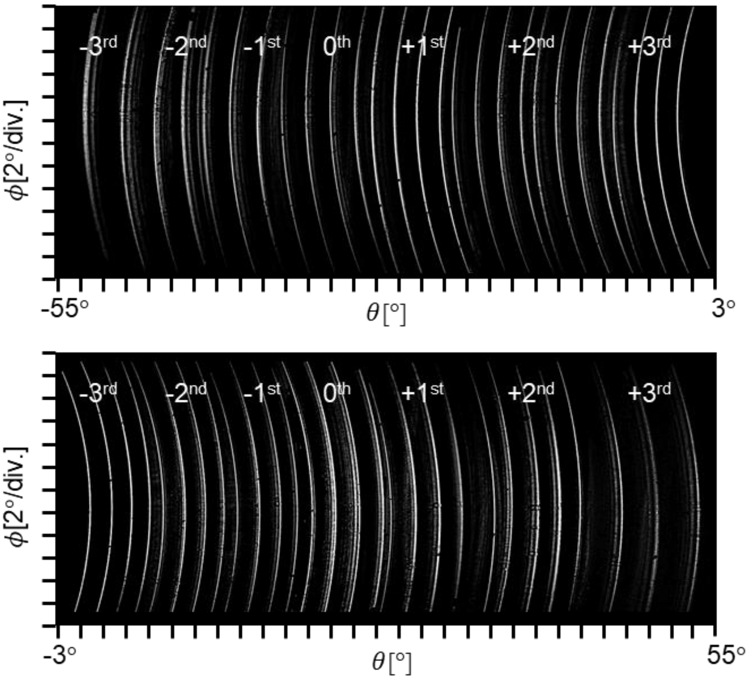

Fig. 3-30 The overlapped FFP of counter-propagation beam scanner (Top: left-emitting beam scanner; Bottom: right-emitting beam scanner) and

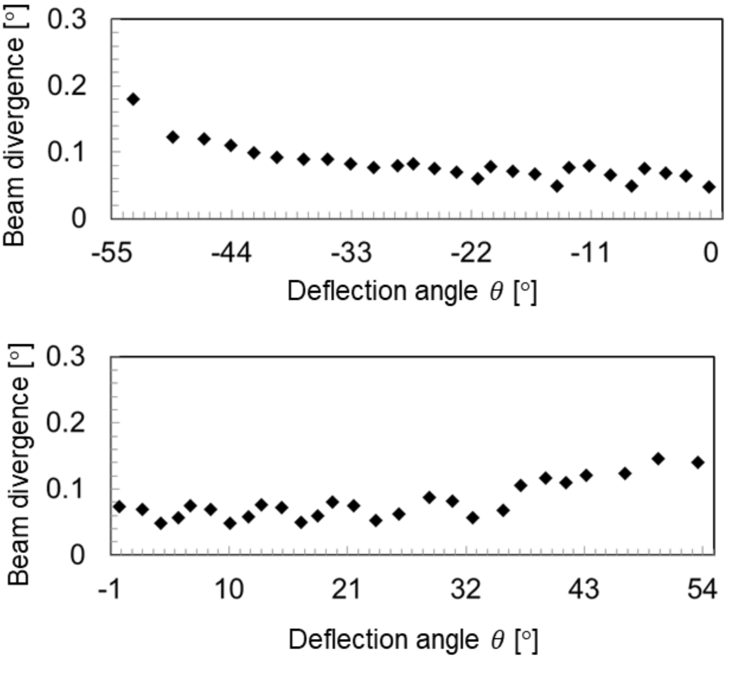

Fig. 3-31 The beam divergence of counter-propagation beam scanner (Top: left-emitting beam scanner; Bottom: right-emitting beam scanner) and

Reference in Chapter 3

3-1. B. Pesach and Z. Mor, "Projectors of structured light," (2014).

3-2. Z. Mor and B. Morgenstein, "Overlapping pattern projector," (2018).

3-3. C. C. Lee, Y. C. Chang, C. M. Wang, J. Y. Chang, and G. C. Chi, "Silicon-based transmissive diffractive optical element," Opt. Lett. **28**(14), 1260 (2003).

3-4. D. C. Kim, A. Hermerschmidt, P. Dyachenko, and T. Scharf, "Inverse design and demonstration of high-performance wide-angle diffractive optical elements," Opt. Express **28**(15), 22321 (2020).

3-5. H. Pang, S. Yin, G. Zheng, Q. Deng, L. Shi, and C. Du, "Design the diffractive optical element with large diffraction angle," Hologr. Diffractive Opt. Appl. VI **9271**(November 2014), 92711M (2014).

3-6. Z. Song, S. Tang, F. Gu, C. Shi, and J. Feng, "DOE-based structured-light method for accurate 3D sensing," Opt. Lasers Eng. **120**, 21–30 (2019).

3-7. S. Hu, A. Hassan, X. Gu, M. Nakahama, S. Shinada, and F. Koyama, "Surface grating VCSEL-integrated amplifier/beam scanner with high power and single mode operation," Appl. Phys. Express **14**(6), 62005 (2021).

Chapter 4

2D beam steering with enhanced field of view and resolution

In this chapter, 2D beam steering will be demonstrated by integration of VCSEL beam scanner array and by cylindrical lens. The field of view and resolution will also be enhanced by DOE-based optics.

4.1 Principle of 2D beam steering and FoV/resolution enhancement

4.1.1 Principle of fan beam collimation and focal-plane-based 2D beam steering

Before talking about the principle. The importance of 2D beam steering should be estimate. 2D beam steering means spot pattern beam steering in orthogonal two directions spot by spot. Compared to the fan beam scanning in one direction, spot beam means better power concentration and larger power density. For instance, if a fan beam with fan angle $\delta\phi$ of $10°$ was collimated to a spot with beam divergence of 0.1°, assuming the beam divergence in orthogonal direction $\delta\theta$ is unchanged. The power density (power/mm^2) should be improved by 100 times. Reflecting on the FFP measurement, the intensity of spot beam will be large then spot beam by 100 times.

Beam collimation is usually completed by collimation lens [1][2,3] as shown in Fig. 4-1.The collimation lens could be a concave lens. However, for the fan beam the collimation is only needed in the extended direction, in our case ϕ direction. It is wanted that in the orthogonal θ, the beam could be propagating as it is, so the cylindrical lens will be adopted in the collimation of our fan beam emitted by the beam scanner.

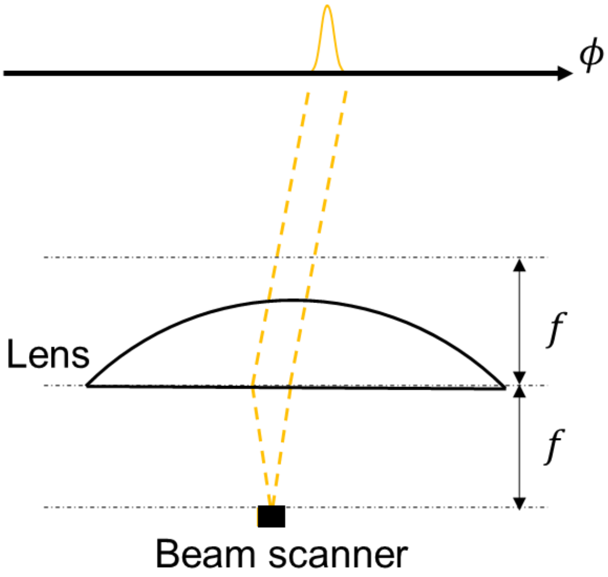

Fig. 4-1 The collimation schematic by using a collimation lens

The beam divergence after collimation is related to the original beam divergence and the focal length of cylindrical lens. Assuming the diffraction-limited beam collimation is completed when M^2=3 and assuming the original beam divergence $\delta\phi$ is about 10°. The intensity improvement by beam collimation could be obtained in Fig. 4-2.

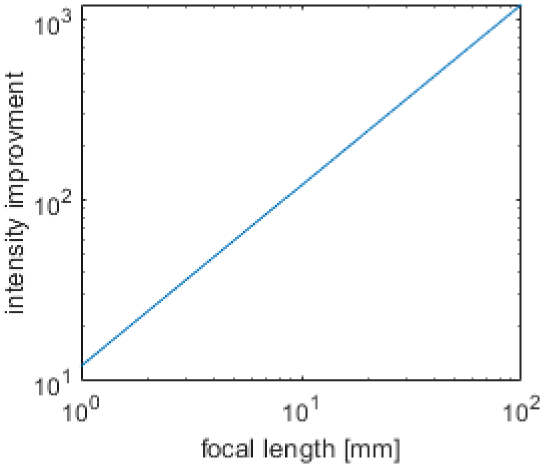

Fig. 4-2 The intensity improvement of collimation by lens with different *f*

It could be found by collimation, the intensity improvement of more than 100 could be obtained when the focal length of >10mm. However, when the lens is placed at a fixed distance to make collimation for the beam emitted in a specialized angle, if the beam is steered away, the focal length for the new beam will be changed due to the curvature variation at emission plane and the distance between the scanner and lens in emission plane is also changed. It will destroy the collimation condition as shown in Fig. 4-3 [4][5] that previously discussed for slow-light photonic crystal beam scanner.

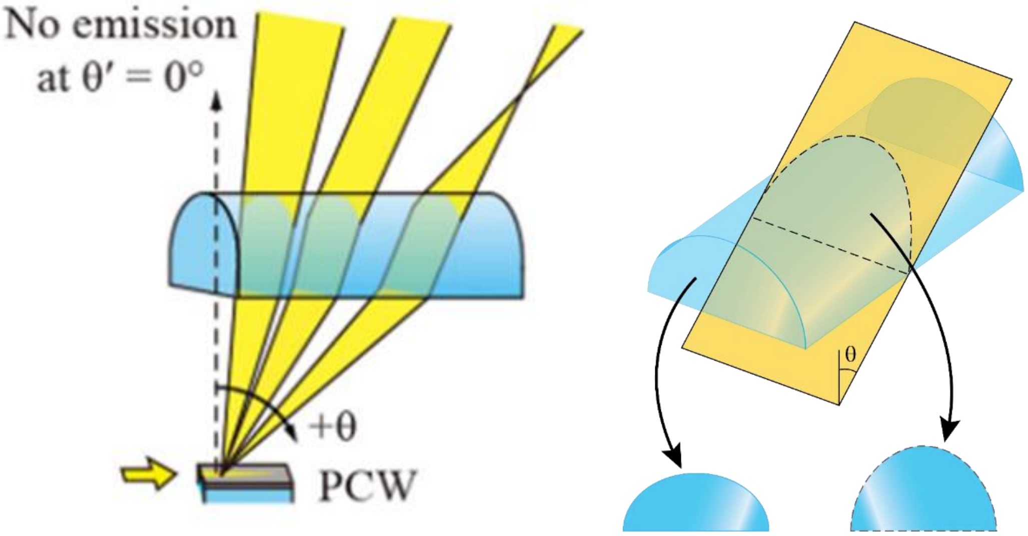

Fig. 4-3. Defocusing with beam steering [4][5]

This phenomenon limits the scanning angle of beam steering. By using a cylindrical lens with focusing length of 20mm, in around 5° steering range, the focusing condition could be maintained well. The collimation degradation will strengthen the beam intensity and power intensity variation. Sometimes, even giving up the beam steering range, the collimation condition should be maintained.

Then, the principle of 2D beam steering will be discussed. The beam steering in θ direction has been discussed before. To realize the beam steering in the ϕ direction. The focal-planed based beam scanner array should be adopted. The principle could be found in Fig. 4-4. When the beam scanner array was aligned in the ϕ direction, depending on the relative position of beam scanner element and cylindrical lens. The refraction angle though the cylindrical lens is also different. Each time, only one scanner will be operated. By switching the scanners in the array one by one, the beam steering in ϕ direction could be realized. And the beam steering space angle ϕ_{res} and total scanning range $\Delta\phi$ could be calculated as shown in Eq. 4-1 and 4-2. The resolution number is simply equal to the number of scanners integrated in the array N.

$$\phi_{res} = tan^{-1}(s/f) \tag{4-1}$$

$$\Delta\phi = tan^{-1}[(N-1)\,s/f] \tag{4-2}$$

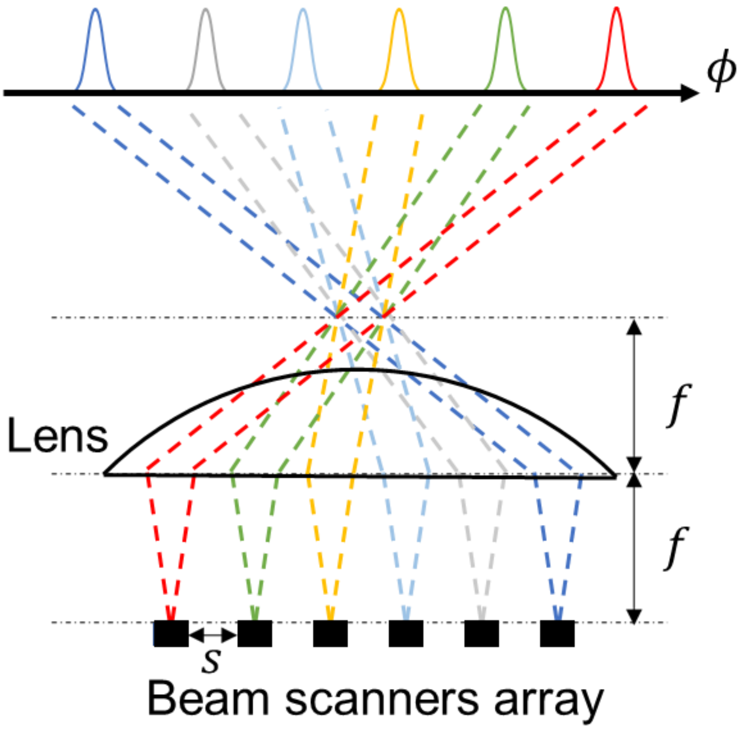

Fig. 4-4. Beam steering principle in ϕ direction

where s is the space between neighboring scanners in the array and f is the effective focal length (EFL) of cylindrical lens. It is noted that the effective focal length is not the focal length of the cylindrical lens. It is also related to the incident angle of beam in θ direction. Based on the Eq. 4-1-4-2, the $\Delta\phi$ dependence on effective focal length of cylindrical lens could be estimated assuming the s=200um as shown in Fig. 4-5. It could be used to realize the field of view of >30° by using 16, 32, 64 scanners with proper effective focal length. Another important thing is the numerical aperture (NA) of the cylindrical lens. When the EFL is small, if the total area of scanner array is large, the required NA of cylindrical lens may be impractical. For example, when the N=64, the total area of beam scanner array is 12.8mm. If EFL is 5mm, the required NA will be >1. Although it could be used to realize much larger FoV, the cylindrical lens with NA>1 is impractical unless the meta surface technology was introduced [6–8]. In this calculation the NA is assumed to be <0.5, which is a promising value for commercial manufacturing.

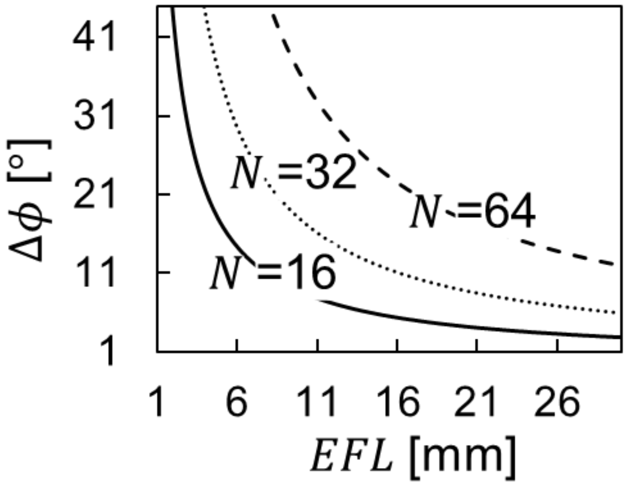

Fig. 4-5. The $\Delta\phi$ dependence on effective focal length

4.1.2 Principle of FoV and resolution enhancement of 2D beam steering

After knowing the principle of beam steering in ϕ direction. The previous discussions about FoV enhancement could be applied here. If only the beam steering range should be enhanced in θ direction, the DOE could be directly placed on the cylindrical lens. It is noted that as mentioned before the original beam steering range was limited due to the concern about collimation degradation. The DOE ③ with separation angle of 4° was chosen. It also has 10 spot. The fabrication process of 10-spot DOE is not absolutely same as odd number spot DOE. The 21 order grating should be firstly considered to design the pitch size Λ as Eq. 4-3. And then the odd orders will be suppressed by microstructure within the pitch.

$$\Lambda = \frac{\lambda}{\sin{(\theta_s/2)}} \tag{4-3}$$

The DOE could be directly stacked on the cylindrical lens cooperated with the prism mirrors mentioned in the previous section to make the beam cover the vertical direction as shown in Fig. 4-6. Also, the counter propagation integration could be applied here to make the FoV double. However, for the 2D beam steering devices, to make the beam steering in ϕ direction of counter-propagation in the same angle. The counter-propagation should be aligned side by side as shown in Fig. 4-6. From the font view, it is absolutely same as previous 1D beam steering, while form the side view it will be like the Fig. 4-4.

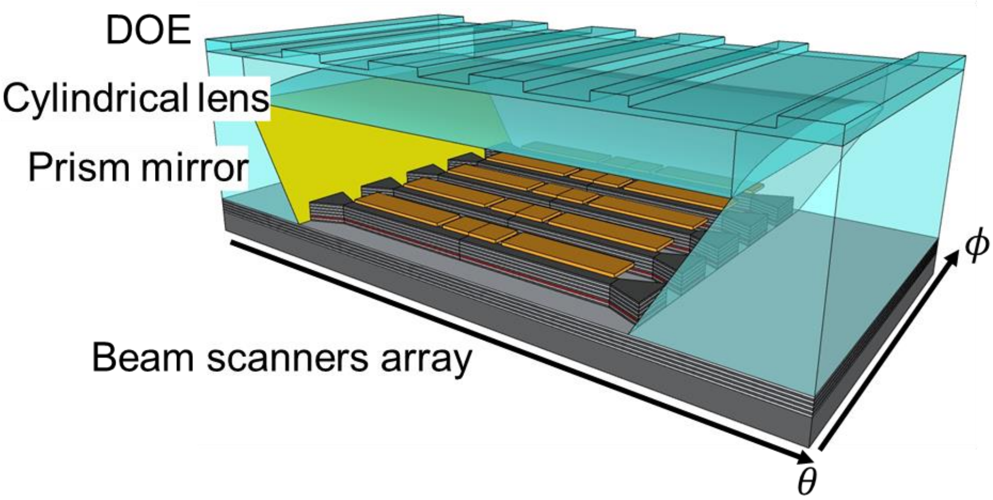

Fig. 4-6 Schematic of 2D beam steering

To evaluate the possibility of the system, the ray-tracing simulation was completed in Zemax. To simulate the system in Zemax, the system shown in Fig. 4-7 was established to simulate the real system, where the light source was assumed to an angular light source with emission area of 2mm×3μm and original beam scanning range of θ'=50°~54°. The light source has the beam divergence in both directions of $\delta\theta = 0°$, $\delta\phi$=10°. The prism mirror was replaced by a planar reflector with full reflectivity. The cylindrical lens was assumed to be a commercial lens that was produced by Thorlabs AYL2520-B. The DOE was performed by the diffractive grating with beam splitting.

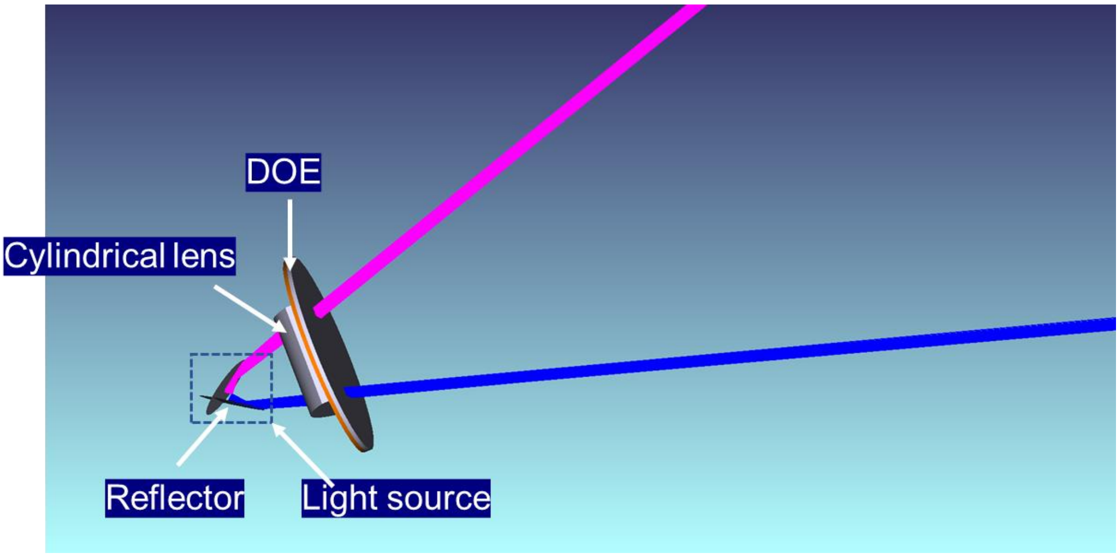

Fig. 4-7 The system simulated in Zemax

Firstly, the collimation condition should be confirmed without DOE, where the counter-propagation scanner was assumed, and cylindrical lens and prism mirror was equipped as the sub system shown in Fig. 4-8 (reflector is not shown in the figure, but in the simulation, it was added). The simulated result was shown in Fig. 4-9. In the simulation, the beam steering was assumed to be 5 steps from 50°~54°. After reflection by the reflector and collimation by the cylindrical lens, the FFP was shown in Fig. 4-9. It could be found that the beam could be well collimated by the lens in the entire beam steering range of 4°.

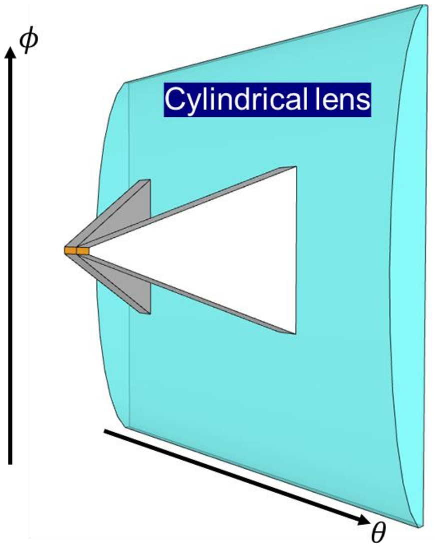

Fig. 4-8 System used to simulate the collimation of a cylindrical lens

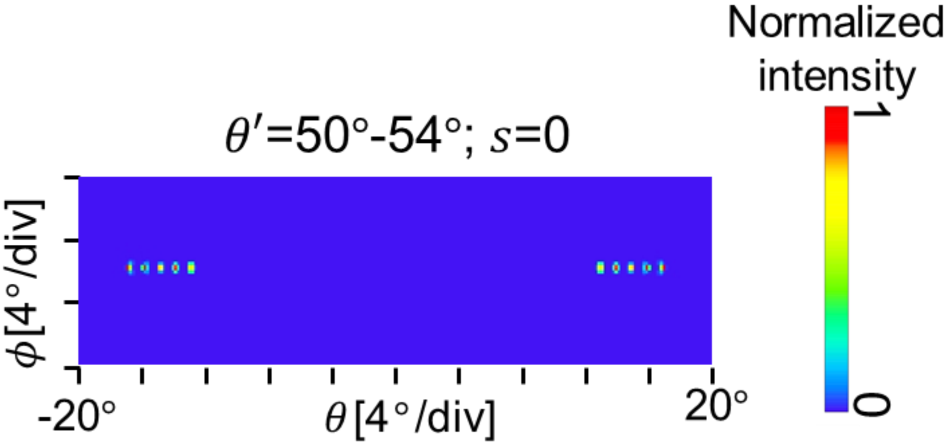

Fig. 4-9 Simulated FFP of collimation of beam steering range

The DOE was simply added on the cylindrical lens. The DOE was assumed as near as possible to the real DOE. It is a 10-spot diffractive beam splitter with separation angle of around 4°. It is noted that the detailed intensity variation due to the microstructure in the DOE pitch could not be simulated in the simulation. The system was shown in Fig. 4-10 and the simulation result could be found in Fig. 4-11. The assumption of light source is absolutely same as previous simulation. It could be found that the FoV could be enhanced to 70° with good collimation condition.

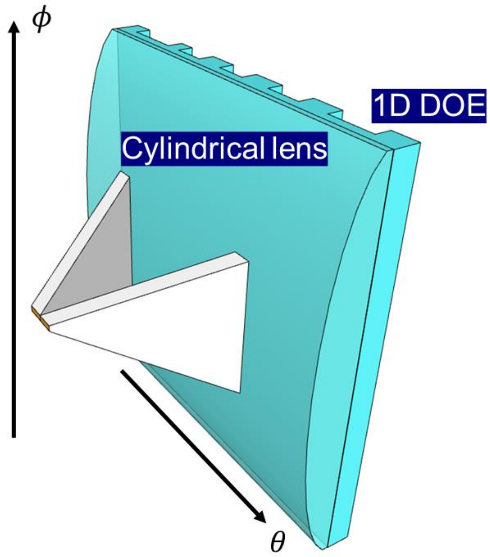

Fig. 4-10 System used to simulate the FoV enhancement of a cylindrical lens

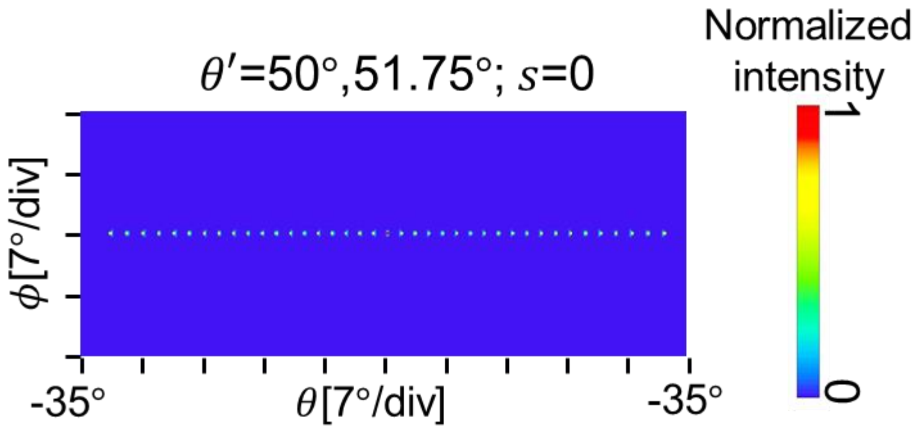

Fig. 4-11 Simulated FFP of collimation of beam steering range

Then the overlapped 2D beam steering availability was simulated. In the simulation a 10-scanner counter-propagation scanner array was simulated as shown in Fig. 4-12, where the space between two neighboring elements is 0.5mm, because in the real fabrication the 0.5mm was chosen. The Simulation result was shown in Fig. 4-13, the FoV in the ϕ direction is around 15°, which is consistent with the result calculated by Eq. 4-2. And the collimation condition could be greatly maintained in the whole beam steering range. At around θ=0°, the beam from counter-propagation beam scanners are overlapped to indicate the vertical direction was covered.

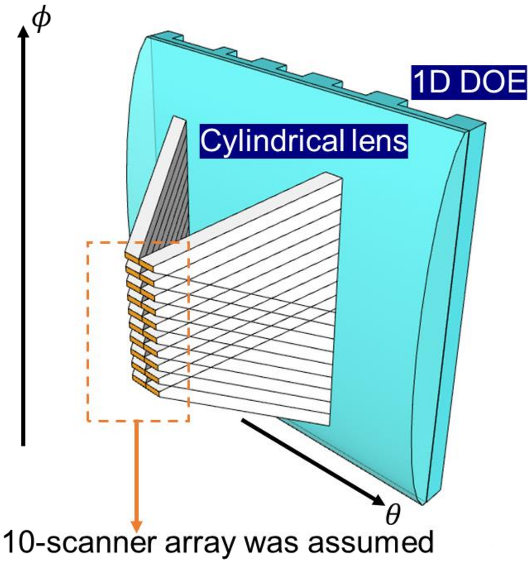

Fig. 4-12 System used to simulate 2D beam steering

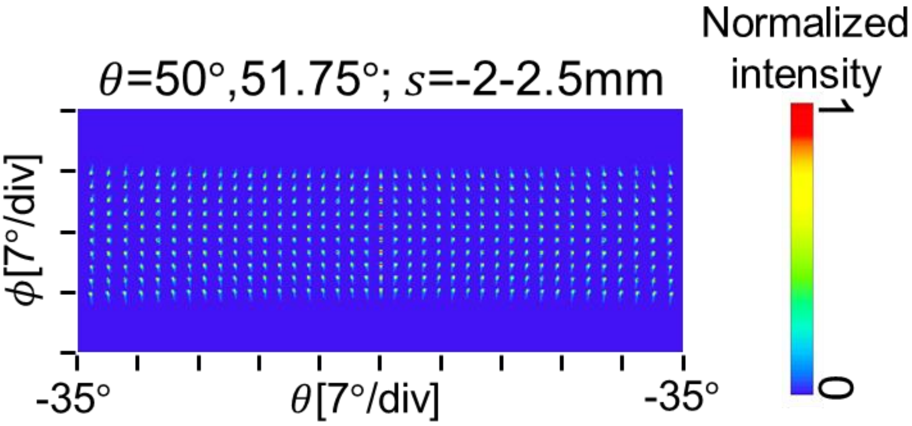

Fig. 4-13 Simulated FFP of collimation of 2D beam steering

The FoV and resolution enhancement in the ϕ direction $\Delta\phi$ is also very important. Although from Eq. 4-2 it could be known that the $\Delta\phi$ could be increased by shortening the EFL and increasing the number of beam scanners in the array, the EFL is limited by the module height that discussed previously because the focal length could not be smaller than the height of prism mirrors. Another concern is difficulties in integration of more beam scanners. 64 scanners integration in the array is already difficult and will greatly decrease the yield. The method of using smaller number of scanners to realize enough resolution is very important. Considering the FoV and resolution enhancement of 1D beam steering in θ direction, the enhancement in ϕ direction by using DOE is also possible as shown in Fig. 4-14, where the different color indicates light from different scanner.

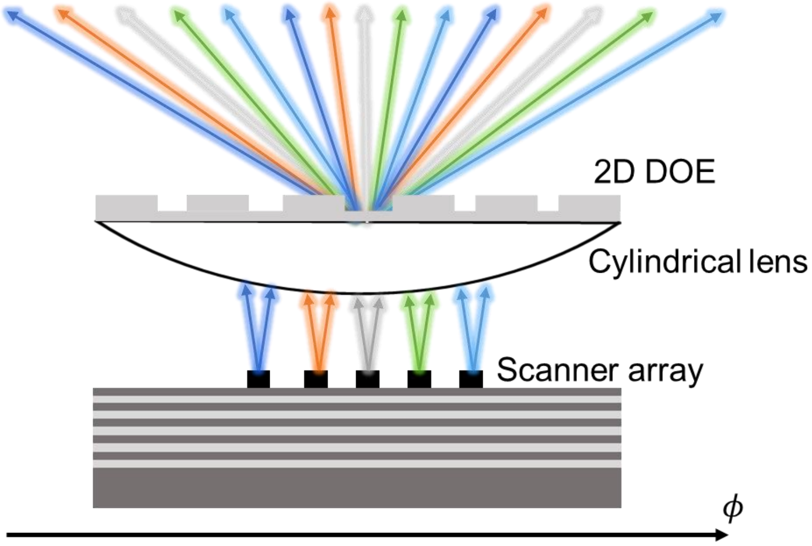

Fig. 4-14 The schematic of extending FoV in ϕ direction

In this case the 2D DOE with micro structured in two direction could be introduced. The availability of using 2D DOE to enhance the FoV and resolution of 2D beam scanning was also simulated by establishing the system shown in Fig. 4-15. Thanks to the enhancement of FoV and resolution in ϕ direction, 10-scanner array may not be required. Here a 6-scanner array with space of 0.5mm was assumed to illustrate the function. Here, 10×7 DOE with separation angle of 4°×6° was assumed. In this simulation the observation plane was assumed as a *x-y* domain plane while in the previous simulation as an angular space plane, because in the experiment we used free-space measurement for

2D beam steering with 2D DOE.

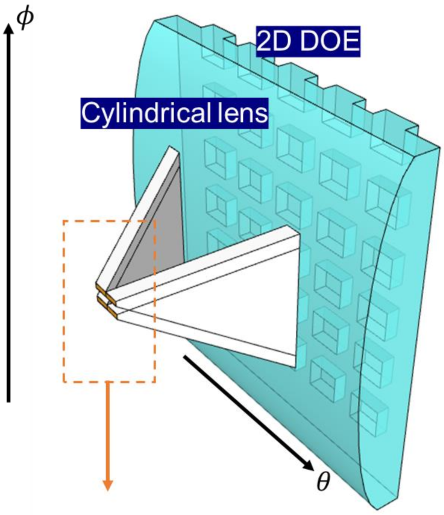

Fig. 4-15 System to simulate 2D beam steering with 2D DOE

The simulation result was shown in Fig. 4-16. It shows the result that the 2D beam steering range was enhanced to 68° × 45° by using only 6 scanners and the cylindrical length with EFL of about 20mm. At the same time, the resolution in ϕ direction is also increased to 42.

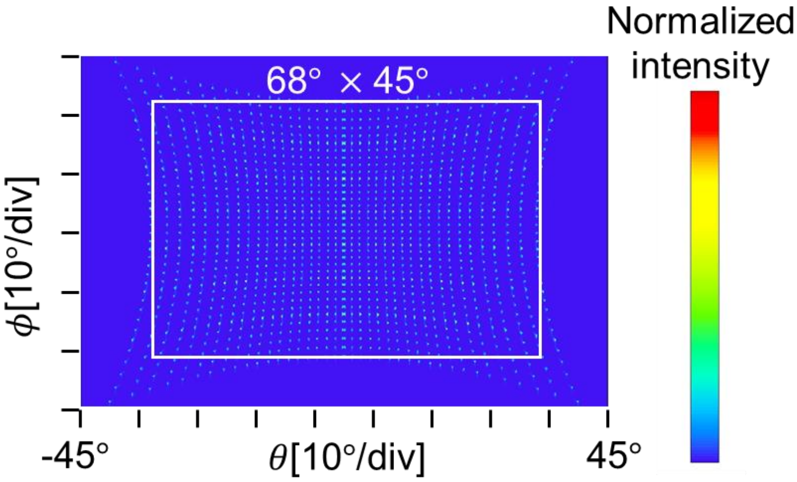

Fig. 4-16 Simulated FFP of 2D beam steering with using a 2D DOE

4.2 Experimental result of 2D beam steering with enhanced

FoV/resolution enhancement

4.2.1 2D beam steering with 1D FoV and resolution enhancement

The measurement setup of 2D beam steering is shown in Fig. 4-17 and the photo of fabricated device was also shown in Fig. 4-18. Al though more than 20-scanner array was fabricated, considering the continuous well-worked devices, only 5-scanner array were selected. The space between scanners are 0.5mm and the length of scanner and slow-light VCSEL are 2mm and 0.5mm respectively. As the previous 1D beam scanning, the prism mirror was put on the chip. Between the 10-spot DOE and prism mirror, a cylindrical lens was inserted. The prism mirror could be redesigned to support the cylindrical lens. The DOE could be placed on the planar plane of a convex-Plano cylindrical lens.

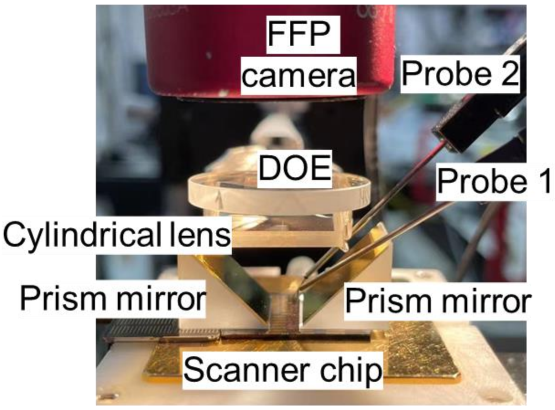

Fig. 4-17 Measurement setup of 2D beam steering

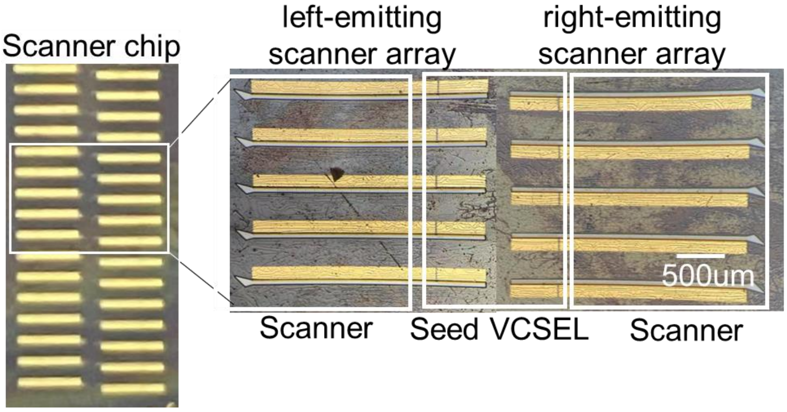

Fig. 4-18 Top-view photo of beam scanner array

Firstly, the measured FFP when the I_{VCSEL} steered from 60mA to 210mA without DOE is shown in Fig. 4-19. The cylindrical lens was inserted and was placed at the position to get the best collimation condition though the whole beam steering range. The FoV in θ direction $\Delta\theta$ is about 4° and the collimation condition could be also witnessed from the FFP. After collimation the beam divergence in both directions was expanded to 0.12° in θ direction and collimated to 0.1° in ϕ direction. The $\delta\theta$ was expanded due to the abbreviation of cylindrical lens. It may reduce the resolution in θ direction N_θ to around 40 but still enough to applications after adding the DOE. The comparison of collimated spot beam and fan beam was also demonstrated as shown in Fig. 4-20. The two figures were captured when the cylindrical lens is added and not added. The left figure is for collimated spot with cylindrical lens and the observation filter is 0.01%. The observed intensity is about 980 units. The right figure shows the FFP directly captured by the camera without any optics. The beam was observed when the filter is 0.25%. It could be obtained that the intensity of a spot beam could be 160 times as large as that of fan beam. If a 10-spot DOE is inserted, the intensity may be reduced to 1/10, but still 16 times improvement of intensity could be obtained.

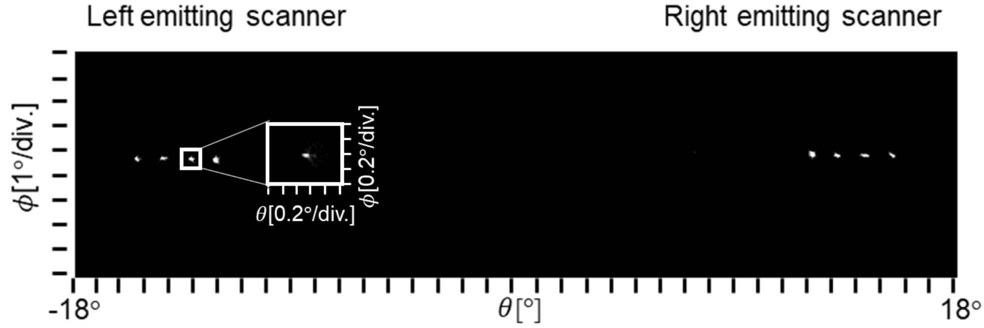

Fig. 4-19 Collimation condition of beam scanner by a cylindrical lens

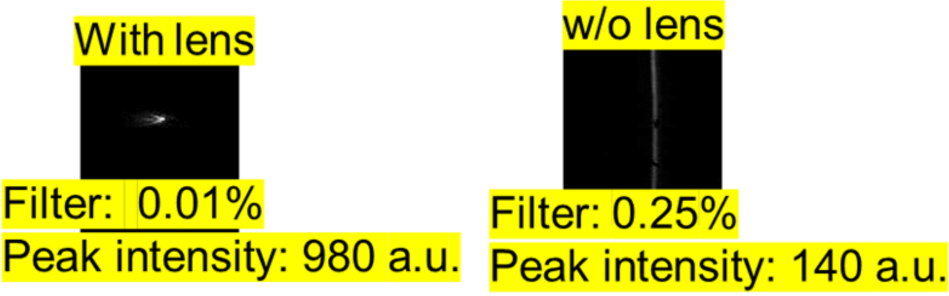

Fig. 4-20 Comparison between collimated beam and fan beam

The FFP after adding a DOE was shown in top figure Fig. 4-20 for static I_{VCSEL} and in bottom figure for scanned I_{VCSEL}. The single spot was split to 10 spots with separation of about 3.5°, when the static I_{VCSEL}= 192mA and 183mA for left- and right-emitting beam scanners. Then by tuning the I_{VCSEL} to 70mA and 60mA, the overlapped beam covering all the separation could observed. It indicates the total FoV $\Delta\theta$ of 64° and the N_{θ} of around 450. Then the 2D beam steering measurement will be carried out by using the scanner array. To show the potential for the beam scanner, although only 5 scanners were fabricated, by moving the cylindrical lens laterally, the 15 virtual beam scanners were formed. Because the cylindrical lens was moved, the relative position of beam scanner and cylindrical lens will also be changed. Although the position of beam scanner is not changed, the light from beam scanner will be diffracted to the other direction. It is same to move the beam scanner chip to form the virtual beam scanner.

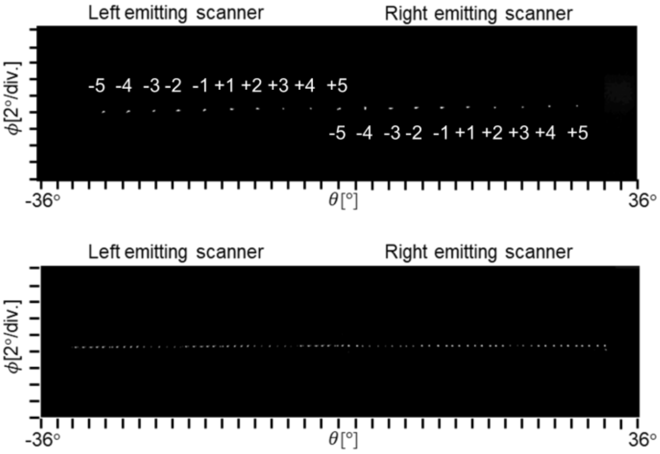

Fig 4-20 The 1D spot beam steering by cylindrical lens and DOE

The overlapped FFP of 20-scanner array 2D beam steering is shown in Fig. 4-21. It could be seen that the whole FoV $\Delta\theta \times \Delta\phi$ of 64° × 14° was covered by switching the 20 scanner (5 real scanners + 15 virtual scanners)in the array. The beam divergence was also measured for the measured spots as shown in the bottom figure of Fig 4-21. The average beam divergence was around 0.14° × 0.1° ($\delta\theta \times \delta\phi$). It indicates the resolution points number of 450 in θ direction and 20 in ϕ direction. That is to say the totally resolution points number could be >9,000. The zoomed figure shows one of the spot, it could be seen that the collimation was well obtained. However, through the who beam steering range, quality of some spots is poor. It may result from the performance variation of different beam scanner and different operation current. Also, the limited aperture of FFP camera may also have effect to the observed FFP. The stage vibration will also affect the performance of the beam scanner under direct contact current injection. The wire and die bonding process may improve the vibration. Although in this experiment, only 5 real scanners were used, thanks to the good integrability of VCSELs, it is easy to fabricate more devices by better fabrication process and thus improve the resolution in ϕ direction.

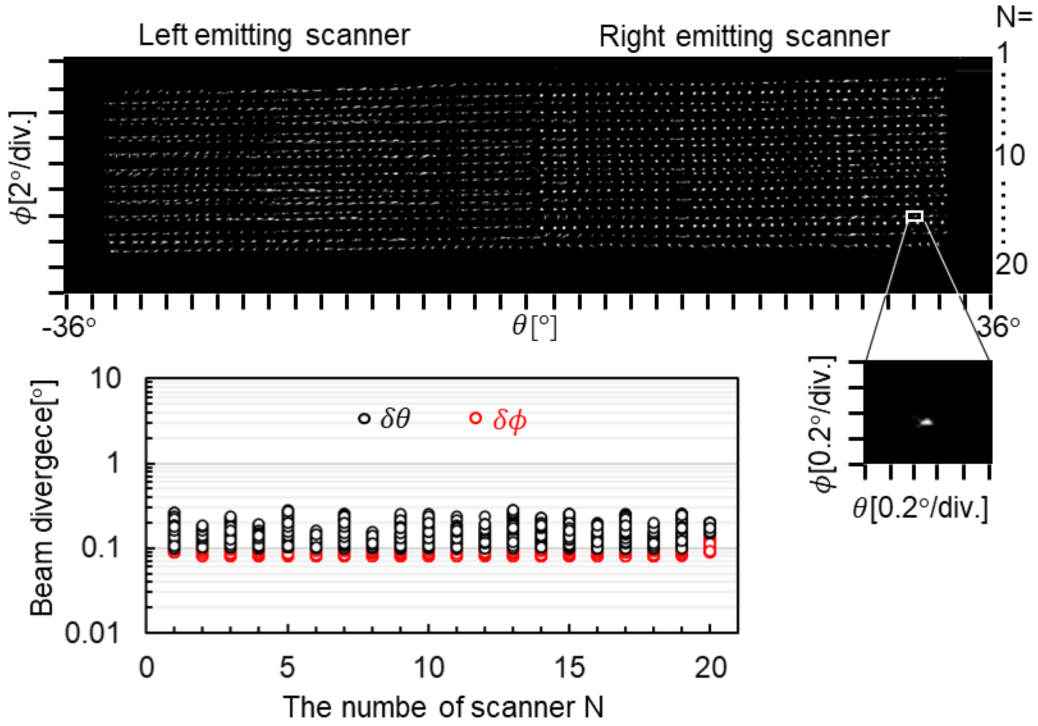

Fig 4-21 2D beam steering and beam divergence measurement

4.2.2 2D beam steering with 2D FoV/resolution enhancement

Differed from the separated counter-propagation proposed in the previous section. Recently, the waveguide-shared counter-propagation-switchable beam scanner was proposed and fabricated. The schematic was shown in Fig. 4-22. Most of things are similar to the separated counter-propagation scanner including two slow-light laser and operation function. The important difference is the light from two slow-light laser will be coupled to the same slow-light waveguide in the opposite direction. It will lead to counter-propagation of light by switching the operation slow-light VCSEL. The design of slow-light VCSEL and waveguide are same as previous section. The fabrication process is also same, where the length for slow-light VCSEL and VCSEL beam scanner are still 0.5mm and 2mm. The merit of this device is firstly smaller device size. The chip size could be half of separate counter-propagation beam scanners. Another thing is the yield, when the processed area is getting smaller, the yield will also be increased correspondingly.

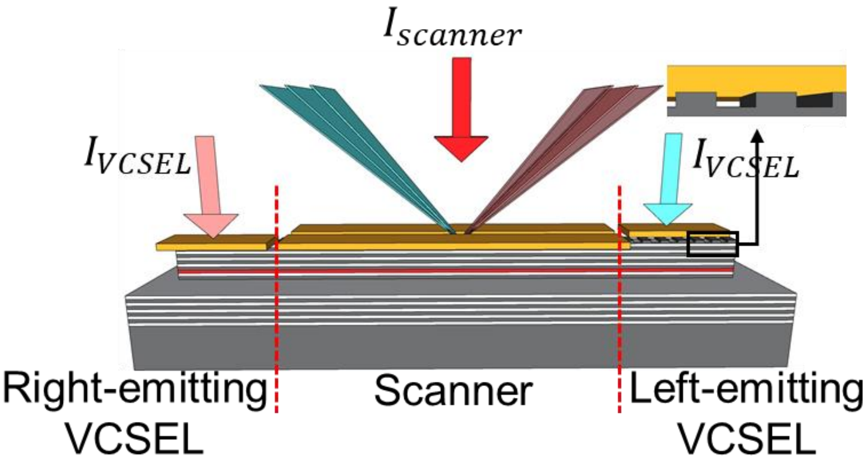

Fig 4-22 Schematic of waveguide-shared counter-propagation-switchable beam scanner

To realize the 2D beam steering, 6-scanner array was also fabricated as demonstrated in Fig. 4-23 and the top-view photo of device is shown in Fig. 4-24. The scanners were fabricated with space of 0.5mm. Despite the waveguide-shared devices, the slow-light laser-shared devices could also be fabricated as shown in Fig. 4-25.

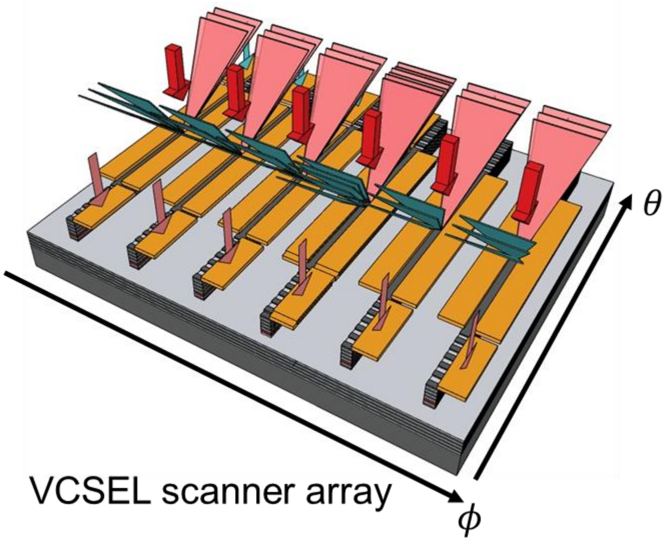

Fig. 4-23 The schematic of waveguide-shared beam scanner array

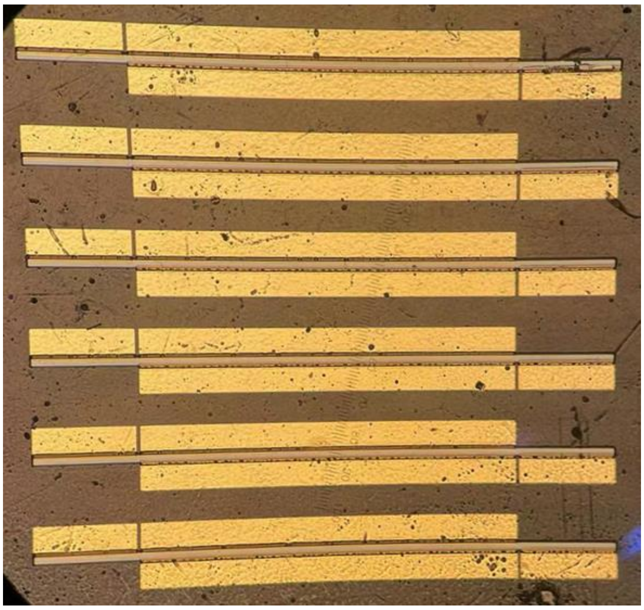

Fig. 4-24 The top-view photo of waveguide-shared beam scanner array

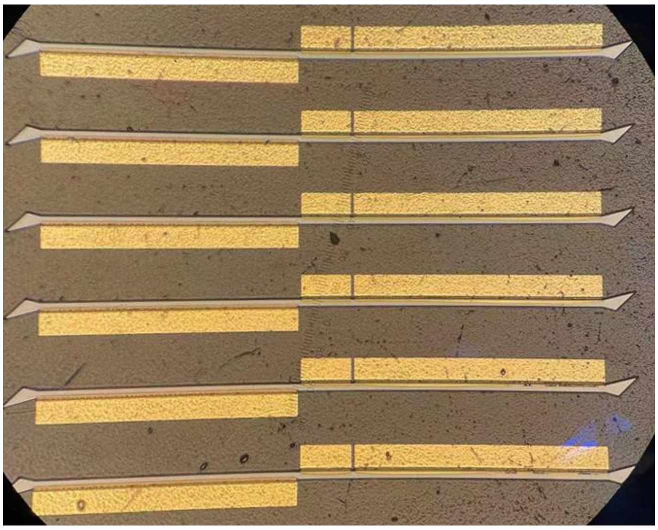

Fig. 4-25 The top-view photo of VCSEL-shared beam scanner array

The merit of VCSEL-shared beam scanner is the smaller area of slow-light laser. Because only half region of previous double slow-light VCSEL devices need to be EB lithographed, the cost could be better. In this experiment, only the waveguide-shared devices were measured. The schematic of waveguide-shared scanner array assisting with lens and DOE was shown in Fig. 4-26. The basic principle and structure are almost same as separate counter-propagation beam scanner.

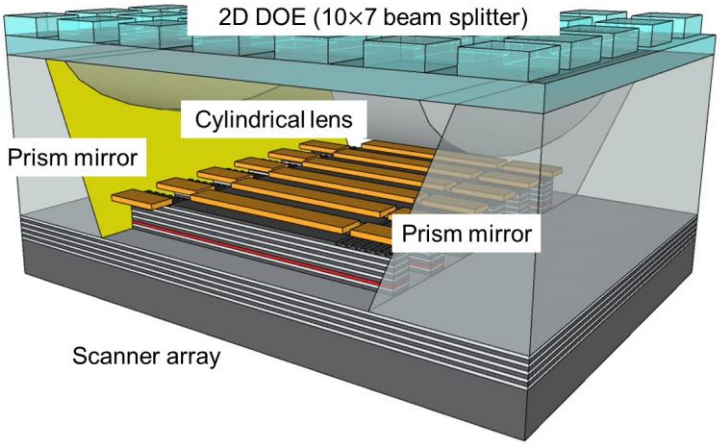

Fig. 4-26 The schematic of 2D beam steering system

Then the 2D beam steering measurement will be carried out. When switching the scanners in the array, the NFP could be observed as shown in Fig. 4-27, where the right-emitting scanner in the second scanner and left emitting scanner in the sixth scanner were operated. The other scanners could be operated by same method. This NFP was captured at the vertical direction by the camera to capture the light from counter-propagation scanners. Actually, the main emission direction, as mentioned before, is in the right or left direction. By observing the NFP from proper emission direction the clear slow-light mode could be observed as NFP shown in Chapter 2.

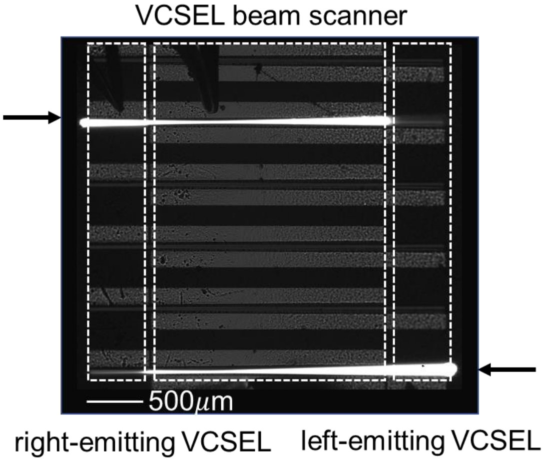

Fig. 4-27 NFP of switching the scanners in the array

Because the scanner array consists of 6 scanners with a spacing of 500μm, so the chip size is as small as <3mm×3mm. By adding a same cylindrical lens with previous experiment and 2D DOE of 10×7 spots with separation angle of 6° × 4° , the far field pattern (FFP) reflected by a flat target were measured. The static FFP was shown in Fig. 4-28 when the fixed I_{VCSEL}=50mA and $I_{scanner}$=200mA were injected to the counter-propagation seed VCSELs and the scanner, respectively. The FFP was measured by free space. It means the emission light will be reflected by a flat diffuser and then received by a conventional infrared CMOS camera. Why the previous FFP analyzer is not used anymore is that the aperture of FFP camera is so small to capture all the light when beam steering. In Fig. 4-28, it could be found 10×7 spot beams with a narrow beam divergence of below 0.1° were obtained. By tuning I_{VCSEL} from 50mA to 210mA and switching 6 scanners one by one, the 2D beam scanning field of view of > 70° × 45° were witnessed in Fig. 4-29. The details of beam divergence in a single order could be measured by a FFP analyzing camera as shown in the zoomed figure. The average beam divergence of all beams in this order is <0.1° × 0.12°. The beam divergence in different orders will be in the same scale, so the number of total resolution points reached > 33,000 (800×42)

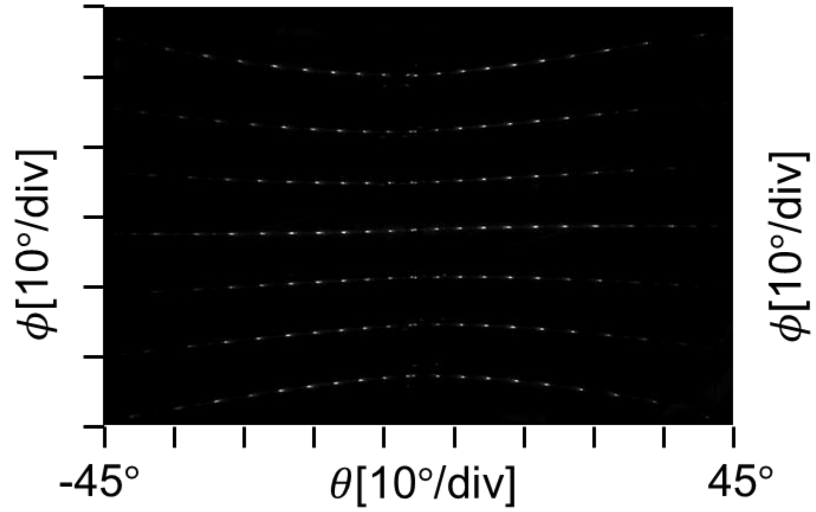

Fig. 4-28 Static FFP of beam scanner with 2D DOE

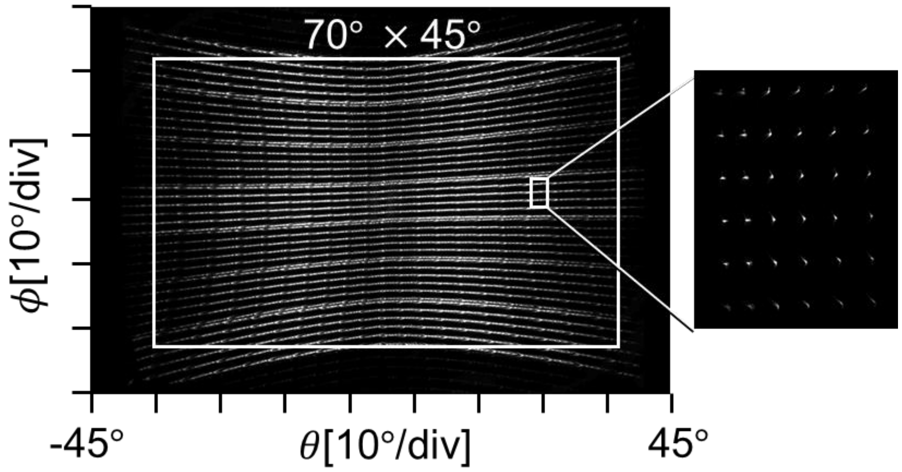

Fig. 4-29 Overlapped FFP of 2D beam steering when beam steering

Reference in Chapter 4

4-1. H. Abe, M. Takeuchi, G. Takeuchi, H. Ito, T. Yokokawa, K. Kondo, Y. Furukado, and T. Baba, "Two-dimensional beam-steering device using a doubly periodic Si photonic-crystal waveguide," Opt. Express **26**(8), 9389 (2018).

4-2. K. Kondo, X. Gu, Z. Ho, A. Matsutani, and F. Koyama, "Two-Dimensional Beam Steering Using Slow-Light Waveguide Deflector Array with Optical Gain," in *Conference on Lasers and Electro-Optics* (Optical Society of America, 2018), p. SM3I.4.

4-3. K. Kondo, X. Gu, Z. Ho, A. Matsutani, and F. Koyama, "Two-Dimensional Beam Steering Device Based on VCSEL Slow-Light Waveguide Array with Amplifier Function," in *2019 Optical Fiber Communications Conference and Exhibition (OFC)* (2019), pp. 1–3.

4-4. J. Maeda, D. Akiyama, H. Ito, H. Abe, and T. Baba, "Prism lens for beam collimation in a silicon photonic crystal beam-steering device," Opt. Lett. **44**(23), 5780 (2019).

4-5. "Concept of LiDAR Device Using Slow-Light Beam Steering Device 3 . Calculation of Raging Precision," 1–8 (2017).

4-6. Z. Bin Fan, Z. K. Shao, M. Y. Xie, X. N. Pang, W. S. Ruan, F. L. Zhao, Y. J. Chen, S. Y. Yu, and J. W. Dong, "Silicon nitride metalenses for unpolarized high-NA visible imaging," 2018 Conf. Lasers Electro-Optics, CLEO 2018 - Proc. 2–3 (2018).

4-7. M. Khorasaninejad, W. T. Chen, R. C. Devlin, J. Oh, A. Y. Zhu, and F. Capasso, "Metalenses at visible wavelengths: Diffraction-limited focusing and subwavelength resolution imaging," Science (80-.). **352**(6290), 1190–1194 (2016).

4-8. J. Engelberg and U. Levy, "The advantages of metalenses over diffractive lenses," Nat. Commun. **11**(1), 9–12 (2020).

.

Chapter 5

3D sensing applications using VCSEL beam scanner

In this chapter, primary application of VCSEL beam scanner in 3D sensing including structured-light sensing and LiDAR will be demonstrated. The advantages of VCSEL beam scanner in real application will be also discussed.

5.1 Application of VCSEL beam scanner in structured-light sensing.

5.1.1 Principle of structured-light sensing based on VCSEL beam scanner

Structured-light sensing is a kind of high-accuracy 3D sensing technology for short-range application mainly shape modelling, for example face identification [1 – 3]. The schematic of structured-light sensing based on VCSEL beam scanner was shown in Fig. 5-1 for a spheric object. It was composed of a beam scanner, a CMOS sensor, and a target. The controlling and synchronization system is also needed, but they were not shown in this figure. It could be seen that if the fan beam generated by the bean scanner is illuminated to an objected with depth fluctuations, the beam disparity will be found in the imaging plane of CMOS sensor. The disparity corresponds to the shape of the target. Based on the disparity received by the camera, the shape and depth information could be obtained. In our experiment, for simplicity of the experimental system, algorithms and analyzing method. A step object used in Fig. 5-2 was formed by two board sticking, where the former board has thickness of about 3mm. The two boards has similar reflectivity of larger than 90%. As shown in Fig. 5-2, when measuring the target depth, a reference plane should be set for obtaining a referred image when illuminating a planar object at know distance for calibration. The detailed depth obtaining principle could be found in the image received by the camera shown in Fig. 5-2.

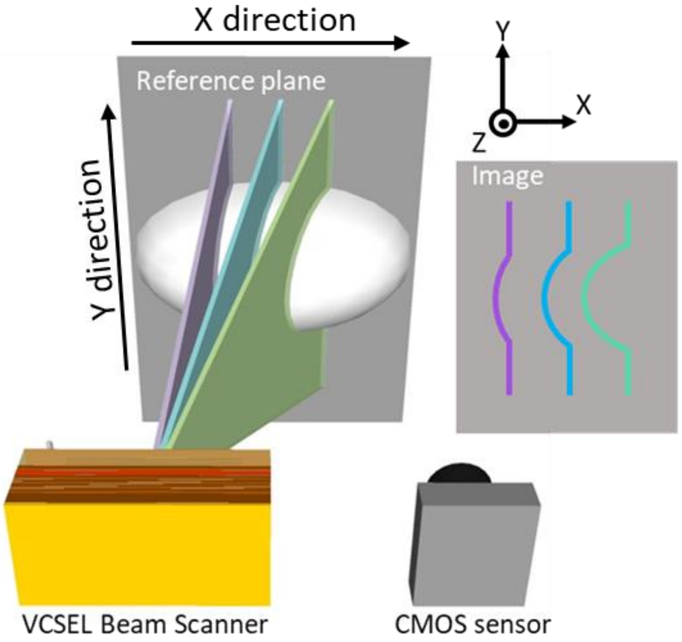

Fig. 5-1 The schematic of structured-light sensing based on the VCSEL beam scanner

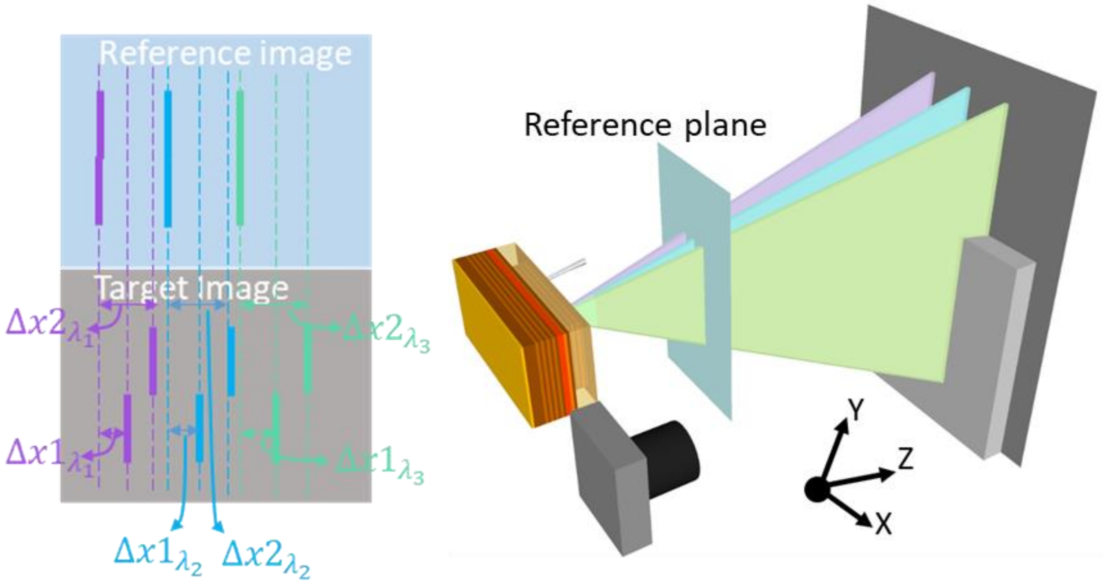

Fig. 5-2 The schematic of structured-light sensing in the experiment

The calculation method could be found in the top-view figure of schematic (From *y* axis) shown in Fig. 5-3. The reference plane could placed in front of or behind the object, but it is needed to set the reference plane near to the target depth to get high absolute measurement accuracy due to suppression of symmetrical error. The reference could be set away from the target depth if the calibration that will be shown later could be finished covering the target depth.

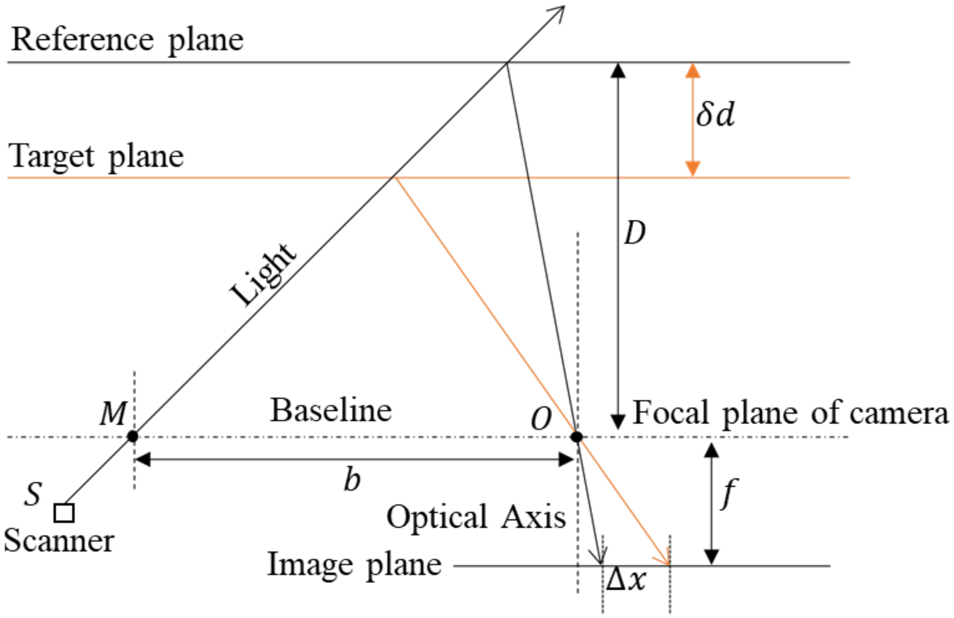

Fig. 5-3 The top-view of the structured-light sensing system

In this figure, the distance between the scanner and camera is *b*, the focal length of camera is *f*, the distance between reference plane is *D*, the target depth between reference plane and target plane is δd. It could be found that for the target plane at different depth, the Δx on the focal plane of camera will be different, so the depth could be obtained by Δx and calibrated parameters of *b, f, D.* as the following Eq. 5-1 [4],

$$\delta d = \frac{\Delta x D^2}{fb \pm \Delta x D} \tag{5-1}$$

where although the d is not the absolute distance in the world coordinates of camera. It is enough to plot the curve of target shape, which is enough for real applications. The calibration method shown in Fig. 5-4 will be used to estimate the parameter *b, f, D.*

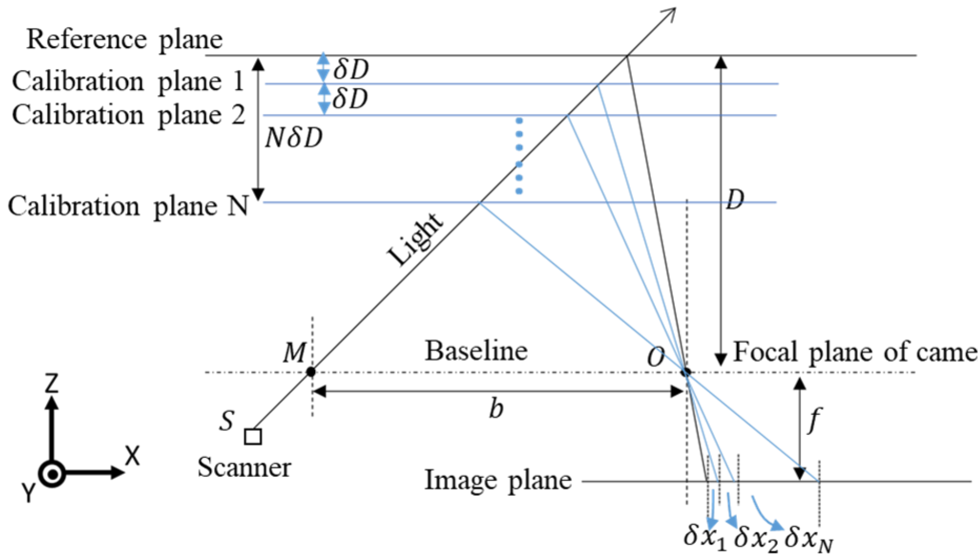

Fig. 5-4 The calibration method of parameter of *b, f, D.*

The parameter could be estimated by moving the reference plane from the original depth D away or closer to the baseline (Line between scanner and camera) by step of δD and measuring the disparity of received fan beam in the imaging plane of camera δx as Eq. 5-2,

$$\frac{1}{N\delta D} = \frac{1}{\delta x_N} \cdot \frac{fb}{D^2} + \frac{1}{D} \tag{5-2}$$

where it could be easily found that $\frac{1}{N\delta D}$ has linear relation with $\frac{1}{\delta x_N}$. By plotting the curve of $\frac{1}{N\delta D} - \frac{1}{\delta x_N}$, fb and D could be estimated by regression model. However, there might be some systematic error due to the factors including, unprecise reference plane moving although we have used a precise motor with moving accuracy of 1um, unprecise δx due to the photon noise, the system placement error for example the base line is not parallel to the reference plane and the beam scanning direction is not critically parallel to the baseline and so on. It could be corrected by the error correction calibration, especially correction in the target depth. The error correction method is as following: 1) reducing the δD to 1mm and move the reference plane step by step; 2) measuring the depth δd

by previously calibrated f, b,D; 3) Plot the scattering figure of $\delta d - N\delta D$ and make the regression training. Each time in the real measurement, the measured depth δd should be transferred to this curve to do correction. All the calibration and reference plane were used before normal measurement. In the real application, it could be finished at manufactory procedure. When it goes to users’ hand, no calibration and reference plane are needed.

5.1.2 Off-line structured-light sensing based on VCSEL beam scanner

The measurement based on Fig. 5-2 was demonstrated. The Fig. 5-5 (a) and (b) are the front-view photo and side-view photo of the target respectively. As shown in the figure, the measured target, which is placed 35cm away the camera (Imperx C4080), is composed of two parts - a Kodak grey card and a Post-Mountable White Polystyrene Viewing Screen (with thickness of 3mm) that is tightly attached to the Kodak card. In the measurement, the exposure time of camera was set to 5ms and current of 120mA was injected to a 2mm device with 3mW coupled light, which brought output power of 15mW.

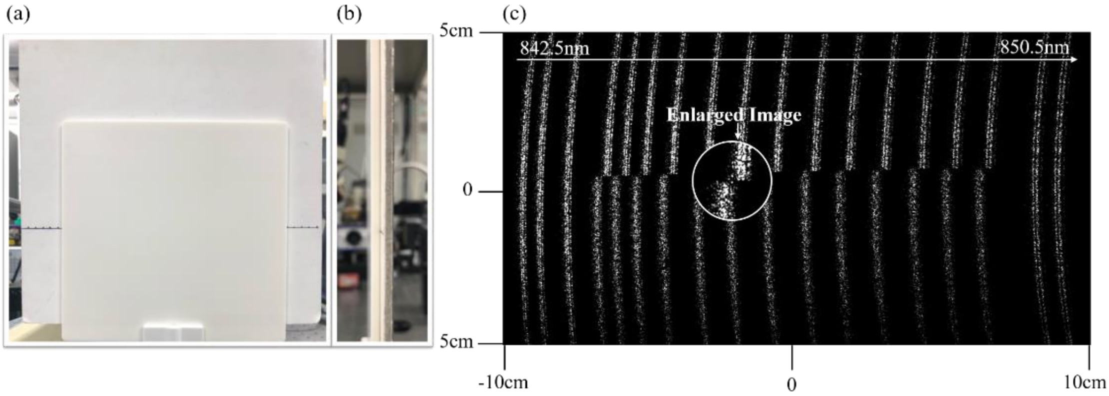

Fig. 5-5. (a) The front-view photo of target (b) the side-view photo of target (c) the image of received pattern reflected by the target

In the experiment, we varied the wavelength of input light from 842.5nm to 850.5nm by 18 times, which projected the output beam covering a range of 20cm (30°) ×10cm

(16°) at 35cm away from camera. The beam width in the received pattern is about 2mm (0.32°) that is much beyond the result shown in FFP of Fig. 5-5 due to limit of device size. Though we only steered the beam for 18 times, the number of potential resolution points could reach 100 points (20cm/2mm), if steering the beam continuously.

The projected beam of beam scanner would bends as shown in Fig. 5-5 (c). Through the way beam bends, we could obtain the 3D information of target as Fig. 5-6 (a) shows. A distinct bound of the front plane and behind plane could be observed in this figure. From Fig. 5-6 (b), the profile of depth could be clearly seen. The slight fluctuation of the depth could also be observed due to noise.

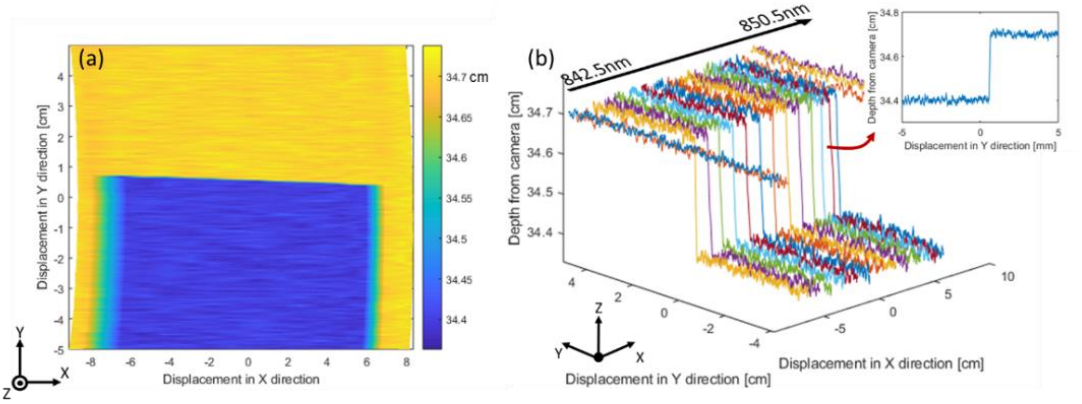

Fig. 5-6. (a) Depth image of target (b) Depth profile of target

The depth measurement of the same target placed 4.7m away from a CMOS camera is demonstrated. In the experiment, we chose a 2mm-beam-scanner device with injected current of 200mA that make the output power of beam scanner 60mW and used an acA1300-75gm camera with an exposure time of 1ms, focal length of 50mm and pixel size of 4.8 μm. Firstly, the target was placed at 4.7m away from the CMOS sensor and then moved 30cm farther from the CMOS camera using a Thorlabs electronic stage with a moving accuracy of 5 m as in Fig 5-7 (a). The reflected stripe beams of the target placed at 4.7m and 5m are obtained as shown in Fig. 5-7 with a beam width of 11.2 mm.

We could see a slight displacement of them as discussed in the last section. Then we scanned the stripe beam by changing the wavelength of an input light from 844.5nm to 845.0nm, which covers a detected range about 14.9cm×14cm, but despite field of view of the camera, the beam could steer a much larger range of 1.3 m×2.6 m at 5m away from the beam scanner, which also corresponds 200 lateral resolution points.

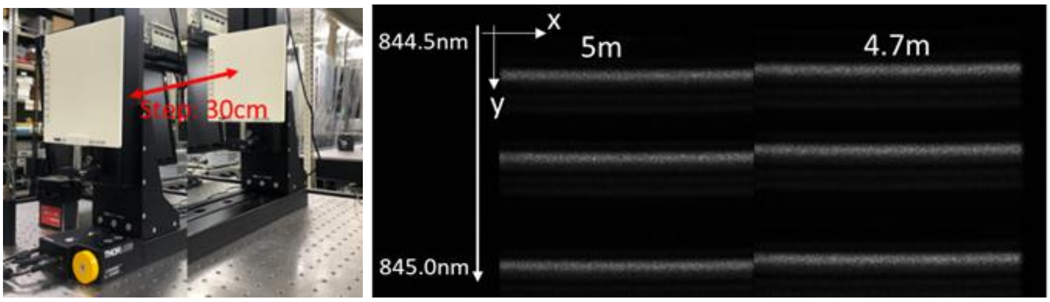

Fig. 5-7. (a) The target placed at about 4.7m and 5m (b)Received pattern reflected by the target placed at 5m and 4.7m

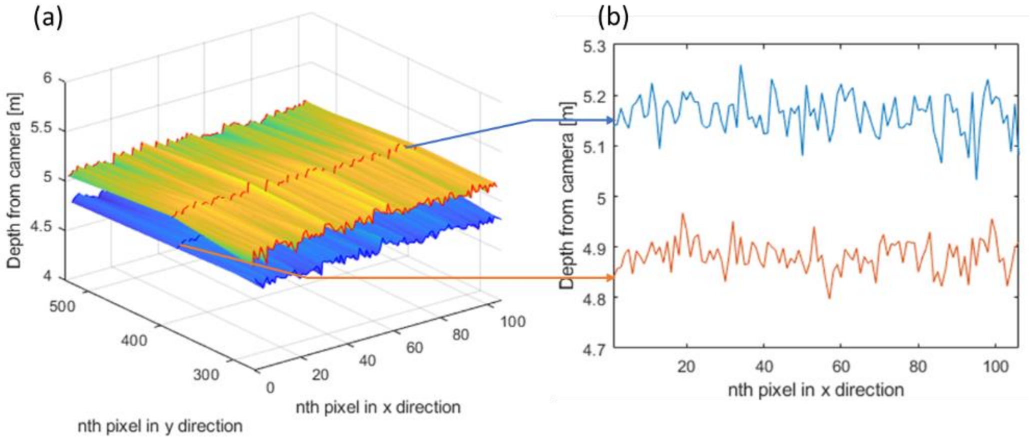

Fig. 5-8 (a) Depth mapping of target (b) depth profile of one-strip measurement

About the depth accuracy. Firstly, we need to clearly define the accuracy in our analysis. There are two kinds of accuracy in mathematical analysis, displacement error that reflects the absolute difference between real value and measured value, and wobbling error (Standard deviation) that evaluates the stabilities of measurement. We will focus on the wobbling error of measurements because when the threshold is higher than $\overline{N_B} + 3\sigma_B$, the displacement error will be much smaller than wobbling error, where $\overline{N_B}$ is the average of background light in received images, σ_B is the standard deviation of background light.

To evaluate the accuracy of sensing, we summarize the procedures to obtain the depth data of target (as shown in Fig. 5-9) and find the factors in the process that is likely to affect the accuracy.

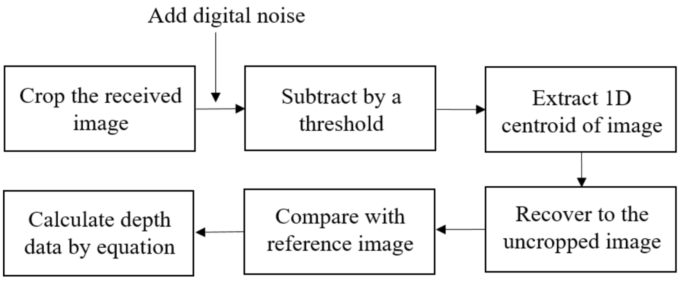

Fig. 5-9 The diagram illustrates the process from received image to obtaining depth data

The first step is to crop the original image into a small image with less pixels and make the center of image about 100 pixels away from the center of a received beam in order to reduce the processing time and improve the accuracy. A threshold should be set to reduce the influence of background light where we set the threshold T to the most optimized value [5]:

$$T = \overline{N_B} + 3\sigma_B \tag{5-3}$$

where $\overline{N_B}$ is the average ADUs of background light in received image, σ_B is standard deviation of background light.

After this procedure, the image will be subtracted by the threshold T and then processed by conventional centroid extracting algorithm or Steger center extracting algorithm [6,7]. Here for high-speed processing, assuming that $U = \sum_{i=1}^{L} x_i N_i,\ V =$

$\sum_{i=1}^{L} x_i N_i$, conventional centroid algorithm is adopted and the 1D centroid x'_c in the cropped image could be obtained by:

$$x'_c = \frac{U}{V} \qquad 5\text{-}4$$

Where x_i is the *x* coordinate of ith pixel, N_i is the ADUs in this pixel. In this procedure, the result of centroid is likely to be affected by various kinds of noises, such as readout noise, offset of a camera, shot noise of background light, background light level, shot noise of received beam and speckle noise.

In the next step, the x'_c in a cropped image will be transferred to the centroid x_c in the original image. Finally, the difference Δx between centroid in measured image x_c and the centroid in reference image x_{c0} could be combined with Eq. (2) and obtain the depth data. Therefore, we could find that the accuracy due to various noises σ_d is reflected on the error of centroid extracting σ_{x_c} or $\sigma_{x'_c}$ and the parameters in Eq. (2) as:

$$\sigma_d = \frac{(D + \delta d)^2 s \sigma_{x_c}}{fb} \qquad 5\text{-}5$$

where s is the pixel size of a camera. It could be found that the accuracy is related to the measured distance $D + \delta d$ and the centroid extraction of the received beam, which is related to the noise source including the camera self-noise, shot noise and speckle noise. Even if the noise source is not strong and σ_{x_c} is very small, depending on the measured depth increasing the accuracy will be poorer and poorer rapidly, which is why the structured-light sensing is difficult to be used in long-range measurement.

5.1.3 Real-time structured-light sensing based on VCSEL beam scanner

By using a VCSEL beam scanner integrated to a conventional VCSEL, the electrical beam steering could be realized. It provides the opportunity to realize the real-time structured-light depth sensing by using the schematic shown in Fig. 5-10. It was almost same to the Fig. 5-2, but the synchronization system was added, and a mirror is used to direct the propagation direction of the emitted light.

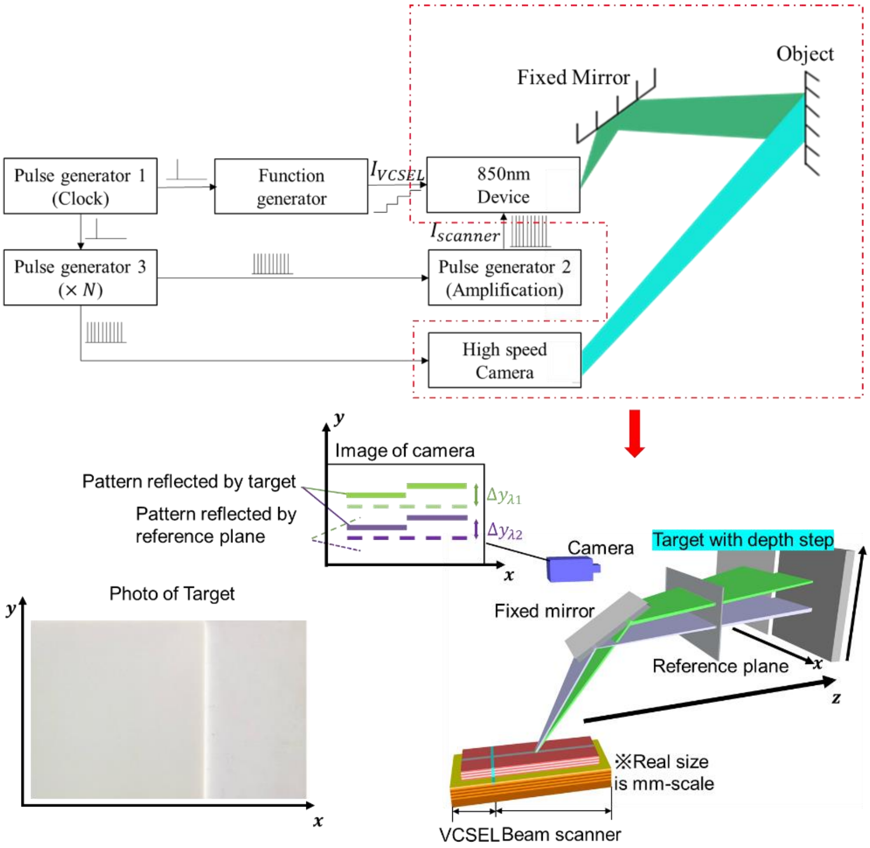

Fig. 5-10 Schematic of real-time beam scanning sensing

The synchronization was realized by pulse generators, function generators and camera. The first pulse generator was used as a clock pulse train to trigger the pulse controlling signal for scanner, camera and VCSEL, where the camera and the scanner will share the same controlling signals and work at the same time, but the pulse for scanner should be amplified to supply enough current to the scanner. The function generator is used to provide the signal to drive the VCSEL. In this system the VCSEL signal is a 20-step signal to make 20-step beam scanning. In details, the signal generated by the clock pulse generator 1 will be split to two path: First path is to function generator to provide the 20-step upstairs signal with period same to the clock period T_{clock}; Another path is to a pulse generator 3 to trigger 20 pulses with period of $T_{clock}/20$. The duty ration could be depending on the application, where the 72% was used in this experiment. Then the pulse train from generator 3 will go to trigger the camera shuttering and amplifier (when the current is enough for scanner, it is not needed.). Finally, the pulse train from amplifier will go to beam scanner. That is to say that the beam scanning frequency f_{scan} =1/T_{clock}, the camera shuttering speed f_{camera}, the total number of beams per frame N_{ytotal} and the scanning step per frame N_y has following relation:

$$N_{ytotal} = f_{camera} = N_y f_{scan} \qquad 5\text{-}6,$$

Because of using the mirror, the disparity in x direction will become that in y direction, so the Δx in Eq. 5-1 should be replaced by Δy. By using the similar step-target to do the real-time measurement, the parameters used in Table 5-1 could be realized. By using the parameter and system, the real-time structured-light could be demonstrated in the Fig. 5-11. The Fig. 5-11 (a) shows the reflected pattern by a step target, it could be seen that the clear cleave between the target could be seen. The resolution in x direction N_x is 500 (determined by the resolution of camera), and N_y=20, so the total resolution could be 10,000 with the framerate of 10Hz and low output power of 1mW. The Measurement target depth was shown in Fig 5-11 (b) and (c). The accuracy of A, B, C, D were estimated to be stable at around 0.3mm, because the experiment was finished indoors and the shot noise and background noise could be neglected while the speckle noise may be the main noise source.

Table 5-1 Parameters used in the real-time structured-light sensing

Parameters	Value
The number of lines per frame N_y	20
Scan speed f_{scan}	10Hz
Injected current to beam scanner	40mA
Output of beam scanner	1mW
Voltage added to VCSEL	4.5~5.4V
Pulse width of pulse generator 2	3.6ms
Aperture of camera F	1.4

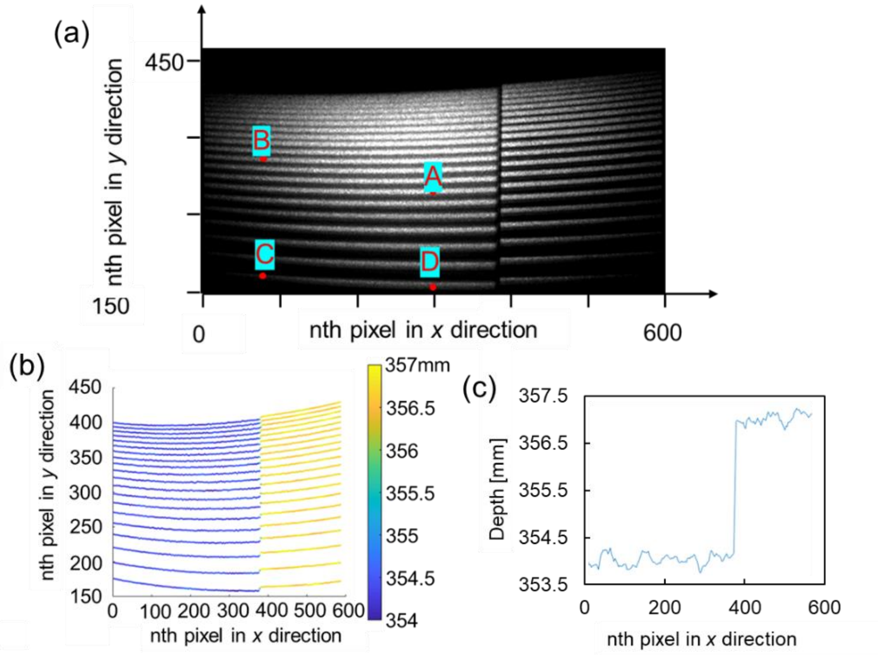

Fig. 5-11 The measurement result of real-time structured-light sensing

The real-time measurement could be witnessed by capturing the continuous-frame image as shown in Fig.5-12. In this figure, the 10 frames in 1 second was captured. It could be found that the good depth information stability could be obtained.

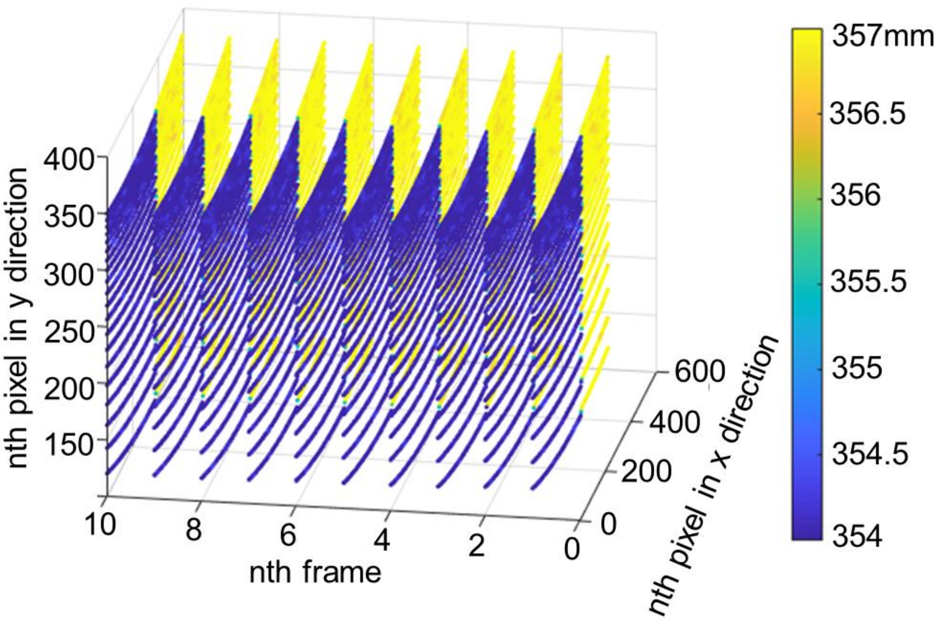

Fig. 5-12 The measurement result of real-time structured-light sensing

Actually, in this experiment the beam steering range is only 6°. Sometimes more than 30° may be needed for completed shape modelling. In this case, as shown in previous section, a DOE could be used to enhance the FoV of the beam scanner. The free-space measurement of a target are shown in Fig. 5-13, where (a) shows the beam beam scanning module schamtic and (b)(c)(d) shows the object photo, static FFP and scanned overlapped FFP. In this measurement a 10-spot DOE was introduced, the FoV could be enhanced to 40°, which is enough for most of applications. Besides, the resolution N_y could be also increased to 100 beams. In the real-time structured-light sensing measurement, only N_y and framerate of 10fps was used due to the limited camera speed. Without DOE, N_y=100 and framerate of 10fps need high-speed camera with speed of 1000fps. By using DOE, because 10 beams could be illuminated at the same time, the camera with speed of 100fps is enough, which is very easy even for mobile cameras. Considering the N_x =500, the total resolution number could be 50,000 by using the camera. The N_x is related to the maximum pixel number of camera, so it could be increased by using a camera with better resolution. Actually, for most of structured-light sensing light projector using the random dot projector, the resolution could not reach the pixel limitation, because the requirement of pattern coding [8]. Binary coded [9] or phase coded [10] line patterns could reach the pixel-limit resolution but the projector size is very large . The VCSEL beam scanner may be the first mm scale projector proving the pixel-limit resolution.

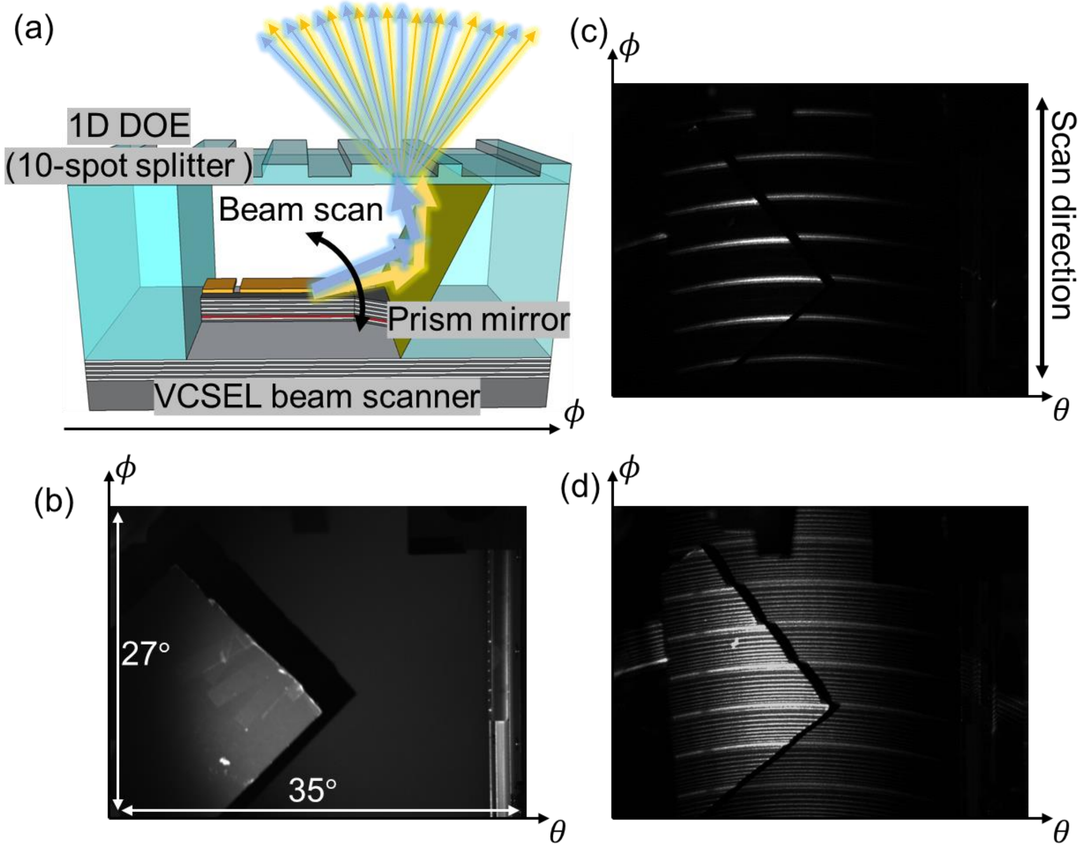

Fig. 5-13 FoV enhancement for structured-light sensing

To see the potential of this system for higher resolution, the exposure time of camera was reduced based on the Eq. 5-7 to simulate the power and noise condition when the resolution is higher,

$$t = 0.72/N_{ytotal} \tag{5-7}$$

because the higher-resolution will reduce the light energy received by the camera per data points. For example, if the total energy is 1J, if the resolution in 100, the energy per point is 0.01J, while if the resolution is 1000, the energy per point will become 0.001J. This principle is also suitable to simulate the framerate increasing. For example, for 10fps, the energy is 1J per frame, while for 100fps, the energy is 0.1J per frame when the power of projector is unchanged. The depth accuracy when increasing the N_{ytotal} and make N_x =500 is shown in Fig.5-14 (Dashed line: outdoor; Solid line: indoor).

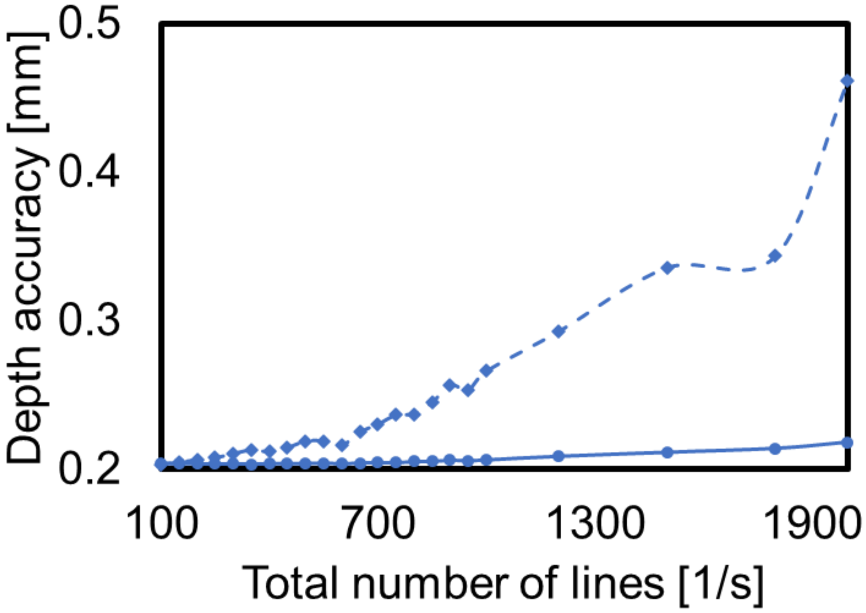

Fig. 5-14 Relation between N_{ytotal} and depth accuracy

It could be found that even if the N_{ytotal} is increased to 2,000, the sub-mm scale accuracy could be obtained even for outdoors measurement. This configuration could be suitable for N_y=100 and framerate is 20fps if a camera with 2000fps could be used. When a 10-spot DOE is introduced the N_y could be 1,000 and make the total resolution $N_y \times N_x$ =500,000. The power penalty due to DOE could be compensated by increasing power from 1mW to 10mW. The performance comparison between different kinds of current structured-light sensing is shown in Table 5-2.

Table 5-2 The performance comparison between different kinds of current structured-light sensing

Works	Framerate	Lateral resolution	Optical power
Microsoft Kinect V1	30fps	76,800	Not public
iPhone X	Not public	30,000	Not public
Intel Realsense SR300	30fps	300,000	150mW
This work	20fps	10,000	<1mW
Prospective by using a high-speed camera (2000fps) and DOE	20fps	500,000	<10mW

It could be found that the VCSEL beam scanner has potentially highest resolution and lowest optical power requirement than other structured-light sensing. Besides, the module size of VCSEL beam scanner could be managed within mm scale, which could be compatible with mobile devices.

5.2 Application of VCSEL beam scanner in LiDAR

This part is introducing the application of VCSEL beam scanner that was used in LiDAR system, which is completed mainly by other members in our Lab. The measurement system was shown in Fig. 5-15 [11]. The light generated by the beam scanner will be illuminated to the object and received by a indirect ToF camera. By estimating the flying time between the illumination time and received time of signal. The depth could be obtained. In our Lab, the system is based on indirect ToF camera, which uses the charges received at different shuttering angle to estimate the time of flight as shown in Fig. 5-16 [11].

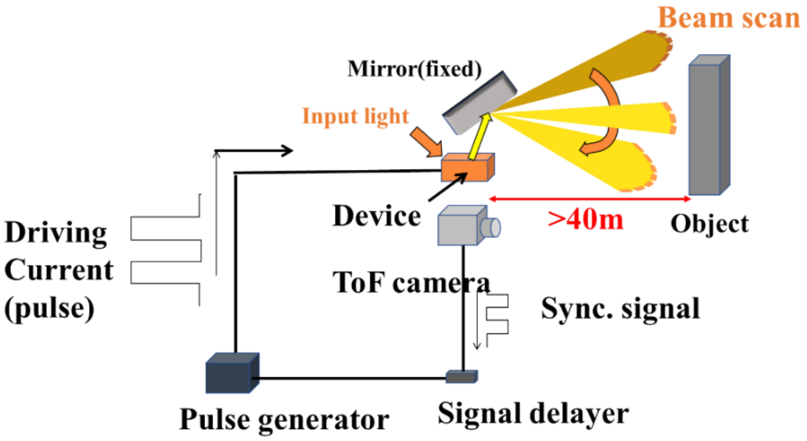

Fig. 5-15 System of LiDAR measurement based on VCSEL beam scanner

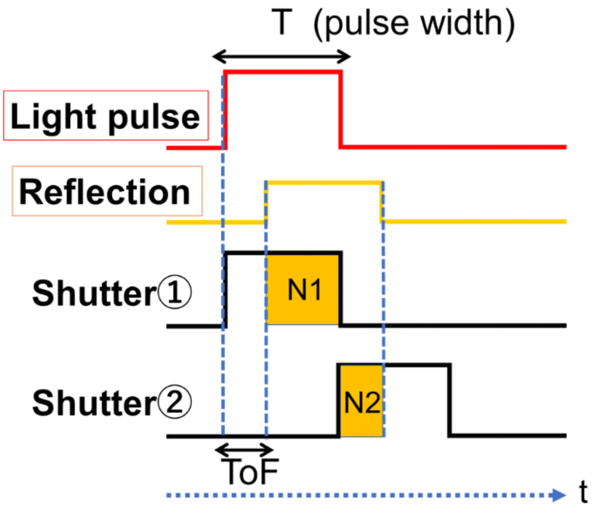

Fig. 5-16 The measurement principle of indirect LiDAR

Assuming the charges received in the shuttering window 1 and 2 are N_1 and N_2 respectively, the depth d should be estimated by Eq.5-8,

$$d = \frac{cT}{2}\frac{N_2}{N_1 + N_2} \tag{5-8}$$

where the c, T are light speed and shuttering window time.

By using the system the depth was measured when the output power is about 200mW indoors as following Fig. 4-7 [11].

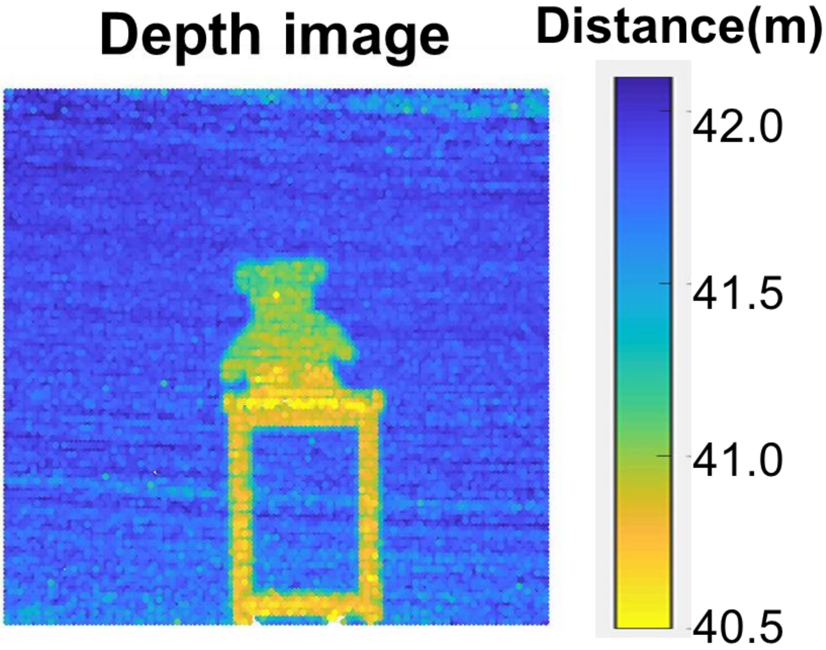

Fig. 5-16 The depth image by measuring using the VCSEL beam scanner-based LiDAR.

Although the experiment was completed in the indoors environment, the required power for the outdoors environment could be estimated as the following table 5-3.

Table 5-3 Required power estimation without DOE

Framerate	Divergence	Resolution	Number of shot	Period	Accuracy
20fps	0.1° × 0.1°	900×20	1	2.78us	10cm
Peak power @100m		20W	Average power consumption*		250mW
Peak power @20m		1W	Average power consumption*		12.5mW

Table 5-4 Required power estimation with a 10-spot DOE

Framerate	Divergence	Resolution	Number of shot	Period	Accuracy
20fps	0.1° × 0.1°	900×20	10	2.78us	10cm
Peak power @100m		50W	Average power consumption*		625mW
Peak power @20m		2W	Average power consumption*		25mW

where the duty ratio was assumed as 0.5% and the power efficiency was assumed to be 40% that suitable for convention VCSEL. It could be found that the required power for the module with a DOE will be larger than that without DOE, but the increase is not as large as spot number because for DOE condition, more shots could be integrated to measure the depth,

Reference in Chapter 5

5-1. J. Geng, "Structured-light 3D surface imaging: a tutorial," Adv. Opt. Photonics **3**(2), 128 (2011).

5-2. P. Zanuttigh, C. D. Mutto, L. Minto, G. Marin, F. Dominio, and G. M. Cortelazzo, *Time-of-Flight and Structured Light Depth Cameras: Technology and Applications* (2016).

5-3. B. Park, Y. Keh, D. Lee, Y. Kim, S. Kim, K. Sung, J. Lee, D. Jang, and Y. Yoon, "Outdoor Operation of Structured Light in Mobile Phone," Proc. - 2017 IEEE Int. Conf. Comput. Vis. Work. ICCVW 2017 **2018-Janua**, 2392–2398 (2018).

5-4. T. Jia, Z. Zhou, and H. Gao, "Depth measurement based on infrared coded structured light," J. Sensors **2014**, (2014).

5-5. L. Qi, Y. Zhang, X. Zhang, S. Wang, and F. Xie, "Statistical behavior analysis and precision optimization for the laser stripe center detector based on Steger’s algorithm," Opt. Express **21**(11), 13442 (2013).

5-6. Y. He and X. Li, "Error analysis of laser beam quality measured with CCD sensor and choice of the optimal threshold," Opt. Laser Technol. **45**(1), 671–677 (2013).

5-7. X. Ma, C. Rao, and H. Zheng, "Error analysis of CCD-based point source centroid computation under the background light," Opt. Express **17**(10), 8525 (2009).

5-8. S. Zhang, "High-speed 3D shape measurement with structured light methods: A review," Opt. Lasers Eng. **106**(March), 119–131 (2018).

5-9. O. Hall-Holt and S. Rusinkiewicz, "Stripe boundary codes for real-time structured-light range scanning of moving objects," Proc. IEEE Int. Conf. Comput. Vis. **2**, 359–366 (2001).

5-10. Y. An, J.-S. Hyun, and S. Zhang, "Pixel-wise absolute phase unwrapping using geometric constraints of structured light system," Opt. Express **24**(16), 18445−18459 (2016).

5-11. 修士論文: VCSEL ビーム掃引デバイスを用いた LiDAR システムに関する研究, 藤岡威吹, (2021).

Chapter 6

Conclusion and prospective

In this chapter, the thesis will be concluded, and the prospective will be discussed.

6.1 Prospective

6.1.1 Potential FoV and resolution of beam scanner

As discussed in the Chapter 1, the beam divergence could be narrower by extending the scanner length. For 1D beam scanning, the FoV is difficult to further improved but the resolution could be enhanced by using longer scanner. The Fig. 6-1 shows the estimation of resolution with varied scanner length from 0.1mm to 10mm for three kinds of DOE for different kinds of applications. It could be seen that more than 4,000 resolution points could be expected for 6mm-long devices. The resolution of 2D beam steering could be also increased by increasing the number of scanners integrated in the array. Considering the same system as illustrated in section 4.2.1, the resolution could be increased by increasing the number of scanners as shown in Fig. 6-2. It could be found that resolution of 28,800 is possible. For the 2D-DOE based 2D beam steering module mentioned in 4.2.2, the resolution could be also increased by increasing the number of spot of 2D DOE in ϕ direction. In ϕ direction of DOE, 15 spot with separation of 5° has been available. It could be used to increase the resolution to >60,000 and FoV to >70° × 70°. In θ direction, the increasing of separation angle θ_S may be helpful for increasing the FoV and resolution, however, larger θ_S may lead to the collimation degradation, it could be solved by using focal-length gradient cylindrical lens.

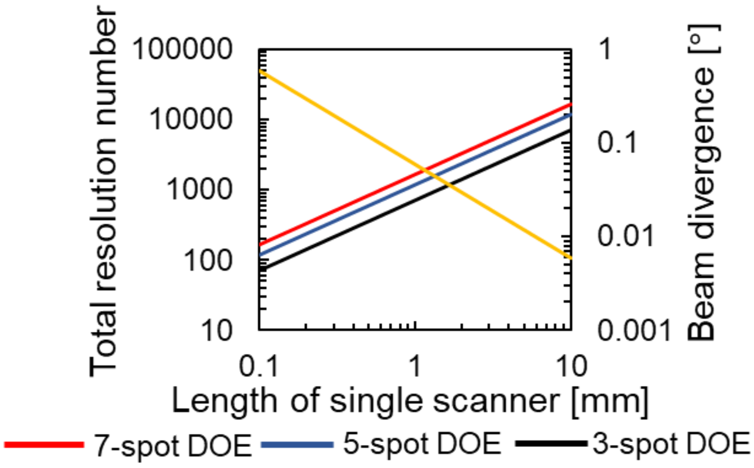

Fig. 6-1 The resolution of 1D beam steering with scanner length increasing

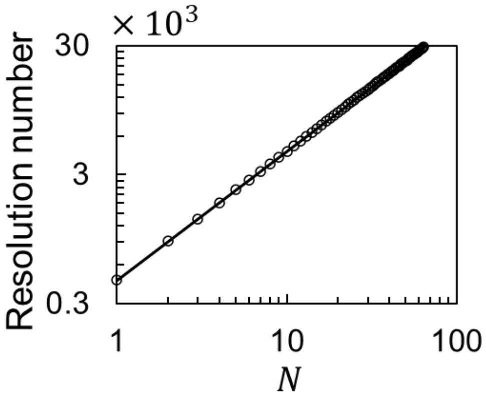

Fig. 6-1 The resolution of 2D beam steering with N increasing

6.1.2 Smaller module size by introducing prism instead of prism mirror

The prism mirror is largest element in the total beam steering module. The miniaturization of prism mirror will greatly be helpful for more compact beam steering module size. The flat optics could be used for replacing the prism mirrors, for example, the blaze grating, meta-surface beam deflector [1,2]. Besides, a prism may be a more convenient and cost-effective way to reduce the module size as shown in Fig. 6-3.

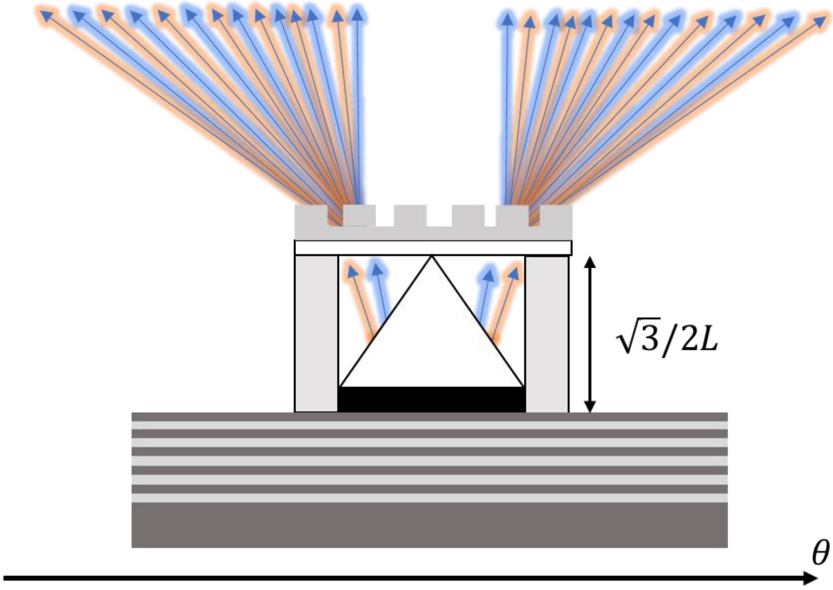

Fig. 6-3 The schematic of replacing prism mirrors by prism.

In this case, for a 2mm-long device, the module size could be reduced to <2mm. The cylindrical lens thickness may be another important factor to affect the module size. Meta lens [79,80] could reduce the thickness of cylindrical lens to <1mm.

6.1.3 FoV and resolution enhancement without DOE for higher power density

For long-range measurement, the power density penalty due to the introduction of DOE may be serious. A FoV enhancement method without DOE is important. For the solitary beam scanner, the FoV of 30° has been realized without DOE, but for beam scanner integrated to the VCSEL, limited by the tuning range of VCSEL, the maximum steering range without DOE is only < 10°. However, if the grating pitch size could be varied, the lasing wavelength is also varied and the deflection angle is also changed as shown in Fig. 6-4.

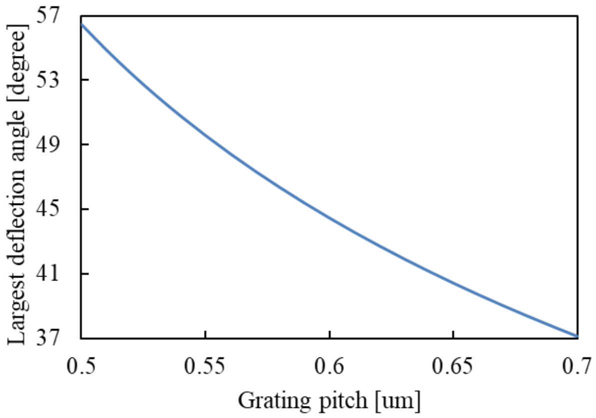

Fig. 6-4 Relation between deflection angle and grating

It provides the possibility by integrating varied-pitch-grating-loaded-VCSEL integrated beam scanners to cover larger FoV even without DOE as illustrated in Fig. 6-5. By using the pitch size of 550nm, the FoV of 49-57° could be covered and by using the pitch size of 600nm, the FoV of 41°-49° could be covered as shown in Fig. 6-6. By using a prism mirror, it could be deflected to 0°-16° and by using counter-propagation scanners, the FoV will be increased to -16°-16° even without DOE. Total 32° is sufficient for long-range LiDAR applications.

Fig. 6-5 Schematic of two-pitch slow-light VCSEL integrated scanners

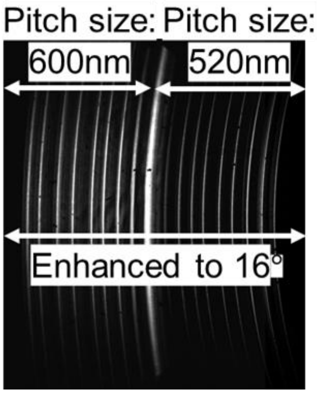

Fig. 6-6 FFP measurement by using two-pitch beam scanner.

Besides, the cylindrical lens could be used to realize 2D beam steering and counter-propagation-switchable device could be used to reduce the module size. Thus, we could design the flexiable beam scanning method for different applications as shown in Table 6-1.

Table 6-1. Different system design for different applications

Device type	DOE	FoV	relative intensity	Detection range
64 Two-pitch counter-propagation scanners	No DOE	32° × 32°	100	Long (100m)
64 counter-propagation scanners	1D 3×1	60° × 60°	33	Middle (50m)
6 Counter-propagation-switchable scanner	2D 10×10	100° × 70°	1	Short (10m)

For long-range detection, there are high requirements for power density, so the DOE is not equipped and the requirement for FoV could be a little relaxed. To realize enough FoV and resolution in ϕ direction, the 64 scanners will be integrated. It will also lead to larger chip size and higher expense, but for long-range detection it could be relaxed. For the middle range detection, the requirement of FoV will be a little increased, so a 3-spot 1D DOE is equipped. For the short-range detection, the requirement of FoV, size and cost becomes critical, so only 6 scanners need to be integrated and a 2D 10×10-spot DOE is introduced.

6.1.4 Higher potential power and narrow pulse width by injecting pulsed current to VCSEL

Currently, the power of integrated VSCEL is only <50mW scale and around 10% power could be coupled into the scanner. Considering the amplification of beam scanner as 30dB, the output power could be around 3W. However, for long-range application more than 10W is required. This is very critical issue for non-mechanical beam scanners including OPA and FPSA. To enlarge the output power of beam scanner, one method is to increasing the coupled power from VCSEL. The power of VCSEL currently was limited by the thermal effect. If pulsed current could be injected in to the VCSEL, the power could be more than 100mW, which may excite large output power from beam scanner of more than 10W. Also, narrow pulse width is also important for LiDAR applications. Current large-current/voltage pulse generator is difficult to generate ultra-shot pulse width of <1ns. However, for the VCSEL beam scanner, the output pulse width is determined by the pulse width of both current pulse width of VCSEL and beam scanner. The current injected to the VCSEL is much smaller than that for beam scanner, so narrow pulse width current/voltage driver is possible. By injecting ultra-narrow pulsed current to VCSEL, the optical pulse width of beam scanner could be also narrower. Because the pulsed current was injected into the VCSEL, the self-heating thermal effected wavelength tuning is not available anymore, an extra heat may be needed to drive the beam scanning.

6.1.5 Prism mirror functions to compensate the beam curvature

As illustrated in the previous section, the curved line make lead to some problem for the detectors. It is useful to compensate the line curvature by using a curved prism. The curved prism was designed as the following figure. Firstly, the curved line could be fitted by the parabolic curve. Based on the fitted line, the curvature of the prism could be designed. By using this design, the simulation setup was established in Zemax. It could be used to simulate the change of curvature after being reflected by the prism.

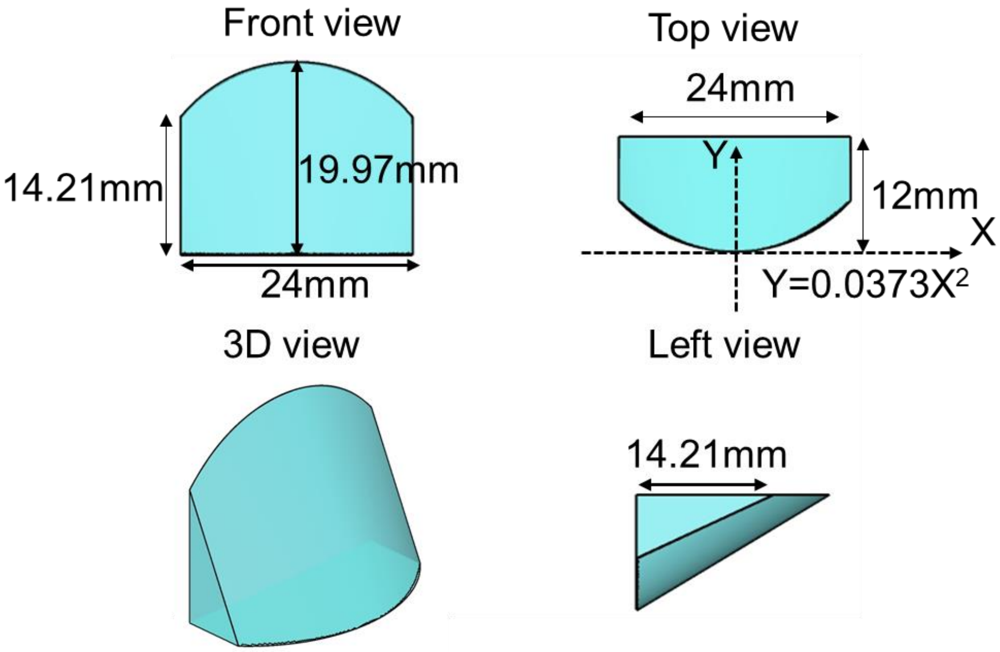

Fig. 6-7 The designed prism for compensation of beam curvature

The simulated result was shown in Fig. 6-8, it could be found that the curvature was compensated.

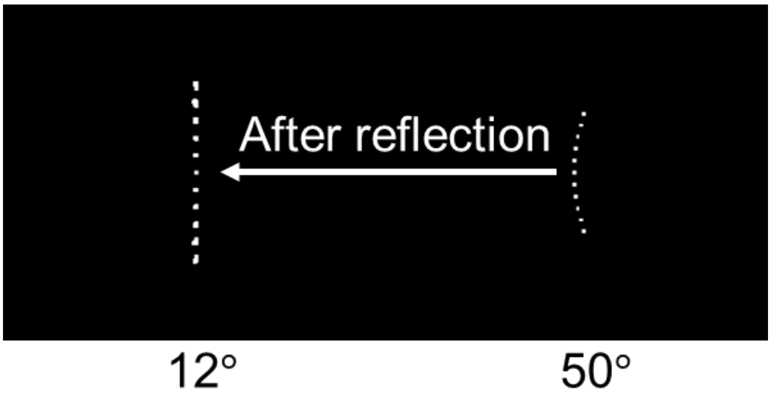

Fig. 6-8 The simulated beam in Zemax after being reflected by the prism

6.2 Conclusion

In this thesis, the principle and schematic of solitary beam scanner based on VCSEL waveguide/amplifier was firstly introduced. The device was also successfully fabricated based on the conventional VCSEL wafer. Its characteristic was also evaluated including the spectrum, NFP/FFP and power. It covers the FoV of 18° ×14° ($\Delta\phi \times \Delta\theta$) and power of more than 3W. The solitary beam scanner was also integrated to a conventional VCSEL through wavelength detuning structure and integrated to grating-loaded slow-light VCSEL. For conventional VCSEL-integrated beam scanner, it realized electrical beam steering of >12° with resolution of >100. For slow-light integrated beam scanner, the beam steering range is >7° and the power could be larger than 2W, which could be further improved to >10W by injecting pulsed current in both VCSEL and beam scanner side and extending the beam scanner length. The scanning frequency could reach >100kHz.

A DOE-based optics system and counter-propagation scanner integration was used to enhance the FoV and resolution of above-mentioned beam scanner. For 6mm-long solitary beam scanner, the record large FoV of >100° ×14° and resolution of >4,000 was obtained. For the VCSEL-integrated beam scanner, the electrically-driven 1D beam steering of >100° was also realized with resolution of >1,400, which is compatible for almost all the 3D sensing applications and has great potential for miniaturized package size. Besides, by extending the scanner length the potential resolution of >4000 is also possible. The size of total module for 2mm-long scanner currently is 6mm scale and could be reduced to 2mm by replacing the prism mirror by flat deflector or prism.

Considering the larger beam intensity and power density, 2D beam steering module was proposed and demonstrated based on the VCSEL beam scanner array and DOE-based optics. The 2D beam steering with FoV of >64° ×14° and resolution of >9,000 was realized by fabricating a 20-scanner virtual array and 10-spot DOE. By integrating more scanners in the array, the FoV in ϕ direction could be extended to >40° and resolution could be increased to >28,800. To further increase the FoV of 2D beam steering in ϕ direction and miniaturize the scanner chip size, the counter-propagation-switchable scanners was fabricated and applied to realize 2D beam steering with FoV of >70° ×42° by using a 10×7-spot 2D DOE. It also reached the high resolution of >30,000. There are still potential to increase the FoV and resolution to >70° ×70° and >60,000 by using an available 10×15-spot DOE. The resolution and FoV in θ direction could also be increased by using a DOE with larger separation angle if a focal-length-gradient lens could be applied.

The beam scanner was also applied in the 3D sensing including structured-light sensing and ToF LiDAR primarily. For structured-light sensing, the depth image of target at 30cm to 5mm were obtained with relative depth accuracy of <0.1%. The real-time structured-light sensing was also demonstrated and realized sub-mm-accuracy depth imaging with resolution of >10,000 and framerate of 20fps. For ToF LiDAR, the depth image was obtained at 40m with relative accuracy of <1%. The scanner is also available for FMCW LiDARs.

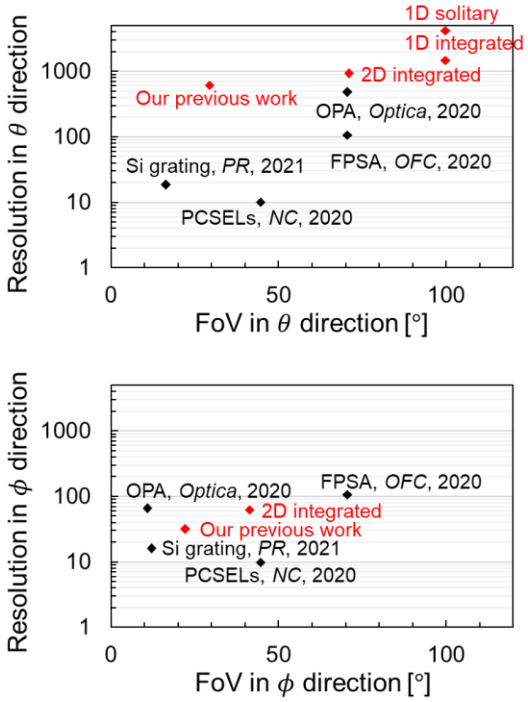

Fig. 6-9 The position of this work compared to other works

Reference in Chapter 6

6-1. T. Aoyagi, Y. Aoyagi, and S. Namba, "High-efficiency blazed grating couplers," Appl. Phys. Lett. **29**(5), 303–304 (1976).

6-2. D. Wang, Q. Fan, J. Wang, Z. Zhang, Y. Liang, and T. Xu, "All-dielectric metasurface beam deflector at the visible frequencies," Guangdian Gongcheng/Opto-Electronic Eng. **44**(1), 103–107 (2017).

6-3. Z. Bin Fan, Z. K. Shao, M. Y. Xie, X. N. Pang, W. S. Ruan, F. L. Zhao, Y. J. Chen, S. Y. Yu, and J. W. Dong, "Silicon nitride metalenses for unpolarized high-NA visible imaging," 2018 Conf. Lasers Electro-Optics, CLEO 2018 - Proc. 2–3 (2018).

6-4. Y. Y. Xie, P. N. Ni, Q. H. Wang, Q. Kan, G. Briere, P. P. Chen, Z. Z. Zhao, A. Delga, H. R. Ren, H. Da Chen, C. Xu, and P. Genevet, "Metasurface-integrated vertical cavity surface-emitting lasers for programmable directional lasing emissions," Nat. Nanotechnol. **15**(2), 125–130 (2020).

6-5. J. Engelberg and U. Levy, "The advantages of metalenses over diffractive lenses," Nat. Commun. **11**(1), 9–12 (2020).

6-6. A. She, S. Zhang, S. Shian, D. R. Clarke, and F. Capasso, "Adaptive metalenses with simultaneous electrical control of focal length, astigmatism, and shift," Sci. Adv. **4**(2), 1–8 (2018).

6-7. M. Khorasaninejad, W. T. Chen, R. C. Devlin, J. Oh, A. Y. Zhu, and F. Capasso, "Metalenses at visible wavelengths: Diffraction-limited focusing and subwavelength resolution imaging," Science (80-.). **352**(6290), 1190–1194 (2016).

Publication list

(a) Journal Papers (as first author)

[J-1] Ruixiao Li, Shanting Hu, Xiaodong Gu, and Fumio Koyama, "*Compact solid-state vertical-cavity-surface-emitting-laser beam scanning module with ultra-large field of view*," Appl. Phys. Express, published, 2021, DOI: 10.35848/1882-0786/ac2ff8

[J-2] Ruixiao Li, Shanting Hu, Xiaodong Gu, and Fumio Koyama, "*Solid-state Slow-light Beam Scanner with Ultra-large Field of View and High Resolution*," IEEE/OSA J. Lightwave Technology, published, 2021, DOI: 10.1109/JLT.2021.3129489

[J-3] Ruixiao Li, Shanting Hu, Xiaodong Gu, and Fumio Koyama, "*Demonstration of real-time structured-light depth sensing based on a solid-state VCSEL beam scanner*," Opt. Express, published, 2021, DOI: 10.1364/OE.448506

[J-4] Ruixiao Li, Shanting Hu, Xiaodong Gu, and Fumio Koyama, "*High-resolution two-dimensional solid-state beam scanner module based on vertical-cavity-surface-emitting laser array*," Appl. Phys. Express, published, 2022, DOI: 10.35848/1882-0786/ac4dda

[J-5] Ruixiao Li, Xiaodong Gu, and Fumio Koyama, "*Structured-light depth sensing based on solid-state VCSEL beam scanner*," Appl. Optics, Submitted, 2021

(b) International Conferences (as presenter)

[I-1] Ruixiao Li, Zeuku Ho, Xiaodong Gu, and Fumio Koyama, "*Structured-Light Sensor Based on Non-mechanical VCSEL beam scanner,*" Micro Optics Conference 2018, E-3, 2018

[I-2] Ruixiao Li, Zeuku Ho, Xiaodong Gu, and Fumio Koyama, "*Wide-range structured-light sensing based on non-mechanical VCSEL beam scanner,*" Micro Optics Conference 2019, E-2, 2019

[I-3] Ruixiao Li, Zeuku Ho, Xiaodong Gu, and Fumio Koyama, "*Structured-Light Sensor Based on Non-mechanical VCSEL Beam Scanner,*" International Nano-optoelectronics Workshop (iNOW) 2019, 2019

[I-4] Ruixiao Li, Zeuku Ho, Xiaodong Gu, and Fumio Koyama, "*Real time Structured-light Depth Sensing Based on Ultra-compact, Non-mechanical VCSEL Beam Scanner,*" Optical Fiber Communication Conference and Exhibition (OFC) 2020, M1C.6, 2020

[I-5] Ruixiao Li, Zeuku Ho, Xiaodong Gu, and Fumio Koyama, "*Enhanced-Field-of-View Solid-State VCSEL Beam Scanner with Lateral Resolution Points of More than 1200,*" The 46th European Conference on Optical Communication (ECOC) , Th1L-5, 2020

[I-6] Ruixiao Li, Zeuku Ho, Xiaodong Gu, and Fumio Koyama, "*Solid-state VCSEL beam scanner with ultra-large field of view and high resolution,*" Optical Fiber Communication Conference and Exhibition (OFC) 2021,W1D.3, 2021 (Top ranked)

[I-7] Ruixiao Li, Xiaodong Gu, Satoshi Shinada, and Fumio Koyama, "*Compact 1D/2D VCSEL Beam Scanner with Enhanced Field of View and High Resolution,*" The 47th European Conference on Optical Communication (ECOC), Th1D.3, 2021

[I-8] Ruixiao Li, Xiaodong Gu, Satoshi Shinada, and Fumio Koyama, "*Ultra-compact VCSEL beam scanner with large field of view and its 2D beam scanning function,*" 27th international semiconductor laser conference (ISLC), 2021

[I-9] Ruixiao Li, Shanting Hu, Xiaodong Gu, Satoshi Shinada, and Fumio Koyama, "*Electrically-driven 2D multi-beam steering with large field of view by using VCSEL scanner array",* Conference on Lasers and Electro-Optics (CLEO) 2022, Submitted, 2022

(c) Domestic Conferences

[D-1] Ruixiao Li, Zeuku Ho, Xiaodong Gu, and Fumio Koyama, "*Structured-Light Sensor Based on Non-mechanical VCSEL Beam Scanner,*" The 79th JSAP Autumn Meeting, 19a-438-9, 2018.

[D-2] Ruixiao Li, Zeuku Ho, Xiaodong Gu, and Fumio Koyama, "*Accuracy Analysis of Structured-Light Sensor Based on Non-mechanical VCSEL Beam Scanner*," The 66th JSAP Spring Meeting, 2019, 9p-W331-2, 2019.

[D-3] Ruixiao Li, Zeuku Ho, Xiaodong Gu, and Fumio Koyama, "*Structured-light sensing based on non-mechanical VCSEL beam scanner for expanding the distance range*," The 80th JSAP Autumn Meeting, 2019, 20a-E207-11, 2019.

[D-4] Ruixiao Li, Zeuku Ho, Xiaodong Gu, and Fumio Koyama, "*Solid-State Beam Scanner with Large Field of View and Resolution Points of More than 1200,*" The 68th JSAP Spring Meeting 2021, 18a-Z18-2, Sep. 2021.

[D-5] Ruixiao Li, Xiaodong Gu, Fumio Koyama "*Compact VCSEL beam scanner with* *large field of view and its 2D scanning function*," The 82nd JSAP Autumn Meeting, 10a-N405-6, Sept. 2021.

[D-6] Ruixiao Li, Xiaodong Gu, Fumio Koyama "*Electrically-driven solid-state 2D VCSEL beam scanner with large field of view and high-resolution*," The 69th JSAP Spring Meeting, Sept. 2021 (Invited talk).

List of Awards

51th Young scientist award in JSAP 82nd autumn meeting (第51回応用物理学会講演奨励賞)

謝辞 Acknowledgement

Firstly, I hope to express my great gratitude to Prof. Fumio Koyama thanks to his opportunity for me to have greatly valuable study experience in Japan and his kind supervision during my 4.5-year study period.

I also hope to thank to other professors in our lab :Prof. Iga Kenichi, Prof. Hiroyuki Uenohara and Prof. Tomoyuki Miyamoto, because their advice in various meetings and conferences. Besides, I hope to thank to Prof. Nobuhiko Nishiyama and Prof. Kentaro Nakamura in Tokyo Institute of technology and Prof. Toshihiko Baba in National Yokohama University for their advice to my study and review of my thesis.

I also hope to thank Prof. Susumu Kinoshita, Dr. Takahiro Sakaguchi and Mr. Hisao Sudo for their kind help for my experiment and management of clean room.

I wish to thank Prof. Xiaodong Gu for his useful academic advise and help in daily life.

I hope to thank sectary of Koyama Lab: Ms. Hiromi Yoshida, Ms. Satsuki Ogawa, Ms. Tomie Chiba, Ms. Etsuko Koiwa for their help of my life in the Lab.

I hope to thank Dr. Shanting Hu, Dr. Hameeda Ibrahim, Dr. Ahmeda Hassan, Dr. Zeuku Ho for their help to my experiment and advice of my study.

I also hope to thank Mr. Liang Dong, Mr. Boxuan zhang, Ms. Chang Ge for their academic communication and life support.

I also wish to give m thanks to Mr. Weicheng Fang, Mr. Yiqi Zhang for their academic communication and urgent life support especially when I just came to Japan.

I also would like to thank all of our Lab members for my life and study support.

I also thank to the funding from Japan Science and Technology Agency.

Finally, I must thank to my parents for their support in every aspects.